

1995

Increasing the efficiency of a piezoelectric aluminum nitride microstrip resonator by utilizing high temperature superconductors

Edward David Goff
Iowa State University

Follow this and additional works at: <https://lib.dr.iastate.edu/rtd>

 Part of the [Electrical and Electronics Commons](#), [Electromagnetics and Photonics Commons](#), and the [Physics Commons](#)

Recommended Citation

Goff, Edward David, "Increasing the efficiency of a piezoelectric aluminum nitride microstrip resonator by utilizing high temperature superconductors " (1995). *Retrospective Theses and Dissertations*. 10780.
<https://lib.dr.iastate.edu/rtd/10780>

This Dissertation is brought to you for free and open access by the Iowa State University Capstones, Theses and Dissertations at Iowa State University Digital Repository. It has been accepted for inclusion in Retrospective Theses and Dissertations by an authorized administrator of Iowa State University Digital Repository. For more information, please contact digirep@iastate.edu.

INFORMATION TO USERS

This manuscript has been reproduced from the microfilm master. UMI films the text directly from the original or copy submitted. Thus, some thesis and dissertation copies are in typewriter face, while others may be from any type of computer printer.

The quality of this reproduction is dependent upon the quality of the copy submitted. Broken or indistinct print, colored or poor quality illustrations and photographs, print bleedthrough, substandard margins, and improper alignment can adversely affect reproduction.

In the unlikely event that the author did not send UMI a complete manuscript and there are missing pages, these will be noted. Also, if unauthorized copyright material had to be removed, a note will indicate the deletion.

Oversize materials (e.g., maps, drawings, charts) are reproduced by sectioning the original, beginning at the upper left-hand corner and continuing from left to right in equal sections with small overlaps. Each original is also photographed in one exposure and is included in reduced form at the back of the book.

Photographs included in the original manuscript have been reproduced xerographically in this copy. Higher quality 6" x 9" black and white photographic prints are available for any photographs or illustrations appearing in this copy for an additional charge. Contact UMI directly to order.

UMI

A Bell & Howell Information Company
300 North Zeeb Road, Ann Arbor, MI 48106-1346 USA
313/761-4700 800/521-0600

**Increasing the efficiency of a piezoelectric aluminum nitride microstrip resonator by utilizing
high temperature superconductors**

by

Edward David Goff

**A Dissertation Submitted to the
Graduate Faculty in Partial Fulfillment of the
Requirements for the Degree of
DOCTOR OF PHILOSOPHY**

**Department: Electrical and Computer Engineering
Major: Electrical Engineering (Microelectronics)**

Approved:

Signature was redacted for privacy.

In Charge of Major Work

Signature was redacted for privacy.

For the Major Department

Signature was redacted for privacy.

For the Graduate College

Members of the Committee:

Signature was redacted for privacy.

**Iowa State University
Ames, Iowa**

1995

UMI Number: 9540894

UMI Microform 9540894

Copyright 1995, by UMI Company. All rights reserved.

**This microform edition is protected against unauthorized
copying under Title 17, United States Code.**

UMI

**300 North Zeeb Road
Ann Arbor, MI 48103**

TABLE OF CONTENTS

ABSTRACT	iii
I. STATEMENT OF PROBLEM.....	1
II. LITERATURE OVERVIEW	3
II.A. Materials	3
II.B. Applications	14
III. THEORY	18
III.A. Experimental Models	18
III.B. Microwave Superconductor Theory.....	20
III.C. Mason Model Theory	22
III.D. Transmission Line Analysis.....	24
III.D.1. Equivalent Inductance	27
III.D.2. Resistance at the Interface.....	34
III.D.3. Mason Model Analysis	36
III.D.4. Theoretical Results	41
IV. EXPERIMENTAL METHOD	49
IV.A. Experimental Design.....	49
IV.B. Substrate Selection	57
IV.C. Buffer Layer Selection.....	59
IV.D. Laser Ablation	60
V. RESULTS	62
VI. CONCLUSIONS	76
VI.A. Significant Contributions.....	77
VI.B. Future Work.....	78
BIBLIOGRAPHY	80
ACKNOWLEDGMENTS	89
APPENDIX A: PUBLICATIONS.....	90
APPENDIX B: SOL-GEL PROCESSING	103
APPENDIX C: GRAVIMETRIC ANALYSIS	109
APPENDIX D: ALUMINUM NITRIDE PROCESSING.....	111
APPENDIX E: PROGRAMS	113

ABSTRACT

High temperature superconductors have potential applications in the field of microwave devices and circuits. To utilize these materials in such a way as to increase the efficiency of these microwave devices would be beneficial for high efficiency / low noise applications. This dissertation accomplishes the following goals: 1) The design and fabrication of an initial device that increases the quality factor, Q , and therefore the efficiency of a high frequency thin film resonator which uses superconducting metal as the device's electrode, 2) the measurement and characterization of this device, 3) the theoretical calculation and predicted performance of this device, and 4) the comparison of the measured response of this device with the measured response of a similar device made by the standard method using metals in place of the superconductor. Using a modified transmission line analysis approach, a theoretical microwave model of a superconducting metal electrode has been developed. The high temperature superconductor characteristics were modeled electrically by the two-fluid model using the modified transmission line model, and acoustically by using an extension of the Mason model for piezoelectric bulk acoustic wave resonators.

Experimental test setups were designed to measure the direct current and microwave characteristics of the high temperature superconductors and devices. A high temperature superconducting microwave resonator structure was fabricated and compared with a similar non-superconducting resonator structure. All results were compared with the aforementioned theoretical results, and conclusions were drawn on the feasibility of the overall project.

Aluminum electroded bulk acoustic wave resonators performed well at liquid nitrogen temperature as well as at room temperature. The high temperature superconductor bottom electroded bulk acoustic wave resonators with aluminum as the top electrode showed

signs of acoustic activity of the aluminum nitride, but the results were not directly comparable to the aluminum electroded structures. More research will need to be performed on the acoustic properties of these high temperature superconductors to further understand and utilize these materials as electrodes on a thin film resonator.

I STATEMENT OF PROBLEM

High temperature superconductors have potential applications in the field of microwave devices and circuits. To utilize these materials in such a way as to increase the efficiency of these microwave devices would be beneficial for high efficiency / low noise applications. This dissertation accomplishes the following goals: To create a device that will increase the quality factor, Q , and the efficiency of a high frequency resonator, to measure and characterize this device, to theoretically calculate and predict the performance of this device, and to compare this device to a similar device made by the standard method using metals in place of the superconductor.

The problem is that this combination of materials has not been attempted previously. The high temperature superconductor - Aluminum Nitride (hereafter abbreviated HTSC - AlN) interface is not mentioned in literature, and there is no mention of stacked acoustic wave resonators utilizing superconductors. There are several processing steps that may affect the material properties of the High Temperature Superconductor or the piezoelectric Aluminum Nitride which has been modeled and experimentally evaluated.

In this dissertation, sol-gel and laser ablated HTSCs will be fabricated and analyzed. The sol-gel was the initial attempt at the growth of the HTSC, and the results are promising, but not consistent enough for the fabrication of devices. The method of this sol-gel process will be discussed in the literature section. The HTSC devices for this dissertation were fabricated using laser ablation. The laser ablated films are superior in grain size and uniformity across the sample.

The theoretical modeling was performed using a transmission-line analysis along with utilizing the Mason model for modeling the piezoelectric effect. Using a Fortran code given in Appendix D, the potential and current for the superconducting resonator were found

theoretically. The piezoelectric effects were modeled using the Mason model, and these results are compared with the experimental results.

The experimental analysis of this dissertation was performed in three parts. The HTSC was tested for resistivity, along with several samples tested for magnetic susceptibility. The resonator is tested using a HP8753 network analyzer with S-parameters at both room temperature and liquid nitrogen temperature for all three structures under investigation: Al-AIN-Al, HTSC-AIN-Al, HTSC-AIN-HTSC. The radio frequency measurement portion of this dissertation was compared to the theoretical results and conclusions are drawn from the results.

The conclusions drawn from this dissertation are that the material properties of the HTSC are not conducive to the production of bulk acoustic wave Aluminum Nitride resonator structures. A different technique in the manufacturing of resonators such as stripline resonators must be pursued for use with HTSCs.

II. LITERATURE OVERVIEW

II.A. Materials

There are many different materials that exhibit the properties of a superconductor. With the arrival of high temperature superconductors in 1986 [1], the definition of superconductors changed dramatically because of this new class of superconducting ceramics. The distinction was made between high temperature superconductors, hereafter abbreviated HTSC, such as $Y_1Ba_2Cu_3O_{7-x}$, and low temperature superconductors such as Niobium and Lead in 1989 with the discovery of HTSC.

Low temperature superconductors, hereafter abbreviated LTSC, have been the superconducting materials of choice for years and continue to have use in large electromagnets such as in the now defunct superconducting supercollider project and other projects where a high magnetic field is desired. The HTSCs have shown themselves to be brittle and somewhat difficult to work with while the LTSCs have well-documented properties and are easily tailored to different applications. The major drawback of LTSCs is that these materials must use liquid helium as a refrigerant. This is much more expensive and difficult to handle than the liquid nitrogen required for HTSCs.

HTSCs are based on ceramic perovskite materials. Certain processing differences are inherent between LTSCs and HTSCs, since ceramic processing is much more versatile than the low temperature metal superconductors. There are five main classes of high temperature ceramic superconductor processing: chemical vapor deposition, laser ablation, co-evaporation, solid-state processing, and sol-gel processing. Each will be discussed in brief detail.

Chemical Vapor Deposition (hereafter abbreviated CVD) is a technique used by many researchers for many different applications. The basic theory behind CVD is that organometallic compounds are introduced to a substrate through a carrier gas. This gas may or may not participate in the reaction, but there must be a method of transport for the organometallics. The organometallics contain the desired elemental constituents in proper ratios along with long carboxylate or hydrocarbon chains. To produce films, a reaction between these chemicals must take place to release the elements from the organometallic compound. The most general type of reaction uses heat as a catalyst. A heated substrate is used to produce film growth from the surface decomposition of the organometallic compound. Another type of CVD reaction takes place in a plasma adjacent to the substrate. This method is referred to as Plasma Enhanced Chemical Vapor Deposition, or PECVD. A reaction of this type is accomplished by using a chemical plasma of carrier gas, either inert or a reactant gas in the chemical reaction, and the interaction of the organometallic gas. The plasma causes the material to break down and the elements then combine to form the desired product. This technique is somewhat beneficial because the carrier gas may react with the organics and create a thermodynamically stable product that will leave the plasma and will not be deposited, leaving only the desired constituents deposited onto the substrate.

There may be more than one organometallic compound in the CVD reaction, and this is the case with high temperature superconductors. There must be three different compounds to account for the three elements in the $Y_1Ba_2Cu_3O_{7-x}$ superconductor. The oxygen is not included in this reaction, since a post processing sintering process will add the oxygen to the HTSC. The breaking down of the organometallic compound is directly linked to the carrier gas. Since the superconductor does not have carbon in its structure, and the organometallic does have an abundance of carbon in its structure, the carbon must be removed by a high temperature firing process which will drive out the carbon and other impurities. Examples of source materials for the CVD of high temperature superconductors are $Y(thd)_3$, $Ba(thd)_2$, and

$\text{Cu}(\text{thd})_2$ where thd stands for 2,2,6,6-tetramethyl-3,5-heptanedionate [2]. The benefits of using CVD are: uniformity of films produced, controllable growth parameters, and speed of growth.

The next method of deposition for superconductors is that of laser ablation. The concept behind laser ablation can be related to small area evaporation. A high power laser, usually a CO_2 or eximer type laser, is used to strike a target of $\text{Y}_1\text{Ba}_2\text{Cu}_3\text{O}_{7-x}$ that has already been prepared in the correct stoichiometry and is itself a superconductor. When the laser strikes the superconductor target, $\text{Y}_1\text{Ba}_2\text{Cu}_3\text{O}_{7-x}$ material is ablated off the surface of the target, and then proceeds toward the substrate which is placed in such a location to receive an optimum amount of material. The ablation process is similar to evaporation on a smaller scale. Typically, the substrate is heated to promote crystalline growth. This entire sequence of events takes place in a high-vacuum environment. In-situ heat treatments, as well as subsequent annealing will produce the desired superconducting film. This method is one of the methods that the author is utilizing in this dissertation and will be discussed in further detail in the methods section.

The next method of deposition for HTSC thin films is that of co-evaporation. Co-evaporation is accomplished in a high-vacuum environment. The three constituent elements of the superconductor are present in either metallic form or a similar form capable of evaporation. Three crucibles are enclosed in the vacuum chamber, and then are heated up to very high temperature. The material inside the crucibles evaporates toward a heated substrate. The three constituent elements arrive via stoichiometrically proportional fluxes to produce the correct atomic ratio for the superconductor on the substrate. The flux rate of the constituent elements is controlled by adjusting the temperature of the corresponding crucibles. This method is also referred to as Molecular Beam Epitaxy, or MBE.

Solid-State processing refers to the technique of mixing the oxides of the constituent elements together in proper proportions and grinding them up to produce a homogeneous powder. This powder is then sintered and the process is repeated. After the powder is determined to be the correct phase of superconductor via X-Ray diffraction, Meissner effect measurement, and/or resistivity measurements, it is then pressed into pellets or whatever shape is desired. A binding agent may be added to promote adhesion in the sample. Although this is not technically a thin film, it is mentioned because some of the data taken for microwave measurements comes from these types of samples.

The final process for the creation of thin films is that of the Sol-Gel procedure. This is the second method in this project that has been used to create HTSC films. Sol-Gel refers to the creation of a solution of chemicals suspended in various solvents such as water or alcohols, which upon concentration yields a gelatinous substance with the identical stoichiometry as the starting mixture of chemicals. This is the basis for sol-gel processing. The benefits of sol-gel are that the chemical components may be controlled with a high degree of accuracy depending only on the quality of the starting components. Ratios of chemicals may be modified and altered by simply adding more of one component, or subtracting some of another component. The high level of uniform stoichiometry inherent in this process is due to the mixing of the solution. The experimental procedure used in the sol-gel processing performed on this project will be discussed in detail in Appendix B.

There are many different methods to create the superconducting sol-gel films. The different methods all will yield superconducting thin films of differing qualities. The difference in the quality of the films comes from the difference in the chemistry of the precursors. Some precursors affect the firing process of the sol-gel solutions adversely, thus altering the superconductor quality by means of defects or contaminants. The superconducting sol-gel systems all require a high-temperature firing step to form the superconducting phase of YBCO. This is common to all of these systems, although

depending on the processing and the chemical constituents, the time and temperature of the firing may change dramatically.

Different chemical systems yield drastically different results. Some of the different chemical systems that have been quoted in the literature include the following classes of systems. One class of superconducting sol-gels is the Nitrate system. Nitrates of Y, Ba, and Cu are mixed in polymeric acids such as Polyacrylic Acid, Oxalic Acid, Citric Acid and Ethylene Glycol [36,37,38]. The benefits of using such long molecular chains of acids along with the constituent YBa_2Cu_3 is that these long chains promote the gelation process to occur when the solution is concentrated. Citrates of the three constituent precursors (Y, Ba, Cu) will gelate by themselves, and with the addition of Oxalic Acid to the solution, gelation will occur with improved uniformity and controllability [39].

Another method of employing long-chain polymers in the system is to attach the chemical constituents to an alkoxide compound. Examples of this method are complex molecules such as Y-methoxyethoxide, Ba-methoxyethoxide, Cu-ethoxide [40,41], and Y- $(\text{CH}_3\text{COCHCOCH}_3)_3$ (denoted $\text{Y}(\text{acac})_3$ for its double acetate chains), Ba-methoxyethoxide, and Cu-ethoxide [42]. The polymerization of this solution does not require an external agent to assist the gelation due to the long hydrocarbon chains. Other alkoxide compound systems such as Y-propoxide, Ba-ethoxide, and Cu-acetate [43] and others can be used with similar results [44,45,46].

Other combinations of alkoxides are possible to be used such as Y-isopropoxide, $\text{Ba}(\text{OH})_2$, and Cu-acetate [47], or the most commonly tried combination, acetates of all three components [48,49,50]. The benefits of acetates are that they are a simple compound with a relatively small hydrocarbon chain attached to them, and they are miscible in various solvents such as H_2O , methanol and methoxyethanol. A sample acetate molecule is shown in Figure 1 with R being the metal to be attached to the acetate molecule. For Barium or Copper, there would be two sets of these molecules combined and the metal would then be in

the center of the molecule. An example of a similar molecule will be shown later when the system used in the sol-gel portion of this dissertation is described.

Variations on acetates using hydroxide for one of the precursors [51] have been attempted, and the results are promising. The benefit of having the hydroxide chemical precursor is that the pH of the solution will not be as acidic as compared to only using acetates in the solution. The gelation process proceeds much quicker with a pH of approximately 7, or a neutral solution. An acidic or basic solution makes applying multiple layers of sol-gel very difficult as the solution tends to etch away previous layers due to the acidic or basic nature of the solution.

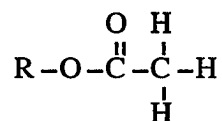
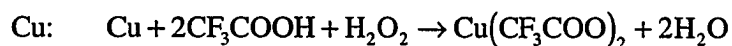
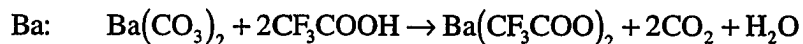


Figure 1: Acetate Molecule

Using the broad definition of sol-gel, another completely different method of preparation of precursors is introduced. Oxides of the three constituent elements in either oxide or carbonate form: Y_2O_3 , BaCO_3 , and CuO are mixed with a mortar and pestle to obtain a homogeneous powder. This powder is then fired to produce the correct phase of the superconductor. Then the superconductor is mixed with a viscous material such as ethylene glycol to create a paste or slurry. This paste is then applied to the substrate via dip coating or various other techniques [52]. This method can also be used for making superconducting castings, tapes, and large electromagnets. However, this technique does not lend itself easily to thin film technology.

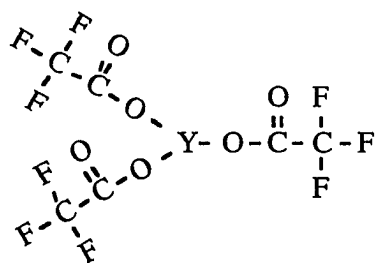
The sol-gel chemical system that is being used in this dissertation is the Y-trifluoroacetate, Ba-trifluoroacetate, and Cu-trifluoroacetate system after a paper by Gupta et

al. [53]. A visual representation of these molecules is shown in Figure 2. To create these complex precursors, Y_2O_3 , $Ba(CO_3)_2$ and Cu metal were mixed with trifluoroacetic acid (CF_3COOH). The processes are outlined below:

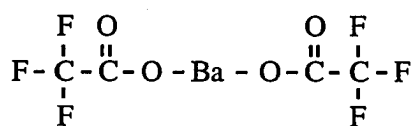


After the aqueous solutions are thoroughly mixed, they are evaporated to dryness. Methanol is then added to the dried compound to create the liquid solution. The reason for using methanol is that methanol "wets" substrates which alleviates the need for a surfactant.

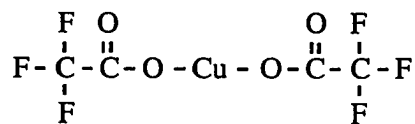
Another reason for avoiding using the aqueous solutions is that they will react with each



Yttrium trifluoroacetate



Barium trifluoroacetate



Copper(II) trifluoroacetate

Figure 2: Trifluoroacetate Molecules

other, and produce precipitates, which has been determined experimentally. Gravimetric analyses are performed on the solutions to verify the concentration before mixing. A description of gravimetric analysis and a sample calculation may be found in Appendix B. This calculation is performed to reaffirm that all the chemical has reacted in the solution, and if there is not complete reaction, the gravimetric analysis will yield the best approximation as to the concentration of the solution. After the chemicals are mixed in the proper proportion (Y=1, Ba=2, Cu=3), the solution is concentrated. Due to the high vapor pressure of methanol, the solution concentrates quickly with little or no heating required. The viscosity of the sol is approximately 50 centipoise which is the maximum viscosity for this system before precipitates form. When precipitates form, an addition of methanol and subsequent heating of the sol will re-dissolve the precipitate.

The next step in sol-gel processing is to fabricate the thin film of superconductor. Except for the slurry approach, all of the sol-gel processing requires a post-processing high temperature annealing or firing up to temperature of $\sim 850^{\circ}\text{C}$ or greater. Therefore, all the techniques must be suited to incorporate this step into the processing of the superconducting material. A few of the techniques of sol-gel processing will be presented.

The most common technique quoted in the literature is that of dip-coating. This technique is performed by "dipping" a substrate into a container of the solution and then drying the layer. Multiple layers may be applied with repeated dippings. Similar in approach to dip-coating is that of spin-coating, which is used in this dissertation. The benefits of spin-coating are identical to that of dip-coating with the addition of uniformity of layers and also the controllability of the thickness. By varying the speed of the spinning and the concentration of the solution, the thickness may be controlled with high reproducibility.

The other method of sol-gel processing is the creation of fibers. Since the solution can be concentrated to a high level of viscosity, the fibers may be extruded from the solution by simply drawing from the viscous sol by placing a glass rod into the sol and drawing the

fibers up [12]. The fibers can then be fired by suspending them from an alumina bar in a furnace to prevent them from losing shape. The author has experience making superconducting fibers at the 3M Company, but due to agreements of confidentiality, results can not be presented. The fibers that were produced had difficulty retaining their shape and cohesion through the firing process due to the loss of organics. When the fibers are heated, the organics leave the fibers and then are burned out in the firing cycle. This process created very porous fibers, and due to the nature of the ceramic superconductors, the fibers were very brittle. This "outgassing" of organics is present also in the thin film sol-gel processing, but the effects are not as critical due to the presence of the substrate to stabilize the structure.

There are a couple of measurements that may be made on the specific sol-gel processing variables to achieve comprehensive results. Viscosity measurements are required to enhance reproducibility and to characterize the spin-on film. Thermo-gravimetric analyses should be performed to determine when the organics burn out of the structure and to determine when the auxiliary phases are formed. Thickness measurements need to be performed to determine the optimum speed and viscosity of the solution for spin-on techniques. When all of these variables are determined, the sol-gel component of the superconductor may be isolated.

After the processing method has been decided, the substrate must be chosen. There are a variety of substrates that can be used to grow superconductors, and all have qualities that require trade-offs. Some of the characteristics that must be weighed are those of lattice parameters, dielectric constant, and thermal expansion. Table 1 gives a summary of some of the popular high temperature superconductor substrates [3].

Other substrates have been explored due to future needs and desired characteristics. Superconducting films have been produced recently on Silver metal [4]. The reason for this choice is to incorporate a metal with the substrate to increase the high temperature ($T > T_c$)

Table 1: Phase Composition of the Products of Interaction of $Y_1Ba_2Cu_3O_{7-x}$ with Some Oxides Used as Materials for Substrates of Thin Superconducting Films [3]

No.	Superconductor	Oxide for substrate	Identified phases
1.	$Y_1Ba_2Cu_3O_{7-x}$	ZrO_2	ZrO_2 , $BaZrO_3$, CuO, YSZ
2.	$Y_1Ba_2Cu_3O_{7-x}$	$\alpha-Al_2O_3$	Al_2O_3 , $BaAl_2O_4$, CuO
3.	$Y_1Ba_2Cu_3O_{7-x}$	$SrTiO_3$	$SrTiO_3$, $Y_1Ba_2Cu_3O_{7-x}$, $Y_1Ba_3Ti_2O_{8.5}$
4.	$Y_1Ba_2Cu_3O_{7-x}$	MgO	MgO, $Y_1Ba_2Cu_3O_{7-x}$, traces of Y_2BaCuO_5

conductivity and to create a superconductor with a high pinning force which in turn create material with very high critical currents.

Silicon wafers are popular with the semiconductor industry, hence combining superconducting technology with the well-known semiconductor processing technology seems inevitable. Various methods of creating superconductors on Silicon wafers have been attempted. One method calls for the use of a buffer layer of patterned gold to be placed on the Silicon wafer [5]. The superconductor is then deposited onto the entire wafer. The superconductor that is in direct contact with the Silicon wafer does not have good superconducting properties because the Silicon diffuses into the superconductor and thus destroys the superconductor. Where the gold acts as a buffer layer, the superconductor has good qualities, and therefore a patterned wafer of superconducting areas separated by non-superconducting areas is created. Adding buffer layers of other types of materials is another option that works better than the metals listed above. A layer of Ytria stabilized Zirconia, $Y-ZrO_2$, or YSZ, which is lattice matched to the superconductor performs well as a buffer layer [6]. A discussion of spin-on sol-gel buffer layers of $Y-ZrO_2$ will be discussed in the methods section.

Another material consideration for the creation of superconducting devices is that of lithography and etching. High temperature superconductors are hydroscopic, and therefore wet etching could possibly be detrimental to the superconducting films. There are papers which speak of using weak acids to etch superconductors with fairly good results [7]. Dry etching processes are currently being investigated as an alternative to wet chemistry. Two different techniques that have research underway are the processes of laser ablation and reactive ion etching. Laser ablation lithography is the same in principle as the method of laser ablation film deposition. The only exception to this is that in the lithography process, the material that is removed is discarded, and what is left on the surface is then the correct pattern. Reactive ion etching, or RIE, is a process of bombarding the substrate with different ions to dislodge the atoms on the surface. Again, the material is removed from the substrate and the remaining material is the desired pattern. Both of these processes can use standard photolithographic techniques such as spin-on photoresist and standard developer, but the laser ablation has the capability of being computer controlled and removing the material without the use of photoresist.

Other topics in general materials research include the different high temperature superconductor systems such as $\text{Bi}_2\text{Sr}_2\text{Ca}_1\text{Cu}_2\text{O}_8$ and $\text{Tl}_2\text{Ba}_2\text{Ca}_1\text{Cu}_2\text{O}_8$. In the $\text{Y}_1\text{Ba}_2\text{Cu}_3\text{O}_{7-x}$ system, substituting Nd for Y has been attempted with marginal results when compared to the $\text{Y}_1\text{Ba}_2\text{Cu}_3\text{O}_{7-x}$ superconductor [8]. Other researchers are focusing their efforts in analyzing the various interactions with substrate materials including metals and other ceramics as mentioned above. The most intriguing research is the addition of Ag to the superconducting formula in various weight percents. The transition temperature did not change dramatically until large amounts of Ag was added to the chemical formula. The remarkable change occurred in the critical current measurement which increased by a factor of two [9].

Another concern of materials research is that of the firing schedule for those processes that require a post processing anneal procedure. There are many studies that have analyzed the loss of carbon, solvents, and other carrier compounds with firing temperature. There are many different firing schedules and many different explanations to justify the differences in firing time and temperature. The reason for the variety in firing schedules is the ternary phase diagram of the HTSC. The Phase diagram for the $Y_1Ba_2Cu_3O_{7-x}$ is shown in Figure 3 [63], where 123= $Y_1Ba_2Cu_3O_{7-x}$, 211= Y_2BaCuO_5 , and 132= $YBa_3Cu_2O_{7-x}$. As can be seen, there are a variety of phases and intermediates which must be accounted for. With the author's experience working with superconductors, and using a consensus of most of the papers surveyed, a firing schedule was formulated. The effects of O_2 in the creation of the superconductor structure have not been fully analyzed, although since oxygen is needed in the compound, an abundance of oxygen has been found to promote growth of the superconductor.

The materials research in the field of HTSCs is varied and still a debatable subject. There is no clear cut best compound, substrate, method, or firing schedule for these HTSCs. Therefore, research is needed that must be done to help answer the questions to find the superior properties of the high temperature superconductor.

II.B. Applications

The applications for superconductors will be classified into two main areas of interest: 1) Where high current density is required, and 2) where good quality thin films are needed. Both of these cases take into account the need for little or no resistive losses. The first area deals mainly with bulk superconductors and such applications as power lines and large electromagnets. The second area of applications will be focused on, since this is the main area of interest in this dissertation. Samples of microwave devices that can be

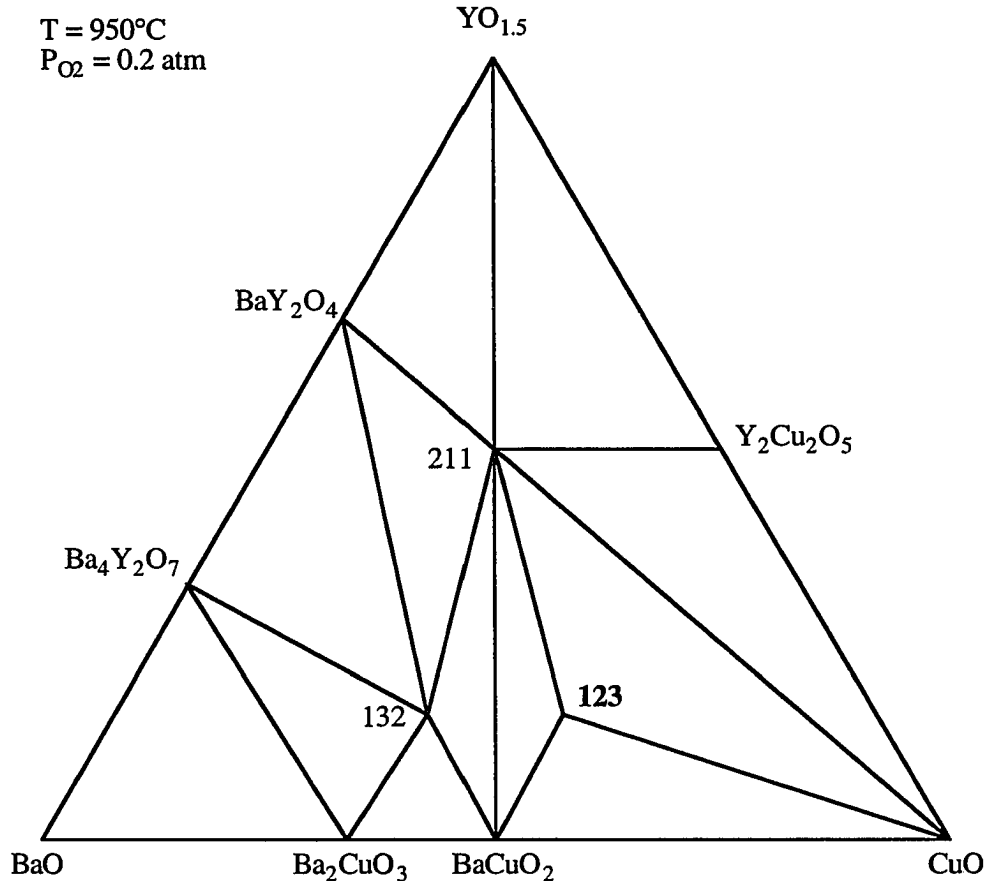


Figure 3. The YO_{1.5}-BaO-CuO pseudoternary phase diagram at 950°C in air. [63]

fabricated from superconducting thin films are filters, resonators, oscillators, phase shifters, and antenna elements.

Josephson Junctions are a special application of superconductors for which the results from paper to paper are very materials dependent. A recent paper by Martens et al. [10] speaks of a superconducting-normal-superconducting Josephson Junction with CaRuO₃ as the separating junction layer. CaRuO₃ was chosen for this center layer because the lattice constant is similar to Y₁Ba₂Cu₃O_{7-x}, the chemical composition does not affect the Y₁Ba₂Cu₃O_{7-x}, and it is a metallic material. Josephson Junctions are very simple devices in

theory, and are also easy to fabricate. There are many examples of such devices throughout the literature.

Superconducting filters have been reported with promising results [11,12,13,14,15]. Various types of filters have been created such as a coplanar waveguide filter, a microstrip filter, and a stripline filter. The unloaded Q of the superconducting resonator reached a peak value of 10,000 in one example of a stripline six-pole elliptic-function filter [12]. These filters will have enormous effects on superconducting circuits with the benefits of increased efficiency and low noise for high frequency circuits.

Microwave resonators are another application for these high temperature superconductors. Different examples of resonators appear currently such as ring resonators [16,17], microstrip resonators [18,19], stripline resonators [20,21], and waveguide resonators [22]. HTSCs are ideal for microwave resonators since they have properties of a high Q value, which leads to low surface resistance, and low power dependence [18]. High temperature superconductors increase the Q of a microstrip resonator by more than a factor of 50 at 1 GHz and by a factor of 20 at 10 GHz as compared to resonators made by replacing the superconductor with gold [19]. With this level of performance available using high temperature superconductors, the potential for use in high sensitivity circuits seems inevitable.

Superconducting transistors are still being investigated heavily in the literature. There are two classes of superconducting transistors: A superconducting base bipolar-type transistor, and a field effect transistor using an oxide below the superconductor. Both of these structures use resonant tunneling as the transport property for the device [23,24,25,26]. The last type of superconducting transistor mentioned in the literature is a vortex flow transistor [27]. This device can be viewed as the magnetic dual of the field effect transistor from a small signal equivalent circuit.

Microwave detectors can be as basic as a block of superconducting material, or they can be as complex as a microwave detector set to receive a specific frequency. Konopka et al. [28] created a microstrip resonator and received millimeter waves with a high level of efficiency, although above 300 GHz the devices did not function well.

The last microwave application to be discussed is the microwave antenna. There has not been a large volume of research done on superconducting antennas, most likely due to the difficulty in fabrication. A paper describing a superconducting meander antenna by Chaloupka et al. [29] yields good results with an increase in efficiency and Q factor compared to copper metal. The largest benefit for superconducting antennas is that the physical size of the antennas may be decreased dramatically.

Future applications will be modifications and improvements on these fundamental microwave devices. A better understanding of superconductors may yet yield increasingly improved results for these high temperature superconductors. A single limiting factor in the application of high temperature superconductors may be the cost of refrigeration down to the temperature of liquid nitrogen. The steps required to achieve this cooling may put high temperature superconductors out of the commercial market until a new class of superconductor is found which will operate at room temperature. Until then, the end user for the type of device proposed in this dissertation will most likely be governmental agencies, the military, space programs, and research institutions.

III. THEORY

III.A. Experimental Models

The presence of superconductivity has been a theory since resistivity measurements were carried out on Mercury by Kamerlingh Onnes in 1911 [30]. He observed that at a temperature slightly below 4.20°K the resistance of a Mercury filament dropped abruptly by a factor of 1000. He assumed that the metal had passed into a new state and called it the "superconductive state." From these early beginnings, scientists have been explaining theories of superconductivity with varied success. In this section, a summary of the theories of superconductivity will proceed from well-established theories and papers as they relate to high temperature superconductors and microwave properties of superconductors.

Overall, there are many different aspects and phenomena of superconductivity pertaining to the new high temperature superconductors such as the Meissner effect, the isotope effect, and zero resistance. A brief summary of these phenomena will be given below along with its relation to the microwave properties of superconductors.

Zero resistance is the most common characteristic quoted in all papers. The transition from normal conducting resistive state is the most pronounced effect and allows current to pass through the sample with little or no resistive loss. The critical temperature, T_c , is a function of zero resistance and is defined as the temperature where the sample makes the transition from a normal conducting state to the superconducting state. A fictional sample plot for resistance vs. temperature for a fictional sample is shown in Figure 4.

Zero resistance will not give conclusive evidence of a superconducting transition. The magnetization reaction of the superconductor is also required to properly describe the superconductor. The Meissner effect is used to show that a sample has indeed passed

through the superconducting transition. Meissner and Ochenfeld demonstrated that a superconducting sample would expel magnetic flux, rather than trapping the flux. More recent data shows that flux is expelled from all but the top $\sim 400\text{\AA}$ of the sample which is defined as the penetration depth, λ [31]. The penetration depth is a function of the material quality, and the frequency of the measurement [33].

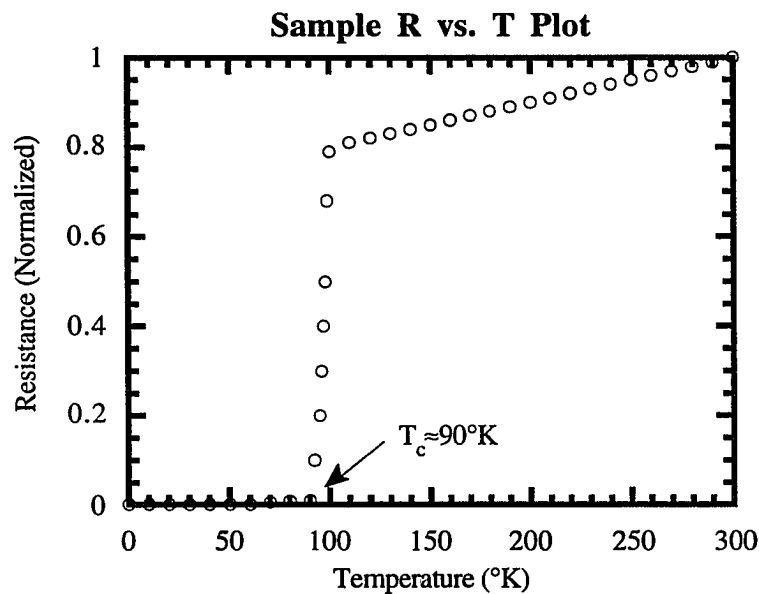


Figure 4: Ideal R vs. T plot

The isotope effect deals with the superconductivity of different materials, which are mostly metals. The theory states that $T_c \approx M^{-\alpha}$ where $\alpha \approx 1/2$, M is defined as the atomic mass of the element, and T_c is the critical temperature of the sample. The effect is useful in describing the theory of superconductivity, but is not useful for practical purposes.

III.B. Microwave Superconductor Theory

The microwave dependence of superconductors in accordance with these theories is easy to describe. First, there is no isotope effect in the new HTSCs. Second, the zero resistance phenomenon is crucial in determining the effect of the superconductor on the microwave properties of the device in question. If the sample has not passed through the transition temperature, then the microwave properties of the device may not be usable due to the losses inherent in the superconductor above the critical temperature. Lastly, the Meissner effect is important for both determining the properties of the high temperature superconductors, as well as inherent in the functionality of the devices. A microstrip bulk acoustic wave resonator needs to have good conductors to support resonance between the parallel plates, and having a superconducting conductor for both plates will theoretically confine both the electric and magnetic fields within the device, thus increasing the efficiency and the quality factor, or Q , of the resonator.

Different theories about microwave properties of superconductors are very common in the literature. Topics and analyses include microstrip lines, transmission lines, stripline resonators, and a couple of different theories on a two-gap structure for superconductors, and a theory of describing superconductors as a negative dielectric material. These topics will be discussed below.

Transmission lines and microstrip lines are a standard in microwave engineering and high frequency circuits. The analysis of these structures, including the current density, magnetic flux density, and quality factor (Q) as variables of operating frequency and strip width are changed are the topic of many papers in this area. Most of these theories use the simplifying assumption that the thickness of the film is much greater than the penetration

depth, λ . If this assumption does not hold, then the complexity of these formulas derived from BCS theory make them impractical to use. [33]

Stripline resonators can be used for a number of applications and also for the electrical characterization of HTSCs. Their structure is similar to microstrip lines, but their geometry and analysis is somewhat more complicated than microstrip resonators. These devices are simple to fabricate, they easily demonstrate the microwave properties of superconductors, and they have been in the literature since 1989 (for HTSC). Stripline resonators eliminate the radiation losses associated with microstrip lines, and they also have the advantage of planar fabrication techniques, with the resonant frequency determined photolithographically.

A paper by Kresin et al. [32] illustrates the variety of theories and analyses available to analyze HTSCs. In this paper, they discuss a theory that $Y_1Ba_2Cu_3O_{7-x}$ has two conductive sub-systems: Planes and chains, thus resulting in a two-gap structure for the electrical characteristics. The chains in this theory represent a conductive metallic subsystem, while the planes are a pure superconductor.

Another paper by Mei and Liang looks at the analytical suggestion that the superconductors can be modeled as a negative dielectric material, rather than just a low loss conductor [33]. By having a negative real component to the dielectric constant, the data and measurement suggest that this theory could be valid in some cases.

Two papers have theories which relate closely to the application described in this dissertation. One paper is by Lee et al. [34] which models superconductors along with giving a good overview of the current analyses of microwave superconductor theory. The other paper is by Pond and Weaver [35] and models the field and energy-density profiles in a layered structure. This theory is similar to the theory developed in this dissertation.

III.C. Mason Model Theory

To calculate the resonant frequency of the HTSC - piezoelectric device, the Mason model is used. [62] The Mason model is an approximation for the acoustical wave produced by the piezoelectric AlN. The assumptions taken into account are that the velocities of the waves in the piezoelectric, the polarization coupling constants, and the impedances of all waves in all materials are known. It is also assumed that only one mode is propagating. For simplicity, a one dimensional Mason model is used.

The Mason model translates the acoustical portion of the device into an electrical equivalent that may be simulated using standard high frequency electromagnetic software. The premise used by the Mason model is a simulation of the acoustic wave of the circuit by assuming that acoustic waves in materials are similar to electric waves in transmission lines, and therefore transmission line theory may be used to simulate the structure. A sample Mason model structure is shown in Figure 5. This example is the model used in the calculation of the resonant frequency and the theoretical performance of the HTSC / AlN / HTSC device, and is the circuit simulated in section III.D.3. The equations governing the Mason model are:

$$Z_1 = jZ_{a-HTSC} \tan\left(\frac{k_{HTSC}d_{HTSC}}{2}\right) \quad (1)$$

$$Z_2 = -j\frac{Z_{a-HTSC}}{\sin(k_{HTSC}d_{HTSC})} \quad (2)$$

$$Z_3 = jZ_{a-AlN} \tan\left(\frac{k_{AlN}d_{AlN}}{2}\right) \quad (3)$$

$$Z_4 = -j\frac{Z_{a-AlN}}{\sin(k_{AlN}d_{AlN})} \quad (4)$$

$$Z_5 = jZ_{a-MgO} \tan\left(\frac{k_{MgO}d_{MgO}}{2}\right) \quad (5)$$

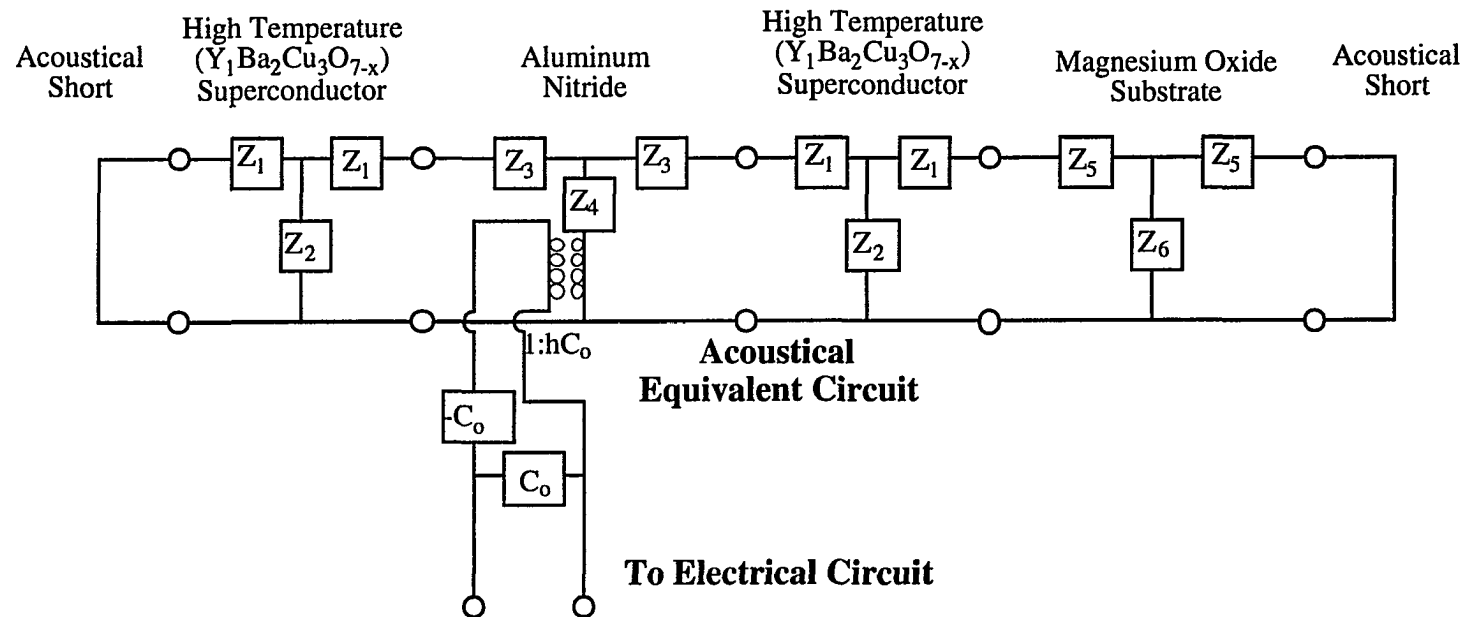


Figure 5: Mason Model equivalent circuit.

$$Z_6 = -j \frac{Z_{a-MgO}}{\sin(k_{MgO} d_{MgO})} \quad (6)$$

$$C_o = \frac{\epsilon_s A}{d_{AlN}} \quad (7)$$

where Z_a is the acoustic impedance of the material (Aluminum Nitride, High Temperature Superconductor, or Magnesium Oxide) which is defined by

$$Z_a = \sqrt{\rho c} A = \rho v_a A = \frac{ck}{\omega} A, \quad v_a = \sqrt{\frac{c}{\rho}} \quad (8)$$

where A = Area of the section

ρ = the material density

c = the relevant stiffness constant of the propagating mode (longitudinal or shear)

v_a = the acoustic velocity of the wave

k = the propagation constant, i.e. $u = a e^{-jkz} + b e^{+jkz}$

d = the thickness of the layer

$h = \frac{e}{\epsilon_s}$ where $e = cd$, c is defined above, and d is the piezoelectric strain matrix

$\epsilon_s = \epsilon_0 \epsilon_r$, ϵ_0 = Permittivity of free space, ϵ_r = relative permittivity of the material

III.D. Transmission Line Analysis

An analysis has been developed by the author that has been presented for a superconducting bulk acoustic wave resonator [64]. This theory will be discussed in detail presently. A copy of this paper, which was presented at the Fall 1994 Materials Research Conference, may be found in Appendix A.

The goal of this analysis is to model a hybrid superconductor piezoelectric resonator structure using transmission line theory. To accomplish this goal, an equivalent circuit must

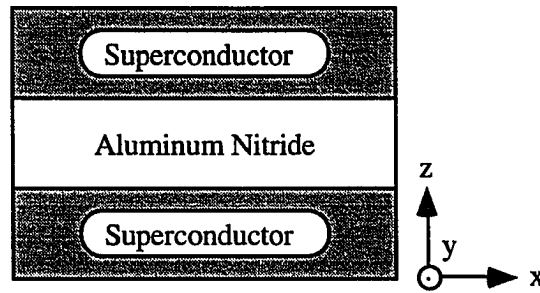


Figure 6: Simplified theoretical HTSC - AlN - HTSC structure

be set up which correctly approximates the entire structure. The structure to be simulated is a High-Temperature Superconductor - Aluminum Nitride - High-Temperature Superconductor resonator structure as shown in Figure 6.

The calculation will be broken down into sections dealing with specific aspects of the analysis. The first section analyzed will be the equivalent inductance of the superconductor. The second part will be the terminating resistance at the free space boundary. The final section will be to add the Mason model to the circuit modeling the piezoelectric resonator and the mass loading effects of the superconductor and the substrate. Shown on the next page in Figure 7 is the electromagnetic model for the superconducting transmission line structure.

There is only a capacitor shown modeling the piezoelectric layer on this model, but on all the capacitor nodes there will be an equivalent Mason model to add the piezoelectric and mass loading effects into the circuit. The Mason model was discussed previously in the theory section.

The results from this analysis agree well with a predicted superconductor analysis, as well as with superconducting theory. The penetration depth is found to be consistent with both measurements and this analysis.

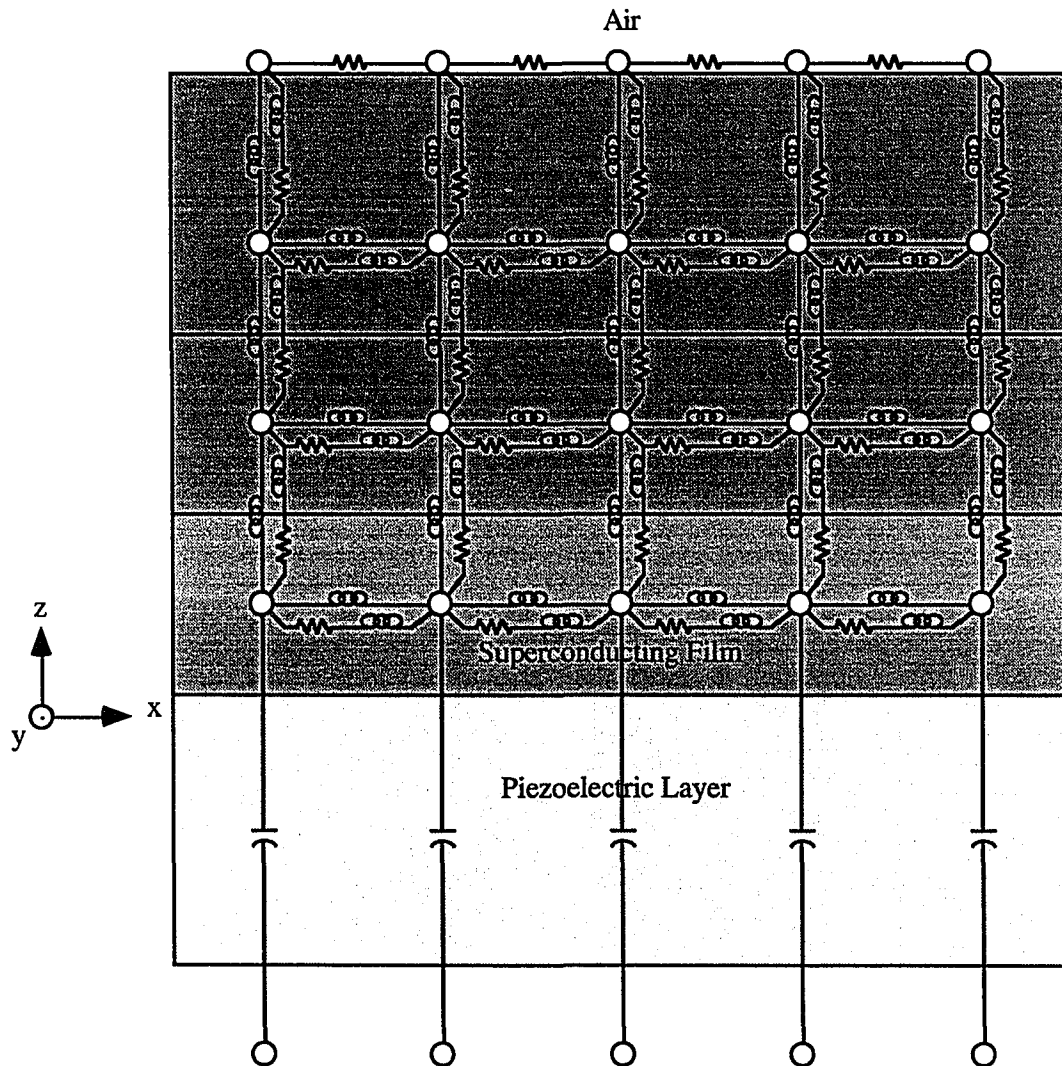


Figure 7: Schematic of the HTSC - AlN Structure

III.D.1. Equivalent Inductance

The intent of the inductor analysis is to find an equivalent circuit element that may be used in the transmission line analysis. A small section of a superconducting sample will be analyzed as shown in Figure 8. Because this material is a conductor, the magnetic field energy is the energy that must be determined. To find an equivalent inductance in the superconducting sample, a current is assumed to flow in only the x - direction. There is assumed to be no variation of the z-component of the magnetic field in the y - direction, $\frac{\partial H_z}{\partial y} = 0$ which greatly simplifies the analysis.

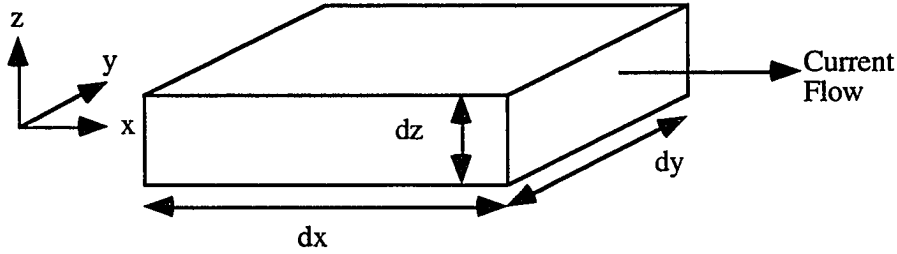


Figure 8: Theoretical superconducting sample

The equation for energy stored in an inductor is

$$W_L = \frac{1}{2} Li^2. \quad (9)$$

The magnetic stored energy in this slab of material is found by using the equation for the magnetic stored energy in a field,

$$W_M = \frac{1}{2} \iiint_V \vec{B} \cdot \vec{H} \cdot dv = \frac{1}{2} \iiint_V \mu H^2 \cdot dv \quad (10)$$

with $\vec{B} = \mu\vec{H}$. Therefore, from equations 9 and 10 we obtain

$$Li^2 = \iiint_V \mu_0 H^2 \cdot dv \quad (11)$$

where $\mu = \mu_0 = 4\pi \cdot 10^{-7}$ henries/meter in high temperature superconductors [30]. To find the magnetic field corresponding to the current in the sample, we use Maxwell's equation in integral form as derived from Ampere's law which states

$$\oint_C \vec{H} \cdot d\vec{l} = \iint_S \vec{J} \cdot d\vec{s}. \quad (12)$$

The solution for the right side of equation 12 is the current passing through the sample. To determine the current components, we use the assumption stated previously that $\frac{\partial H_z}{\partial y} = 0$

and look at the differential current traveling in the x - direction which is also shown in Figure 9.

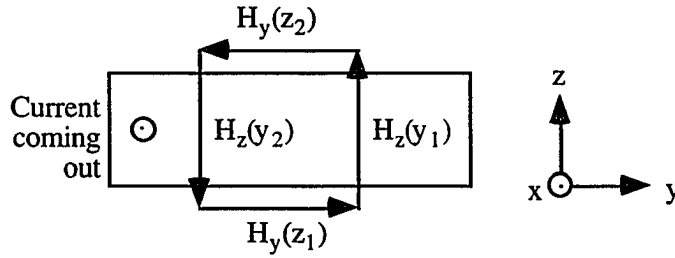


Figure 9: Equivalent magnetic fields through the superconducting sample

Approximating the integrals as differentials, we can evaluate the current as follows.

$$J_x(z) \cdot dy \cdot dz = [H_y(z_1) - H_y(z_2)] \cdot dy \quad (13)$$

$$J_x(z) = \frac{H_y(z_1) - H_y(z_2)}{dz} \approx -\frac{\partial H_y}{\partial z}. \quad (14)$$

Next, we will assume a solution of the following form:

$$\vec{H} = \vec{H}_0 e^{-\alpha z}. \quad (15)$$

The $e^{-j\beta z}$ phase shift term was not considered in equation 15 since the finite difference approach used considers the fields in a local area and not the distributed nature of the field. The distributed nature of the fields then results from solving the total nodal problem of the net mesh. To solve equation 11 for L , we must determine the current, I , in terms of the magnetic field intensity, H . The first step is to define the current in terms of J , which is a basic definition,

$$I = \iint_S \vec{J} \cdot d\vec{s} \quad (16)$$

where only the J_x component of the current density is considered to exist. Then, inserting equation 16 into equation 11 we obtain

$$L \left(\iint_S \vec{J} \cdot d\vec{s} \right)^2 = \iiint_V \mu_o H^2 \cdot dv. \quad (17)$$

Using the differential relationship given in equation 14, equation 17 becomes

$$L \left(\iint_S -\frac{\partial H_y}{\partial z} \cdot ds \right)^2 = \iiint_V \mu_o H_y^2 \cdot dx \cdot dy \cdot dz. \quad (18)$$

Using the form of the magnetic field assumed by equation 15 in the y - direction, $H_y(z) = H_o e^{-\alpha z}$, this equation will be simplified. To do this we will break equation 18 into two parts. The first part to be evaluated will be the right hand side, therefore using equation 15 in the right side of equation 18 we obtain,

$$\begin{aligned} \iiint \mu_o H_y^2 \cdot dx \cdot dy \cdot dz &= \iiint \mu_o (H_o e^{-\alpha z})^2 \cdot dx \cdot dy \cdot dz \\ &= \mu_o H_o^2 \int_0^{\Delta x} \int_0^{\Delta y} \int_z^{z+\Delta z} e^{-2\alpha z} \cdot dz \cdot dy \cdot dx = \mu_o H_o^2 (\Delta x)(\Delta y) \int_z^{z+\Delta z} e^{-2\alpha z} \cdot dz \end{aligned}$$

$$= \frac{\mu_0 H_0^2 \Delta x \Delta y}{-2\alpha} \left(e^{-2\alpha(z+\Delta z)} - e^{-2\alpha z} \right) = \frac{\mu_0 H_0^2 \Delta x \Delta y}{-2\alpha} e^{-2\alpha z} \left(e^{-2\alpha \Delta z} - 1 \right).$$

Expanding the last exponential, the following equation results:

$$\begin{aligned} &= \frac{\mu_0 H_0^2 \Delta x \Delta y}{-2\alpha} e^{-2\alpha z} \left(e^{-2\alpha \Delta z} - 1 \right) = \frac{\mu_0 H_0^2 \Delta x \Delta y}{-2\alpha} e^{-2\alpha z} \left(1 - 2\alpha \Delta z + () + \dots - 1 \right) \\ &\approx \frac{\mu_0 H_0^2 \Delta x \Delta y}{-2\alpha} e^{-2\alpha z} (-2\alpha \Delta z). \end{aligned} \quad (19)$$

Now, expanding the left side of equation 18 using equation 15, we obtain:

$$\begin{aligned} &\left(\iint_S -\frac{\partial H_y}{\partial z} \cdot ds \right)^2 = \left(\int_0^{\Delta y} \int_z^{z+\Delta z} \frac{\partial (H_0 e^{-\alpha z})}{\partial z} \cdot dz \cdot dy \right)^2 \\ &= \left(\int_0^{\Delta y} \int_z^{z+\Delta z} -\alpha H_0 e^{-\alpha z} \cdot dz \cdot dy \right)^2 = \left(\Delta y H_0 \int_z^{z+\Delta z} -\alpha e^{-\alpha z} dz \right)^2 \\ &= \left(\Delta y H_0 \left(e^{-\alpha(z+\Delta z)} - e^{-\alpha z} \right) \right)^2 = \left(\Delta y H_0 e^{-\alpha z} \left(e^{-\alpha \Delta z} - 1 \right) \right)^2 \\ &= (\Delta y)^2 H_0^2 e^{-2\alpha z} \left(e^{-\alpha \Delta z} - 1 \right)^2 = (\Delta y)^2 H_0^2 e^{-2\alpha z} \left(1 - \alpha \Delta z + \dots - 1 \right)^2 \\ &\approx \alpha^2 (\Delta y)^2 (\Delta z)^2 H_0^2 e^{-2\alpha z}. \end{aligned} \quad (20)$$

Taking the results from equations 19 and 20, and placing them back into equation 18, we can find a value for the incremental inductance of the superconductor:

$$L = \frac{\frac{\mu_0 H_0^2 \Delta x \Delta y}{-2\alpha} e^{-2\alpha z} (-2\alpha \Delta z)}{\alpha^2 (\Delta y)^2 (\Delta z)^2 H_0^2 e^{-2\alpha z}}. \quad (21)$$

Canceling out terms and simplifying, we obtain the following result:

$$L_x = \frac{\mu_0 \Delta x}{\alpha^2 \Delta y \Delta z}. \quad (22)$$

This is the incremental inductance for a current flowing in the x - direction. Similarly, the inductance in the z direction for a z directed current is:

$$L_z = \frac{\mu_0 \Delta z}{\alpha^2 \Delta y \Delta x}. \quad (23)$$

These results are for a sample that is entirely superconducting. In this analysis, the case when the sample is not *entirely* superconducting will be investigated, since for most high temperature superconductors, there remains a small finite resistance that will be accounted for in the transmission line analysis. [33] Figure 10 is a simplified drawing of a superconducting sample with a non-superconducting region. Note that for simplicity of the calculation, it is assumed that the superconducting region contains only superconducting electrons in Cooper pairs, and the non-superconducting region contains no Cooper pairs.

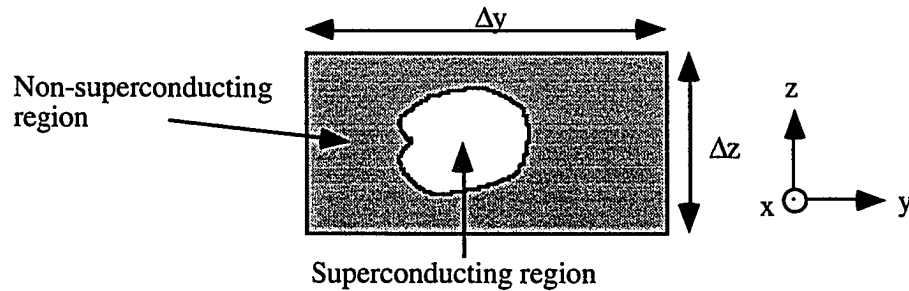


Figure 10: Simplified superconducting - non-superconducting sample.

If only a portion of the area is superconducting, then the effective area of the superconductor will be decreased by a percentage equal to the ratio of superconducting to non-superconducting regions. The area component of equation 22 becomes

$$L_{x-SC} = \frac{\mu_o \Delta x}{\alpha^2 K \Delta y \Delta z}, \quad (24)$$

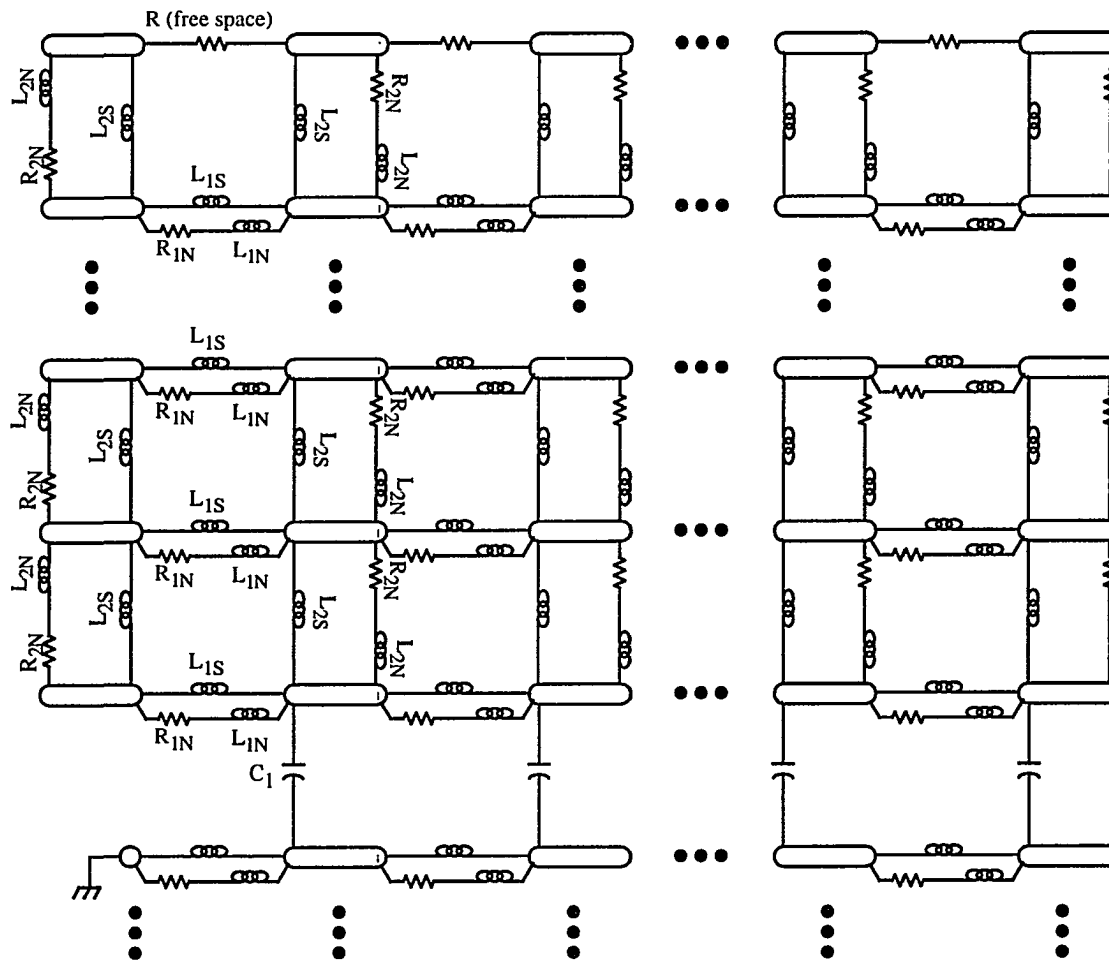
where K is the ratio of superconducting to non-superconducting regions. Similarly, the non-superconducting region will have an inductive component and a resistive component to the impedance which will be given by

$$L_{x-NSC} = \frac{\mu_o \Delta x}{\alpha^2 (1 - K) \Delta y \Delta z} \quad (25)$$

and

$$R_{x-NSC} = \frac{\rho \Delta x}{(1 - K) \Delta y \Delta z} \quad (26)$$

where ρ is the resistivity of the superconductor just before the sample passes through the transition and becomes superconducting. This resistive component is the standard resistance for a non-superconducting block of material. There is no capacitive component considered because in a conducting element, the predominant field energy is magnetic and therefore the capacitance is not significant compared to the inductance. These components can then be combined in a differential circuit element as described in section A and shown in Figure 12 where L_{SC} is defined by equation 24, L_{NSC} is defined by equation 25 and R_{NSC} is defined by equation 26. Note that there is no R_{SC} since when the sample becomes superconducting, it is assumed that this portion has no resistance to it. The entire structure is shown in Figure 11. The free-space terminating resistor at the top of the model will be discussed next.



Same as above

Figure 11: Equivalent superconductor structure model

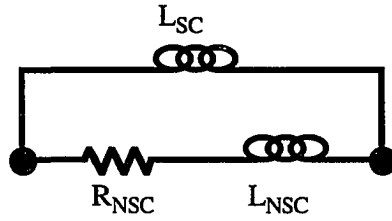


Figure 12: Superconducting / Non-Superconducting equivalent circuit

III.D.2. Resistance at the Interface

The equivalent resistance at the free space boundary of the sample simulates the power lost into the half space that may be used in the transmission line analysis. The incremental area of the sample is shown in Figure 13.

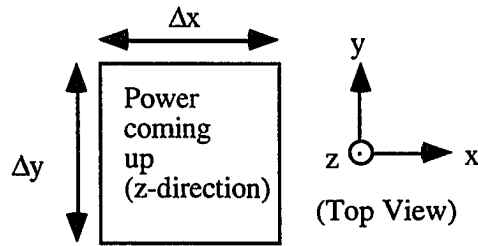


Figure 13: Superconductor section for resistance measurement

The method used to analyze the equivalent resistance at the superconductor - air interface will be to look at the power in free space at the boundary. The theory for this analysis is to model the resistance in free space away from the superconductor and then to bring the resistance close to the superconductor maintaining the continuity of electric and magnetic fields across the boundary. To look at the attenuation at the boundary of the sample, we start with the Poynting vector in the z direction:

$$\vec{P} = \vec{E} \times \vec{H}, \quad (27)$$

which for the example of Figure 13 can be expressed as

$$P_z = E_x \times H_y, \quad (28)$$

in free space. To relate E_x and H_y , we use the relations that in free space,

$$H_y = \frac{E_x}{\eta}, \quad (29)$$

where

$$\eta = \sqrt{\frac{\mu_0}{\epsilon_0}} = \sqrt{\frac{4\pi \cdot 10^{-7}}{8.854 \cdot 10^{-12}}} = 377\Omega. \quad (30)$$

Therefore, equation 28 becomes

$$P_z = E_x \times \frac{E_x}{\eta} = \frac{E_x^2}{\eta}. \quad (31)$$

The total power comes from multiplying equation 31 by the area of the sample, or $\Delta x \Delta y$.

The standard power equation for a resistor is

$$P = I^2 R = \frac{V^2}{R}. \quad (32)$$

Converting the voltage across a resistor back to an electric field by using Maxwell's equation in integral form we obtain the result

$$\sum V = \oint_C \vec{E} \cdot d\vec{l}, \quad (33)$$

which can be interpreted as the voltage drop across the resistor is equal to the electric field multiplied by the distance, or

$$V = -\int \vec{E} \cdot d\vec{l} = -E_x \Delta x. \quad (34)$$

Therefore, with the voltage defined by equation 34 we can find the power from equation 32 in terms of the electric field as follows,

$$P = \frac{V^2}{R} = \frac{E_x^2 \Delta x^2}{R}. \quad (35)$$

Now equating the power from equations 31 and 35 we can define the differential resistance at the superconductor - air interface by

$$P = \frac{E_x^2 \Delta x \Delta y}{\eta} = \frac{E_x^2 \Delta x^2}{R}$$

$$R = \frac{\eta \Delta x}{\Delta y}. \quad (36)$$

III.D.3. Mason Model Analysis

In Figures 7 and 12, there is a capacitor across the Aluminum Nitride structure. This is not entirely correct, since there are other effects of the piezoelectric resonator structure such as mass loading. In a piezoelectric, the electric field interacts with the crystal structure of the lattice creating stress and strain across the lattice. The model chosen is the Mason Model as discussed in section III.C.

The electrical connections of the Mason model will connect to every port in the x - direction of the simulated structure between both the top and bottom superconductor layer. The equations governing the Mason model are described in detail in section III.C. The specific material constants are shown in Table 2. Note that all of the values for c, or the stiffness component, are given for the longitudinal mode of the material in question.

Note that both the piezoelectric and acoustic loading effects are taken into account in the Mason model, thus yielding an accurate result. The resulting electrical equivalent circuit for the Mason model is a reactance in parallel with a resistance. This lumped equivalent

circuit element accurately models the acoustic effects of the different layers, and introduces these effects correctly into the transmission line analysis.

To simulate this Mason model, a Libra^(TM) [68] circuit was designed that corresponds directly with the Mason model and is shown on the next page in Figure 14. These equations and variables are derived from the acoustical circuit equations found in section III.C and are shown in Figure 15.

Some of the equations in Figures 14 and 15 deserve further explanations. The acoustic impedance of each element is determined by

$$Z_o(\text{material}) = \text{area} \cdot \sqrt{c(\text{material}) \cdot \rho(\text{material})}. \quad (37)$$

Table 2: Material Constants for the Mason Model

Constant	Value	Explanation	Reference
c(AlN)	3.95e11 N/m ²	Stiffened c from c33 for AlN	[67]
c(MgO)	2.86e11 N/m ²	c33 for MgO	[67]
c(SC)	1.38e11 N/m ²	c33 for HTSC	[66]
ρ (AlN)	3270 kg/m ³	Density of AlN	[67]
ρ (MgO)	3650 kg/m ³	Density of MgO	[66]
ρ (SC)	5985 kg/m ³	Density of HTSC	[67]
t(AlN)	3.574 μm	Thickness of AlN	-
t(MgO)	100 μm	Thickness of MgO	-
t(SC)	0.5 μm	Thickness of HTSC	-
dx	20 μm	Lateral dimension	-

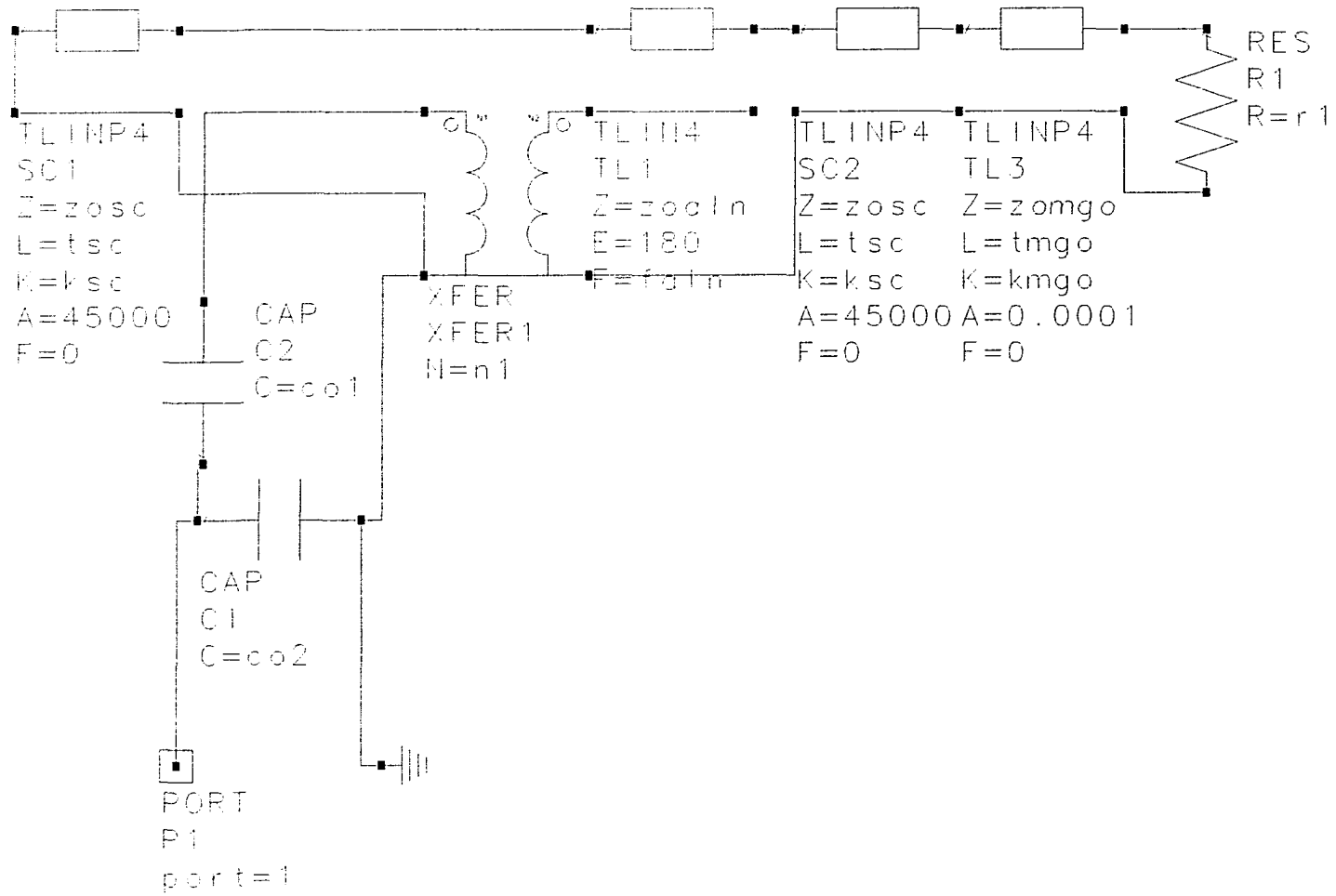


Figure 14: Mason Model simulated on Libra

```

DATA
TEMP
TEMP_DEFAULT
TEMP=16.85

```

```

DATA
RREF
RREF_DEFAULT
R=100000

```

IMPORTANT

- 1) If your Defaults window name is anything other than "defaults.jsn", it must be open in order to be associated with a simulation.
- 2) A test bench or test lab refers to the Defaults window for its units, variables and equations.
- 3) The reserved variables such as "_freq2", "_bias1", etc. can only be defined in the Defaults window.

```

UNITS
UNITS_DEFAULT
FREQ=GHz
RES=Ohm
COND=S
IND=H
CAP=F
LNG=m
TIME=psec

```

```

ANG=deg
POWER=dBm
VOLT=V
CUR=mA
DIST=m

```

Var
Eqn

```

VAR
_VAR
cain=395000000000
r1=1e-7
e=1.55
eain=9.5e-11
dain=3270
tain=3.574e-6
tsc=5e-7

```

```

dsc=5935
csc=138000000000
cmgo=386000000000
dmgo=3650
tmgo=1e-9
c=299792000
a.=2e-5
area=d.*d
cbar=cain+(e**2)/eain

```

```

ca2=eain*area/tain
ca1=1*ca2
a2=e*area/tain
n1=1/n2
zain=area*cbar*sqrt(dain/cbar)
zosc=area*csc*sqrt(dsc/csc)
zomgo=area*cmgo*sqrt(dmgo/cmgo)
kain=(c/((zain/area)/dain))**2
kosc=(c/((zosc/area)/dsc))**2

```

```

kmgo=(c/((zomgo/area)/dmgo))**2
fain=(sqrt(cbar/dain)/(2*tain))/1e9

```

Figure 15: Values used in the Libra calculation

The value of k , or the effective dielectric constant used for these materials is calculated by

$$k(\text{material}) = \left(\frac{3 \times 10^8 \text{ m/s} \cdot \text{area} \cdot \rho(\text{material})}{Z_o(\text{material})} \right)^2 \quad (38)$$

Note that the speed of light is used in this equation to convert from the electromagnetic transmission line to the acoustic transmission line for analysis in Libra. Libra also requires a resonant frequency of the AIN to be input. The resonant frequency of the AIN is equal to

$$\text{frequency(AIN)} = \frac{\sqrt{\frac{c(\text{AIN})}{\rho(\text{AIN})}}}{2 \cdot t(\text{AIN})} \quad (39)$$

It was found experimentally that the value for the width and length value, which are set equal to each other in this analysis, must be greater than 7 μm to prevent round-off errors in Libra. The acoustic loss for the superconductor was estimated to be approximately equal to that of Aluminum. To the first order, this loss will not affect the resonant frequency of the resonator, but it will affect the resistive portion of the equivalent circuit. The thickness of the Aluminum Nitride was varied until the resonant frequency reached 1 GHz. It should be noted at this point that the thickness of the MgO was not used in the calculation of the resonant frequency. Adding this thickness will make the resonator structure overmoded, and to determine the actual resonant mode of the Aluminum Nitride in conjunction with the High Temperature Superconductor this value was omitted. However, Libra can accurately account for the thickness of the MgO, but this analysis was not pursued. The values for the real and imaginary admittance were found, as shown on the graph on the next page in Figure 16. The S_{11} reflected magnitude was plotted on a Smith Chart where the resonance can be easily seen in Figure 17. Note that the lossless Mason model was used to simulate this structure. Losses were added to the analysis on Libra for the acoustic properties of the high temperature

superconductor after the Mason model was calculated. This loss was an estimate of the acoustic loss in the superconductor and was estimated as the loss of Aluminum. This value was somewhat arbitrary and was only used to input some acoustic loss. As will be explained later, this value should have been increased to simulate a larger acoustic loss.

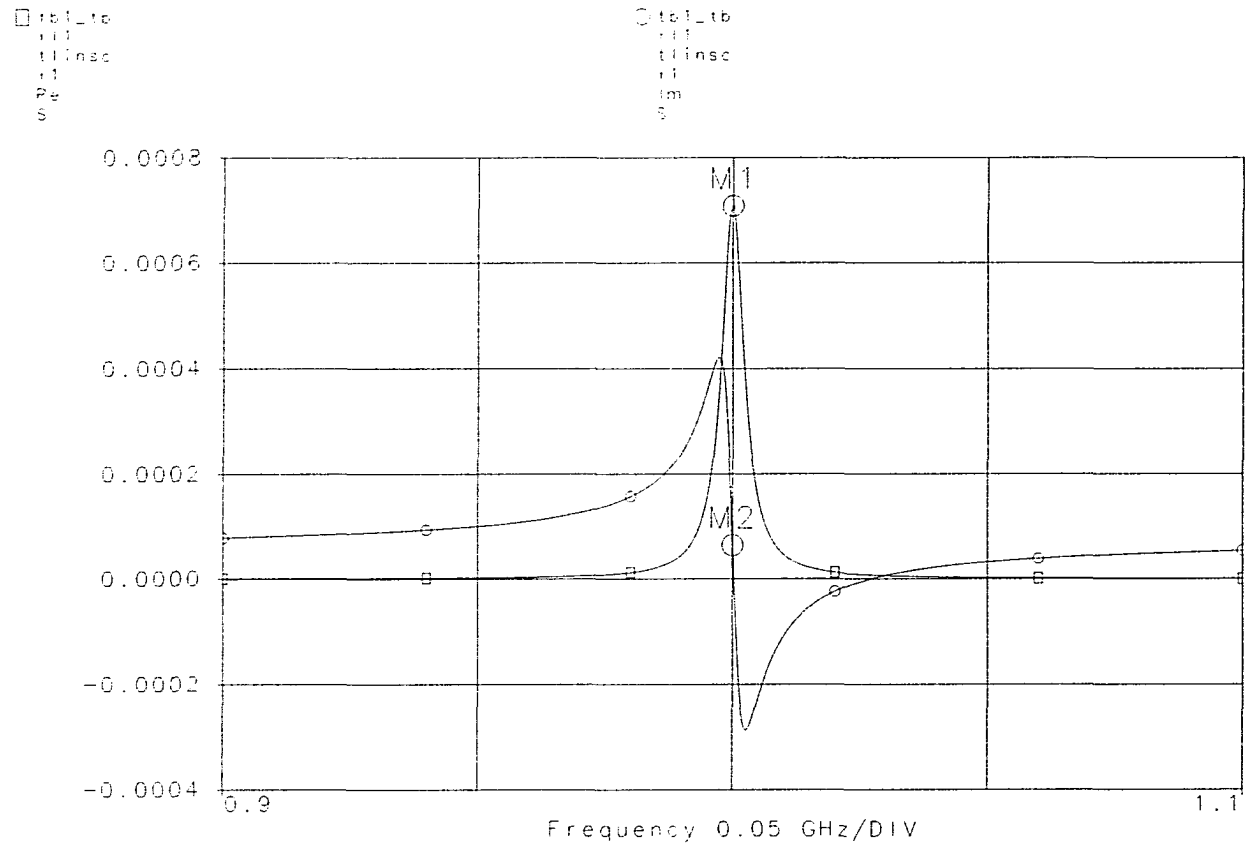
The values for the real and imaginary admittance were found at the resonant frequency of 1 GHz and are equal to $Y_{\text{resonance}} = 707.88 + j64.60 \mu\text{S}$ for the area used, where resonance is defined as the point at which the real component of the impedance reaches a maximum. This is the acoustical equivalent to the HTSC - AlN - HTSC circuit for a $20 \mu\text{m} \times 20 \mu\text{m}$ square at the HTSC - AlN interface. This result can be seen in Figure 16. This calculated result replaces the capacitor impedance of the AlN in Figures 7 & 12 and models the physical parameters of the piezoelectric.

III.D.4. Theoretical Results

A FORTRAN code was written taking all of these elements into account. The code is given in Appendix D. The strategy to solving this circuit was to input the admittance of each of the elements into the array, and then invert the array to obtain the impedances at each point in the matrix,

$$[Y]^{-1} = [Z]. \quad (40)$$

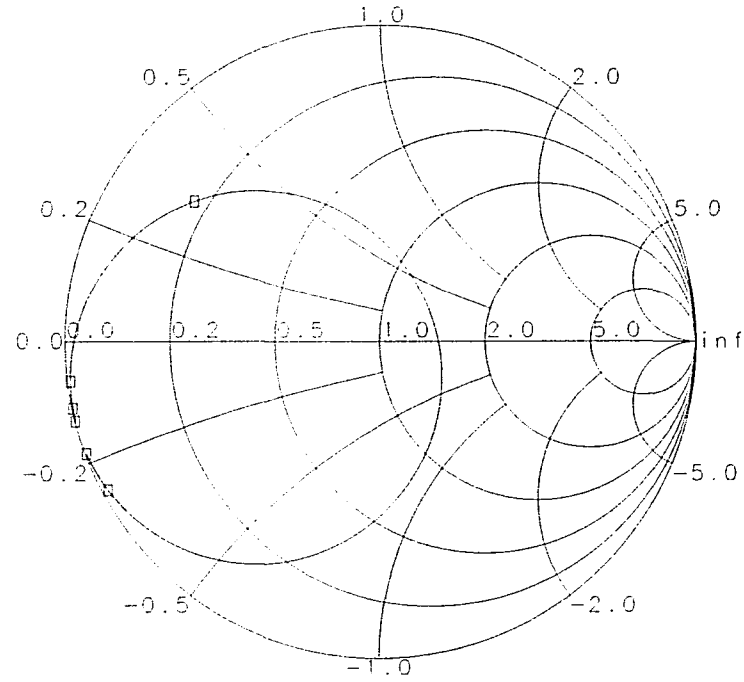
All the impedances are then referenced to the first upper node to have a plane of reference. The next step was to assume a 1A current passing into the sample. Using these assumptions, the potentials across the sample are equal to the impedance values of the Z matrix. With the assumption stated above, currents and electric field potentials at points in the sample may be found as follows.



dx = 20 um t_{aln} = 3.574 um
M1 Frequency=1.00000000 value=0.00070788
M2 Frequency=1.00000000 value=0.00006460

Figure 16: Admittance parameters from Libra
Y(Aluminum Nitride) @ 1 GHz = 707.88 +j64.60 μS

```
□ tbi_tb  
SIUJ  
tlinso  
S[1,1]
```



Frequency 0.9 to 1.1 GHz

$Z_0 = 100 \text{ k}\Omega$

$d_x = 20 \text{ }\mu\text{m}$ $t_{\text{aln}} = 3.574 \text{ }\mu\text{m}$

Figure 17: Smith Chart output from Libra

Current:
$$I = \frac{\Delta V}{Z} = \Delta V \cdot Y = (V_1 - V_2) \cdot Y_{12} \approx (Z_1 - Z_2) \cdot Y_{12}$$

Electric Field:
$$E = \frac{\Delta V}{dx} = \frac{V_1 - V_2}{dx} \approx \frac{Z_1 - Z_2}{dx}$$

The impedance values were referenced to the first node, with the first node using the self-impedance at that node. Translating the admittances and impedances was performed using an augmented matrix analysis and grounding the lower superconductor at the corresponding first node below the reference node of the upper superconductor. This can be seen in Figure 11.

Values for the specific elements and some of the parameters for analyzing the circuit were found from the literature or were obtained from Libra, and are outlined below.

- $\Delta x = \Delta y = \Delta z = 20 \mu\text{m}$
- $\alpha = 1/\lambda$, where λ is the Superconducting penetration depth, $\lambda = 925 \text{ \AA}$ [58]
- $\rho =$ Resistivity of the superconductor just before superconducting, $\rho = 4 \times 10^{-4} \Omega\text{-cm}$ [58]

To calculate the current density, the current entering each node was analyzed, and the vector sum shows where this magnitude is greatest. The results are shown on the next page in Figure 18. The potential was analyzed in a similar method, and is shown in Figure 19 in the form of a contour plot. Note that this graph shows a large potential drop across the superconductor, but this drop is actually very small. Due to the 1 Ampere current that is assumed to flow through the sample, the resulting potential drop is amplified. Also, note that the potential is negative on the bottom superconductor which adds to the large potential difference across the AlN. The conclusions that may be drawn from these plots are that the current in the superconductor remains near the lower edge of the sample closest to the Aluminum Nitride, and does not propagate above the superconducting penetration depth. The current density plot verifies that there is very little current above the third tier of nodes,

and in the potential plot, the values are even more remarkable. In the potential plot, the potential decreases rapidly both in the z direction, as well as decreasing somewhat in the x - direction. These results verify the penetration depth in showing that the current does not flow in the upper regions of the superconductor above this penetration depth.

This theoretical transmission line presentation verifies that the penetration depth holds firm even in microwave analysis of High Temperature Superconductors. The current analysis shows that the majority of the current flowing in this device is confined to a distance less than the penetration depth. The potential analysis also verifies this conclusion. The potential is highest directly near the AlN - HTSC interfaces and then drops off rapidly. The power in the device is therefore confined to a distance from the AlN - HTSC interface not greater than the penetration depth due to the fact that both the current and potential are likewise confined to this area.

The superconductor may be modeled as a transmission line, while continuing to hold to the theoretical approximations. Using standard transmission line equations and theories, coupled with the assumption of a two component current in the HTSC, a coherent analysis and conclusion may be drawn. Likewise, the Mason model may be applied to High Temperature Superconductors to account for standard piezoelectric and mass loading calculations and analysis. With the acoustical parameters of the HTSC quoted in the literature, standard piezoelectric analysis may commence with a high degree of precision. This high level of precision is also maintained in a HTSC - AlN - HTSC resonator which will be discussed in the methods section.

Superconducting Currents

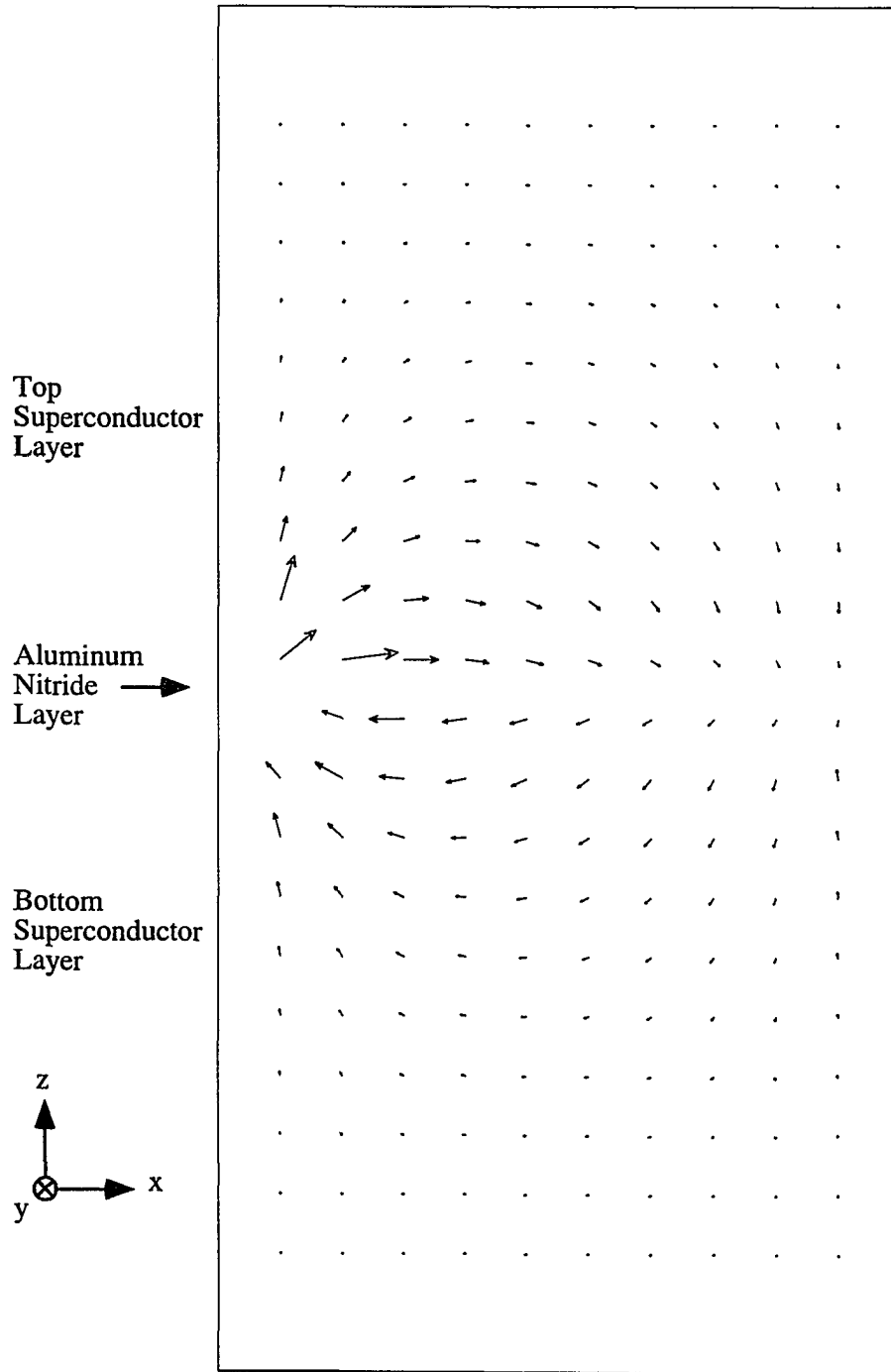


Figure 18: Currents in the superconductor.

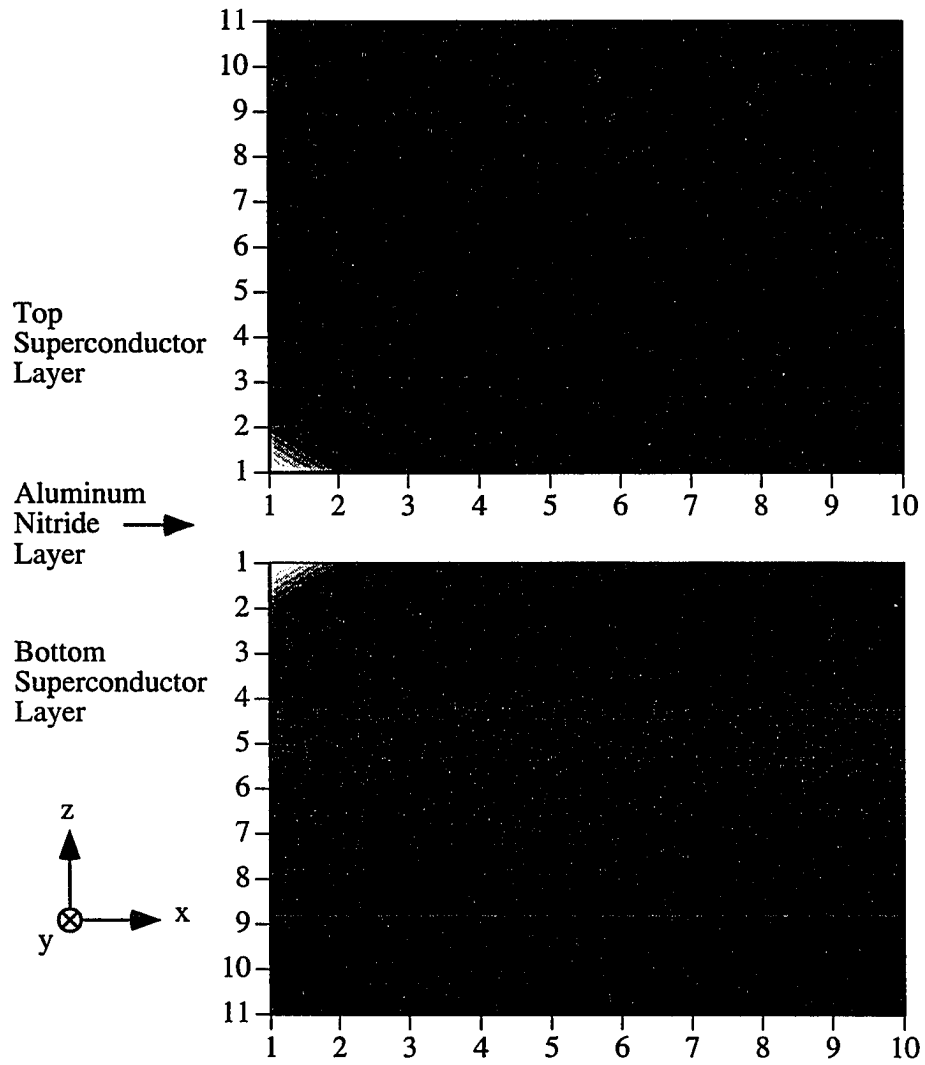


Figure 19: Potential of the superconducting sample

The next step in this dissertation will be to fabricate the aforementioned devices and compare the results with the theoretical results presented here. Some of the calculations will not be compared due to difficulties in measurement. The potential and current calculations will not be found in the samples, but a resonant frequency analysis and comparison with theory using the Mason model will be shown.

IV. EXPERIMENTAL METHOD

The method of this dissertation project will be described in detail below. The experimental procedure and choices for each procedure will be divided into five main sections. The first section will deal with the overall design and structure of the device. The next section will be the selection of SrTiO_3 for the substrate material. Third will be a discussion of Laser Ablation as it relates to its utilization in the deposition of the HTSC. The fourth section will discuss the use of Yttria stabilized Zirconia as the buffer layer for the growth of the top layer of HTSC. The final section will describe the procedure developed by the author for the testing of the HTSC bulk acoustic wave resonator devices.

IV.A. Experimental Design

The structure that is being presented is a bulk acoustic wave microstrip resonator. The resonator will have a substrate of MgO or SrTiO_3 to promote growth of the high temperature superconductor. The next layer in the structure will be a layer of superconductor with the thickness $\sim 2\mu\text{m}$. The limiting criterion for the thickness that is it must be thicker than the penetration depth, or 925\AA . [58] The piezoelectric or dielectric that will be used is Aluminum Nitride. The AlN that will be used is a polycrystalline c-axis aligned form of AlN with well-documented properties. The last layer will be an Aluminum top conductor to provide a top contact to the resonator.

There was one other similar structure fabricated along with this basic device to account for all the possible variables in processing and to compare the structure with predicted results and other materials. The structure fabricated was an Al - AlN - Al structure to establish a baseline reference.

Most of the materials processing for this project was performed at the Microelectronics Research Center. The exception to this is that the superconductor layers were applied by means of Laser Ablation processing performed at Oak Ridge National Laboratory by Dr. Doug Lowndes. The details of laser ablation can be found later in section IV.D. The Aluminum Nitride was deposited using DC Magnetron sputtering from an Aluminum target in a Nitrogen atmosphere. The process for depositing Aluminum Nitride can be found in Appendix C. Lastly, the ZrO_2 buffer layer, if used in any particular structure, is applied by a Sol-Gel technique. A detailed procedural description of this technique can be found later in the method section and previously in the materials section.

Following this page are designs for the structures that were fabricated. There were multiple iterations of structures to determine which would yield the best results in terms of reproducibility and signal strength. The method of measuring the structures at microwave frequencies dictated some of the layered structures due to the geometries necessary for measurements. The method of Dishal [54] was investigated, but was abandoned because of the small geometries used resulting in a very small signal strength. The design for a structure to be measured using the method of Dishal is shown in Figure 20. In Figure 21, there is an

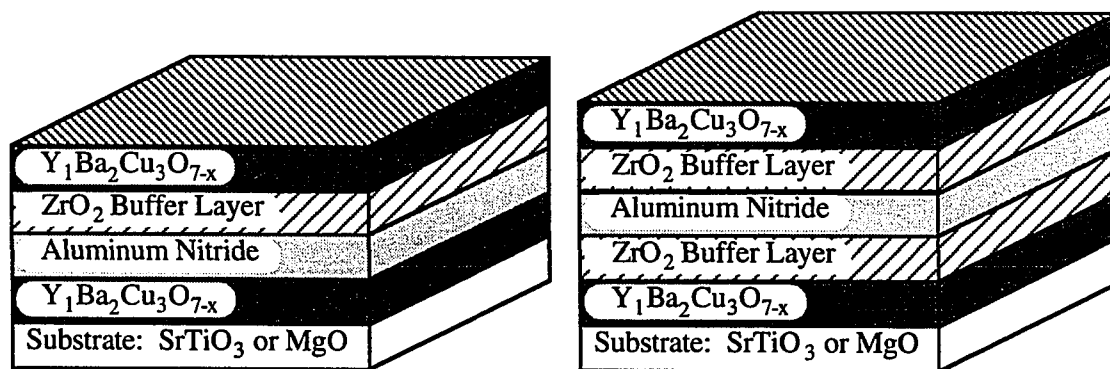


Figure 20: Samples designed for the Dishal method for measuring high frequency superconductive devices. The figure on the right has the additional ZrO_2 buffer layer added.

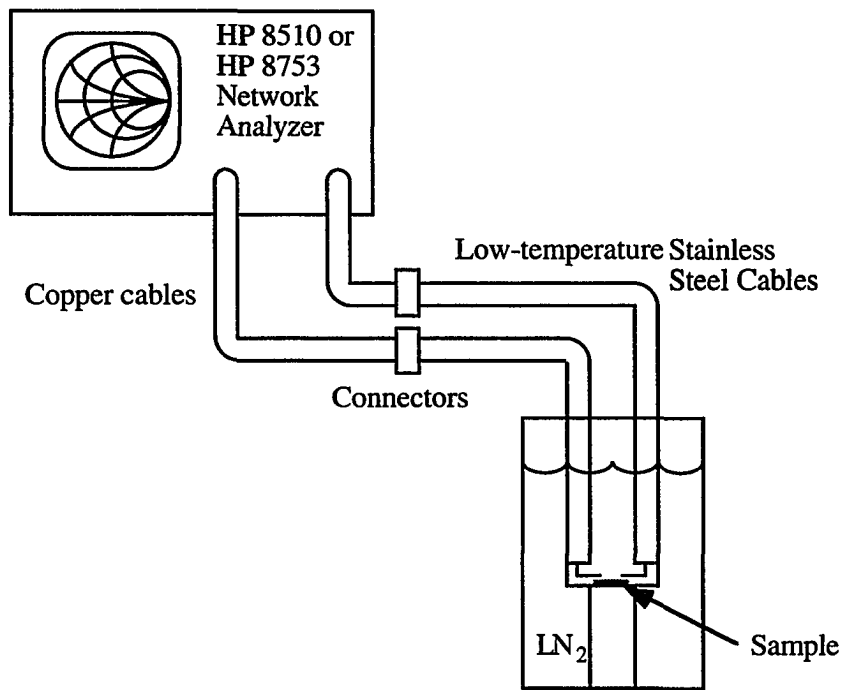


Figure 21: Sample measurement set-up using the Dishal method for resonant structures.

example of the setup that would have been used for this method. This method is a technique to stimulate the resonance in devices by coupling electrically or magnetically to the surface of the device in question. A measurement of S_{21} showing the resonant peak would have been the desired output from this method.

The Dishal method yielded unsatisfactory results due to the high transfer impedance of the sample being measured. The Al - AlN - Al sample had a simple 1 cm x 2 cm pattern etched into the surface to attempt Dishal's method, but even with this large contact size, there was no identifiable resonance. This is due to the thickness and the high dielectric constant of the AlN which results in the high transfer impedance. The method used for measuring the devices is a standard method for small microwave devices referred to as microstrip probing. The probe heads have a uniform spacing of 100 mils at the end of a coaxial high frequency feed line. The experimental structure then feeds into a probing pad with varying sizes available at the capacitive end. This change in size results in different efficiencies and signal strengths which have different effects on microwave circuits. For this project, the strongest signal strength is the desired output. A diagram of this structure can be found in Figure 22.

Shown in Figure 23 are the actual etched structures that were tested. The pattern in Figure 22 is used as a template to etch the top Aluminum conductor of the bulk acoustic wave device.

After the structures have been etched, they are then ready to be tested. The room temperature testing proceeded in a similar fashion to the cryogenic testing, with the exclusion of the liquid Nitrogen. The test set-up is shown in Figure 24, while a photograph of the measurement is shown in Figure 25. Some explanation is required at this point. The sample rests in a dewar with a stand to hold the sample off the bottom of the dewar. The dewar itself is a simple styrofoam "bowl". This setup is then cooled with liquid Nitrogen and then the sample is placed on the top of this holder. This technique was chosen for its simplicity and its capability of maintaining a constant temperature of 77°K.

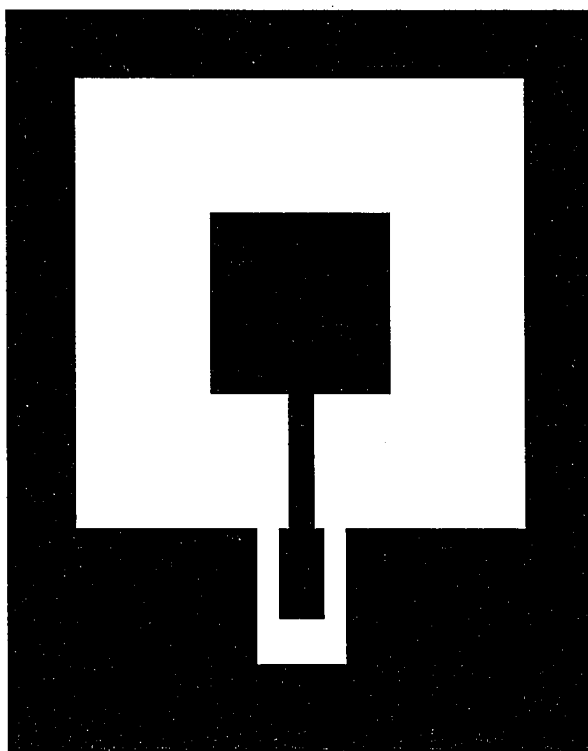


Figure 22: Resonator mask design. The probe will make the measurements at the lower part of the design where the "panhandle" extends out with room for two ground plane connections.

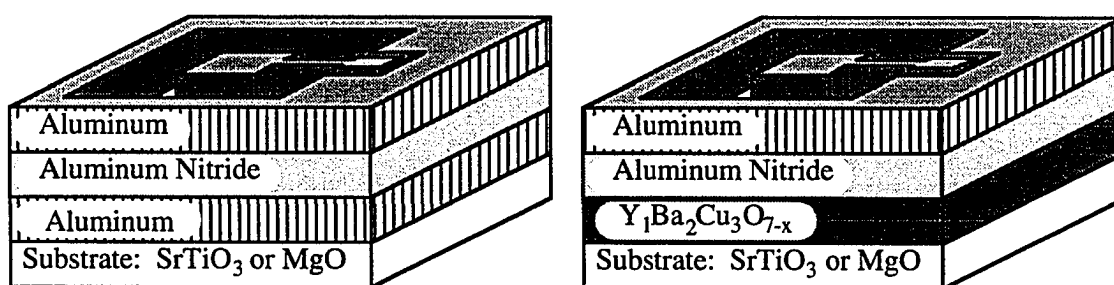


Figure 23: Actual structures for testing of HTSC BAW devices using the mask design presented in Figure 22.

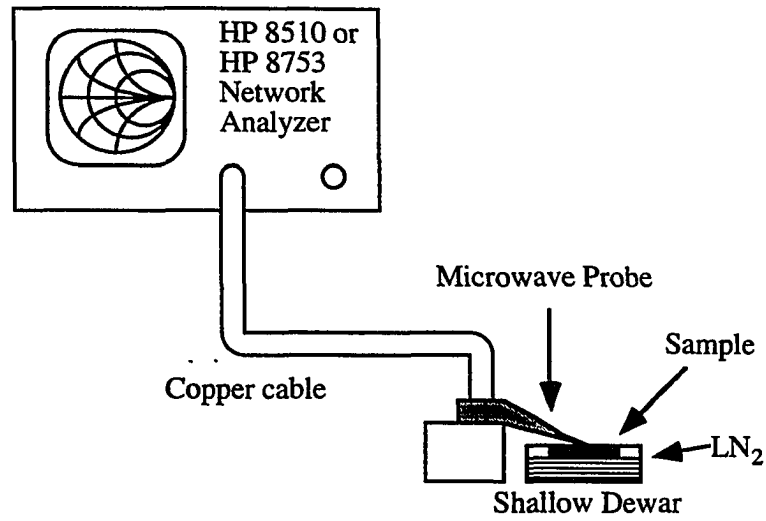


Figure 24: Cryogenic microwave probing of the bulk acoustic wave resonator structure.

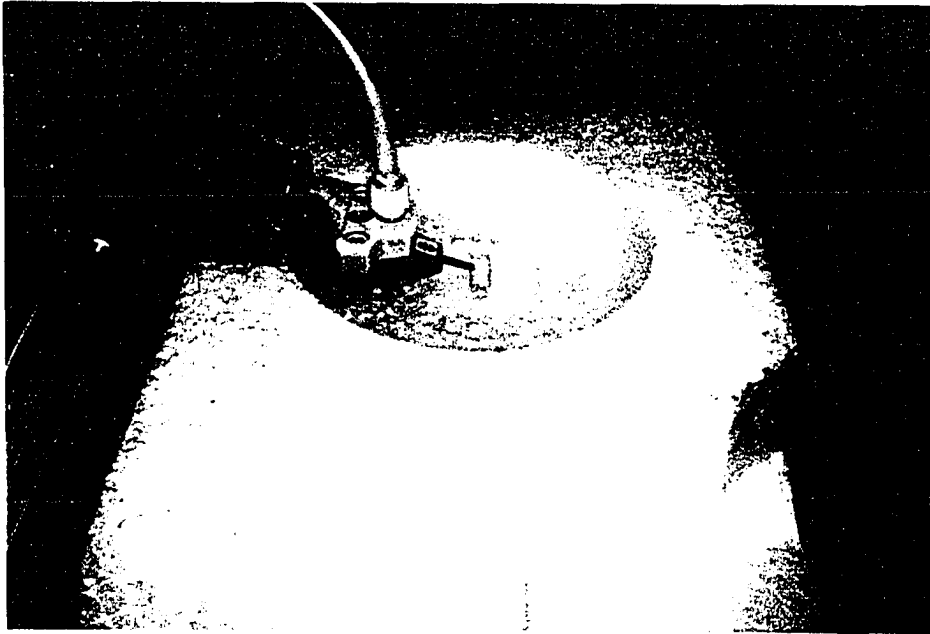


Figure 25: Photograph of the cryogenic microwave measurements taken on the bulk acoustic wave resonator structures.

The DC measurements were automated using a National Instruments device which allowed a Macintosh computer to communicate with three digital multimeters simultaneously. The schematic for this procedure is illustrated in Figure 26, and a photograph of the measurement being taken is shown in Figure 27. The basic program for the measurements can be found in Appendix E. The current across the sample was set at a desired value, and then the sample potential and current were measured, along with the temperature of the sample. The standard output from this test set-up was the resistance versus temperature plot. The temperature of the sample was measured by means of a thermocouple set at the bottom of the HTSC sample with a constant current passing through a temperature sensitive diode. Measuring the potential of this diode will yield a sample temperature after minor conversions. All HTSC samples were measured for DC resistance, and some of the Sol-Gel results are shown in the results section. This is one method of determining the quality of the HTSC samples.

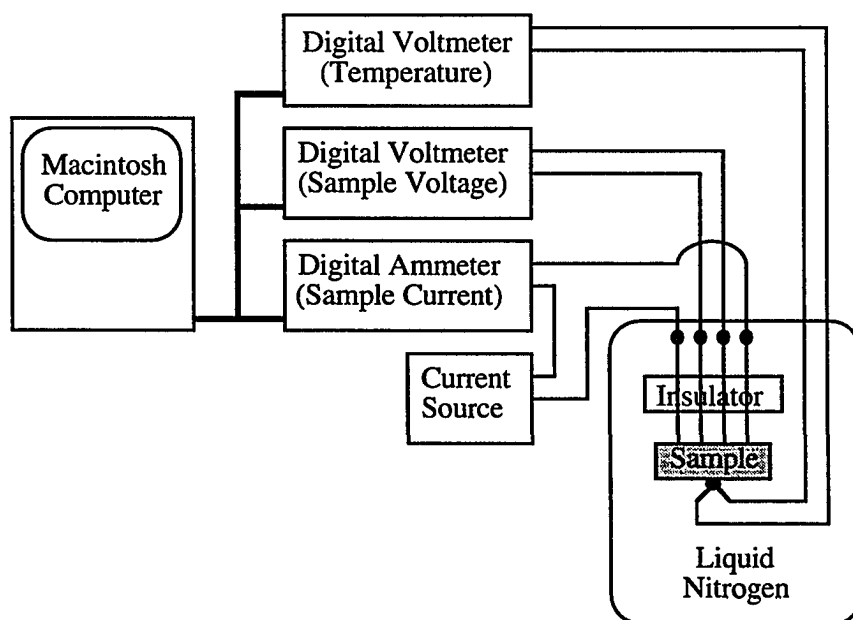


Figure 26: Four point probe cryogenic DC resistance measurement setup.

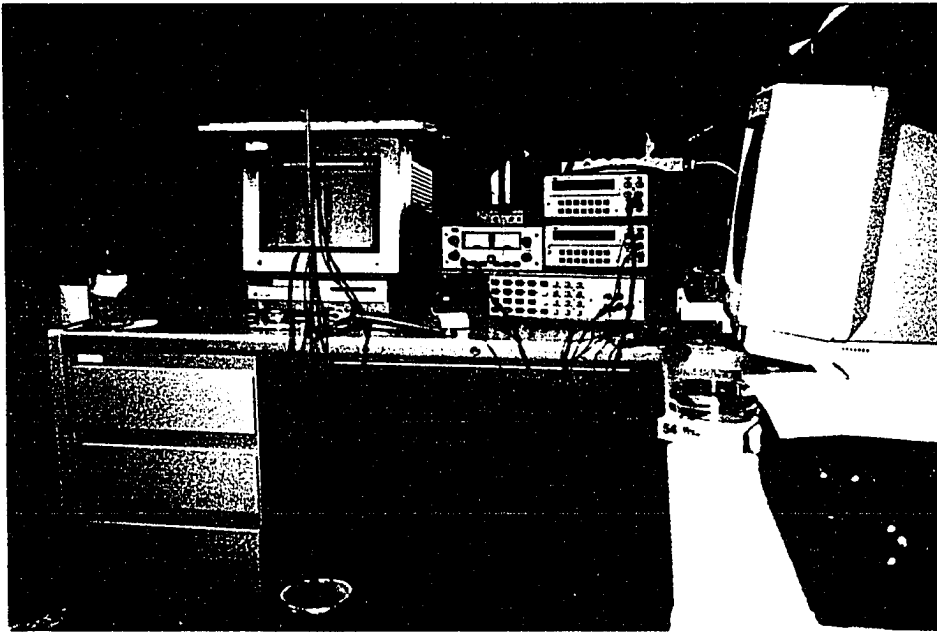


Figure 27: Photograph of the four point probe cryogenic DC resistance measurement setup

IV.B. Substrate Selection

The substrate chosen for most of the work in this project was SrTiO_3 . The reasons for this choice were two-fold: The characteristics of SrTiO_3 are superior for HTSC which will be discussed below, and the staff at Oak Ridge National Laboratories prefer to deposit their HTSC on SrTiO_3 for the best results. At Oak Ridge, they have experimented with MgO , Y-ZrO_2 , SrTiO_3 , and LaAlO_3 , to name some of the more popular substrates for $\text{YBa}_2\text{Cu}_3\text{O}_{7-x}$. They have found that for their system the best results, i.e., the highest transition temperature with epitaxially grown HTSC, have been from SrTiO_3 .

There are drawbacks to using SrTiO_3 for HTSC film growth. In passive stripline resonator structures, the loss tangent of SrTiO_3 is much too high for radio frequency applications [55]. Fortunately, this does not apply to the structure used for this dissertation due to the layered structure of the device. Shown below in Table 2 are dielectric properties for SrTiO_3 .

The benefits of SrTiO_3 greatly outweigh the drawbacks. With the perovskite structure similar to $\text{YBa}_2\text{Cu}_3\text{O}_{7-x}$, SrTiO_3 is arguably the best substrate for the growth of $\text{YBa}_2\text{Cu}_3\text{O}_{7-x}$. SrTiO_3 is the best substrate when compared to almost all substrates for the quality of the film growth [56]. This is illustrated in Table 3 which summarizes the characteristics of a variety of potential substrates.

Table 2: Dielectric Properties of SrTiO₃ for HTSC [55].

ϵ_r	$\tan \delta$	f (GHz)	Temp (°K)
~230	3×10^{-2}	9.5	300
215	1.4×10^{-1}	10 KHz	300
310	3×10^{-2}	10-1000	300
1900	6×10^{-2}	10-1000	80
T - Dependant	$1-2 \times 10^{-3}$	22	77-500
T - Dependant	$2-24 \times 10^{-3}$	22	37-600

Table 3: Properties and misfit relations of important substrates [57]

Substrate	a (Å)	Misfit YBCO (%)	α ($10^{-6}/^{\circ}\text{C}$)	ϵ	$\tan \delta \times 10^{-3}$
MgO	4.213	9	8	12	9.1
ZrO ₂ :Y	$3.63 \times \sqrt{2}$	~5	10.65	4-10	5.4
SrTiO ₃	3.905	~1	9.4	300	>2
LaAlO ₃	3.793	~2	11	15	0.6
LaGaO ₃	3.890	0.6	9	~26	2.5-6
NdGaO ₃	3.86	0.27	10	26	0.3 (77°K)
KTaO ₃	3.988	~3	6.8		
CaNdAlO ₄	3.69	4.4		~20	1.5
SrLaAlO ₄	3.77	2.5	7.4	~22	
SrLaGa ₃ O ₇	4.03×2	~4		13	6.5
Si	$3.84 \times \sqrt{2}$	0.7	4.4	12	<1
YBa ₂ Cu ₃ O _{7-x}	3.866	-	13		

IV.C. Buffer Layer Selection

There was no buffer layer used in these experimental structures. The buffer layer is required to provide a lattice match to the HTSC. This avenue was not pursued due to lack of results from the basic structures. The addition of a buffer layer requires additional processing steps, and material interfaces which can potentially degrade the performance of the HTSC device. If multiple layers of non-lattice matched materials are needed for a device, a buffer layer is required to obtain the smallest degree of misfit between the lattice constant of the substrate and the lattice constant of the HTSC. The microwave properties of this device, Q and efficiency, will decrease due to the addition of these layers, but this is a trade-off for the use of the superconductors.

The following technical requirements must be fulfilled for a given substrate or buffer layer [59]: A lattice match, a high degree of flatness, crystallographic perfection, physical properties (such as thermal conductivity and thermal expansion) matching, and chemical inertness. SrTiO_3 and YSZ satisfy these requirements. Most of the data for these two substrates can be found in Table 3.

YSZ is a popular choice for use as a buffer layer for the YBCO HTSCs. The results from the deposition of YSZ followed by subsequent HTSC deposition are excellent: Transition Temperatures are $T_c = 89^\circ\text{K}$ for YSZ on Si [60], $T_c = 87^\circ\text{K}$, $J_c > 10^4 \text{ A/cm}^2$ @ 77°K for YSZ on a metallic alloy [6], and $T_c = 88^\circ\text{K}$ for YSZ on YSZ [61].

IV.D. Laser Ablation

Laser Ablation was used for the deposition of $\text{YBa}_2\text{Cu}_3\text{O}_{7-x}$ film at Oak Ridge National Labs for the experimental devices. This procedure will be discussed in detail below. This is one of the most popular techniques for the production of HTSC films today due to its reproducibility and superior film characteristics.

This summary follows the description given in the text by Bourdillon and Bourdillon [58]. The procedure for laser ablation begins with a pulsed excimer laser which is focused at a target of HTSC in an air-tight chamber. The power of the laser (typically 300 mJ/cm^2 at Oak Ridge) ablates the material off the target and toward the heated substrate (typically 800°C at Oak Ridge). The atmosphere of the chamber is usually oxygen or Nitrous Oxide to promote oxygenation of the HTSC. The ablated material proceeds toward the substrate and is deposited onto the substrate with rates up to 10 nm/s . A rotating target aids in the uniformity of the film grown and also assists in maintaining the uniformity of the material ablated off the target. A sample set-up for this process is shown in Figure 28.

Laser ablation has the lowest processing temperature for any of the known procedures for fabricating the HTSC described in the material section [56,57]. This is beneficial if any further processing is to be done on the material. In the case of this dissertation, this low temperature processing is especially beneficial because of the AlN processing step. The Aluminum Nitride in the presence of oxygen or oxygen compounds will decompose into Al_2O_3 , therefore maintaining a low temperature is crucial. Also, having lower temperatures will decrease the potential for atoms and molecules to migrate between the processed layers. For all of the aforementioned reasons, laser ablation is the process of choice.

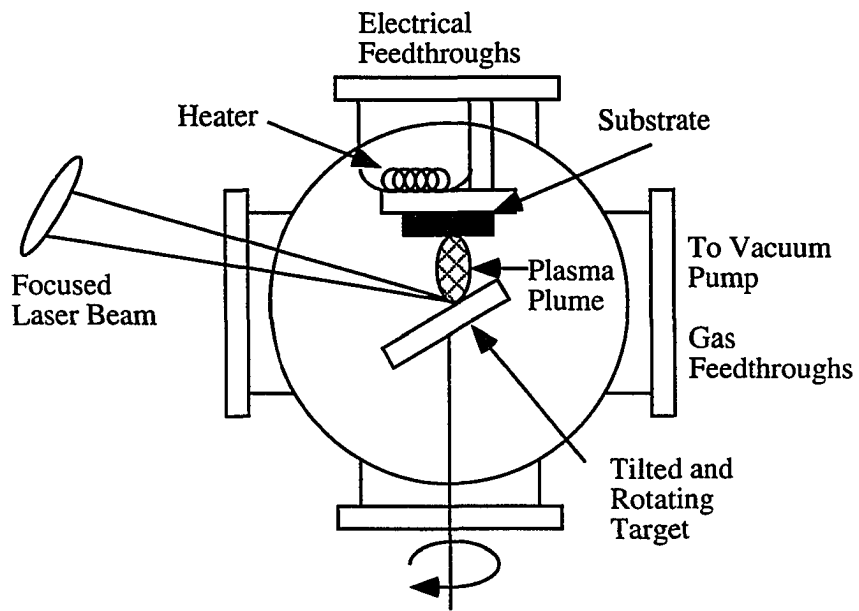


Figure 28: Sample Laser Ablation Schematic Diagram.

V. RESULTS

Results have been obtained for the initial samples of the Sol-Gel superconductors from July of 1993. The data is shown in Figure 29. This was the first sample that was made, and is not of high quality due to the fact that the sample was not protected against water vapor. Another drawback to this sample is the fact that the thickness is inadequate to show distinct superconducting properties. There were "islands" of superconductor on the sample which suggest that the sample was not thick enough for adequate conduction. There were numerous other samples with somewhat promising results ($T_c \sim 82^\circ\text{K}$), and the results of these samples are shown in Figures 30 and 31. The sol-gel procedure was not pursued further due to the non-conformal nature of the superconducting layer. This resulted in the decision to utilize the facilities at Oak Ridge to perform the deposition of the HTSC.

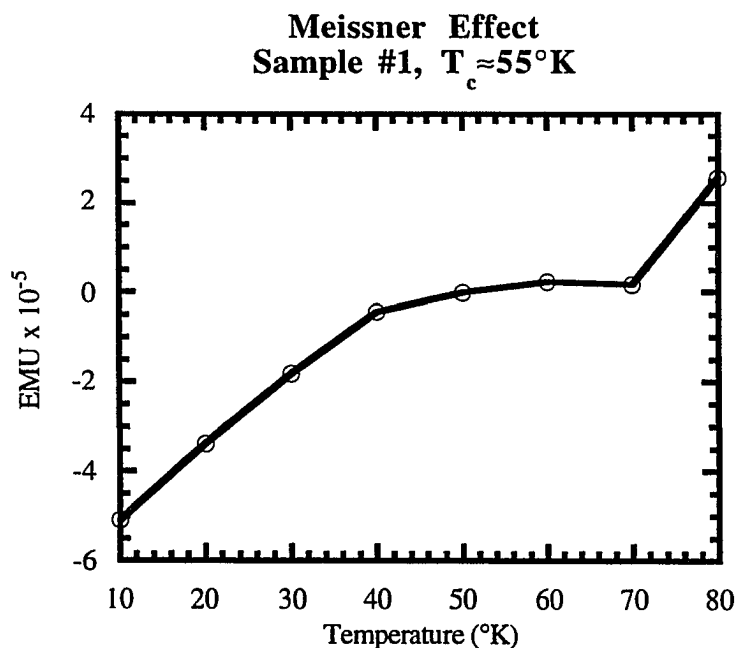


Figure 29: Magnetic susceptibility of sol-gel HTSC sample

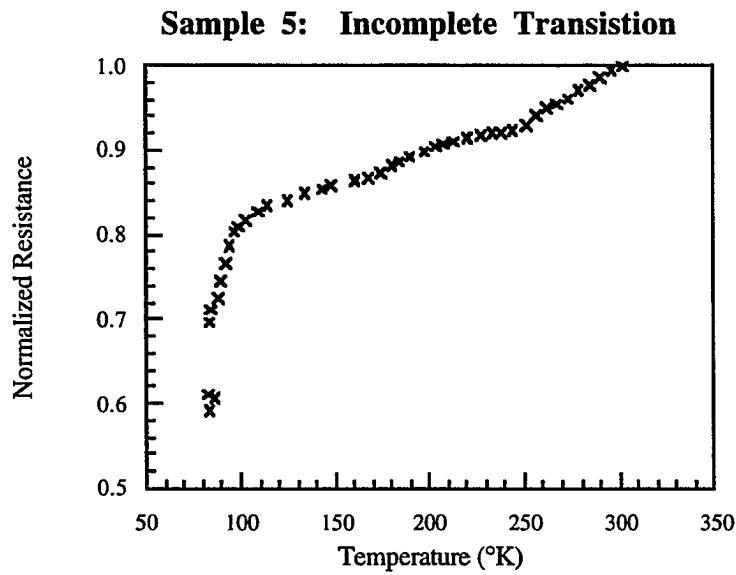


Figure 30: Incomplete sol-gel resistance versus temperature transition.

The sample did not reach $R=0\Omega$.

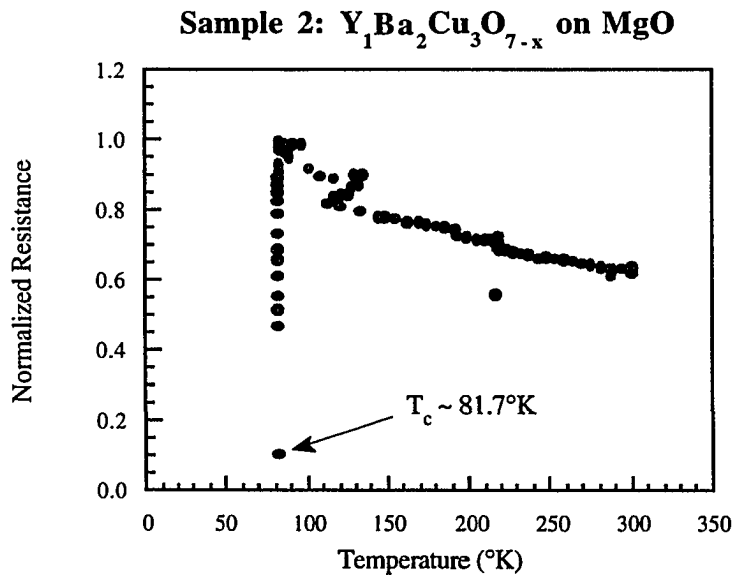


Figure 31: Resistance versus temperature for a sol-gel superconducting HTSC sample. The discontinuities in the graph are errors in the measurement technique by the author.

There are a few pieces of experimental data that should be taken for proper characterization of the HTSCs. The superconducting transition, or T_c , should be measured before any microwave measurements are made. This may be accomplished in two different forms, a DC measurement of the transition temperature, and the Meissner effect measurement to confirm the DC measurement.

The samples obtained from Oak Ridge National Laboratory were measured for superconductivity using the four point probe measurement. The details of this measurement are given in the experimental method section. The result of this measurement is shown in Figure 32. This result confirms the decision to pursue an alternate supplier of HTSC, since the transition of the samples are sharp and of high quality.

The microwave measurements were performed using a Hewlett Packard 8753 Network Analyzer. There were two samples that were measured at high frequencies as

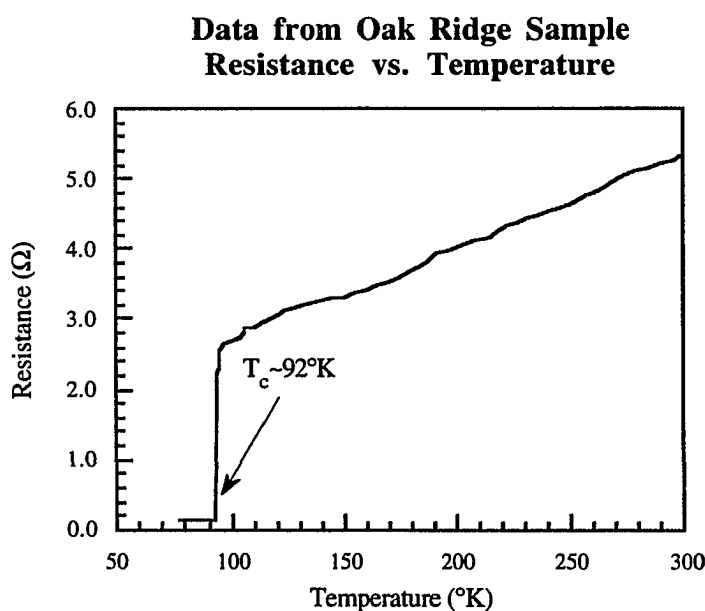


Figure 32: Resistance versus temperature for the superconducting HTSC sample grown at Oak Ridge National Labs.

described in the experimental methods section: Al/AlN/Al and HTSC/AlN/Al samples. The samples were both measured at room temperature ($\sim 293^{\circ}\text{K}$) and liquid nitrogen temperature (77°K). The measurements were S_{11} measurements (one-port scattering parameter data), and were converted into other forms by the network analyzer such as admittance parameters. The data is presented on a Smith chart, a log magnitude plot, and an imaginary part of the admittance format.

The Smith chart format gives a good matching and Q approximation, and displays the data in a convenient graphical format. The log magnitude gives relative intensity of the device under test's signal reflected back to the network analyzer. A useful estimated calculation of Q can be obtained from the log magnitude plot by taking the frequency of the 3 dB point on either side of the resonance as a Δf . Q is then estimated as $f/\Delta f$ where f is the center frequency in question. This is only an estimate because the Q calculation from scattering parameters does not give the exact Q value. An exact value of Q can be calculated by using the frequencies for which $|X|=R$ or $G=|B|$. The values for which $G=|B|$ can be found by setting the network analyzer to measure the imaginary part of the admittance plot. From the frequency change between the peak value to the lowest value of the imaginary portion of the admittance, an accurate value of Δf may be achieved. The $f/\Delta f$ calculation from the imaginary admittance is the definition of Q and is the basis for all quoted Q values in this dissertation unless otherwise noted.

The admittance plot also yields an interesting piece of data. By measuring the Δf between the peaks in the admittance plot, and knowing about some of the material properties of the substrate material, the thickness of the substrate may be ascertained. The logic behind this measurement is that when an acoustic wave is launched into the substrate, it will reach the bottom of the wafer and then be reflected back to the probe. A sample calculation of this technique is given in equation 41 for the Al/AlN/Al sample at room temperature.

$$t = \frac{\sqrt{\frac{c}{\rho}}}{2f} = \frac{\sqrt{\frac{166 \times 10^9 \frac{\text{m}^2}{\text{N}}}{2330 \frac{\text{kg}}{\text{m}^3}}}}{2 \cdot 10.649 \times 10^6 \frac{1}{\text{s}}} = 396 \mu\text{m} \quad (41)$$

All of the high frequency testing had constant measurement parameters. The structure tested in all cases is a $1600 \mu\text{m}^2$ square patch ($400 \mu\text{m}$ per side) bulk acoustic wave resonator with the following approximate dimensions: $420 \mu\text{m}$ Silicon substrate, 1000 \AA Aluminum ground plane, $3.5 \mu\text{m}$ Aluminum Nitride, 100 \AA Chromium (to prevent Aluminum spiking into the AlN), and 1000 \AA of Aluminum as the top metal contact.

The first high frequency results to be presented are the Al/AlN/Al plots at room temperature which are given in Figures 33, 34, and 35. Figure 33 is the Smith chart representation, Figure 34 gives the log magnitude plot, and Figure 35 is the imaginary admittance plot for the same data. This is a typical overmoded response from a bulk acoustic wave resonator. The calculation of Q with data taken from Figure 35 is shown below. Note that this Q value contains the Q of the wafer also.

$$Q = \frac{f}{\Delta f} = \frac{926.244 \text{ MHz}}{926.636 \text{ MHz} - 925.8515 \text{ MHz}} = 1181 = Q \text{ of the BAW resonator at } 293^\circ\text{K} \quad (42)$$

The next high frequency results to be presented are the Al/AlN/Al plots at liquid Nitrogen temperature which are given in Figures 36, 37, and 38. Figure 36 is the Smith chart plot, Figure 37 gives the log magnitude representation, and Figure 38 is the imaginary admittance plot for the same data. This is a typical overmoded response from a bulk acoustic wave resonator, but due to the cryogenic measurement parameters, the results are significant. The calculation of Q with data taken from Figure 38 is shown below. Note that this Q value contains the Q of the wafer also.

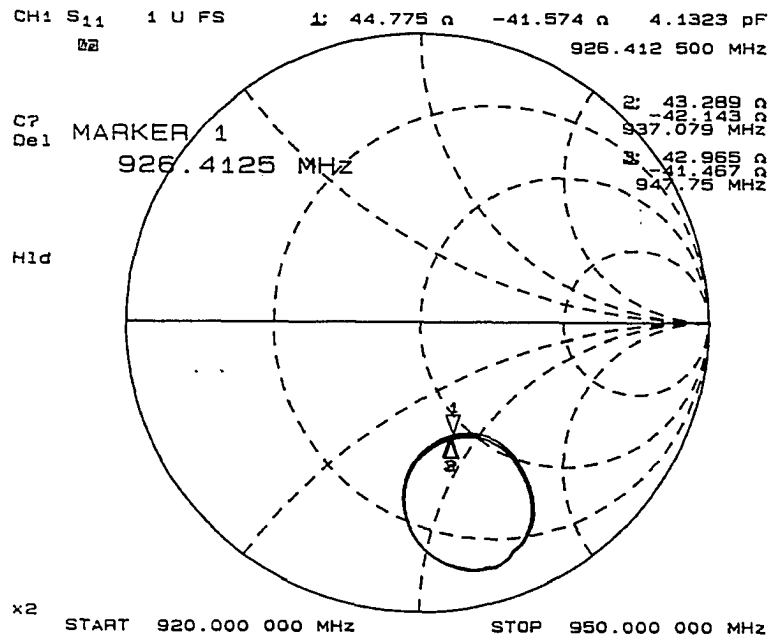


Figure 33: Smith chart display of AI/AIN/AI bulk acoustic wave resonator at 293°K.

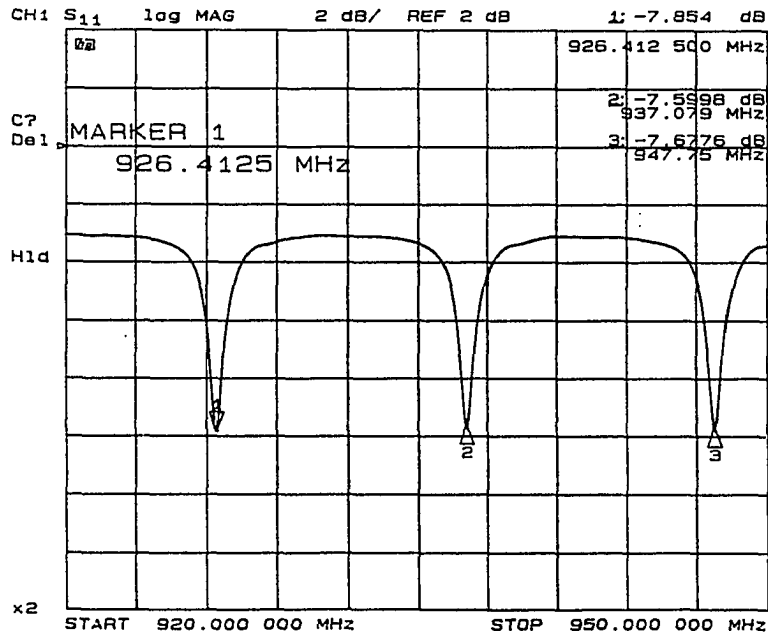


Figure 34: Log magnitude display of AI/AIN/AI bulk acoustic wave resonator at 293°K.

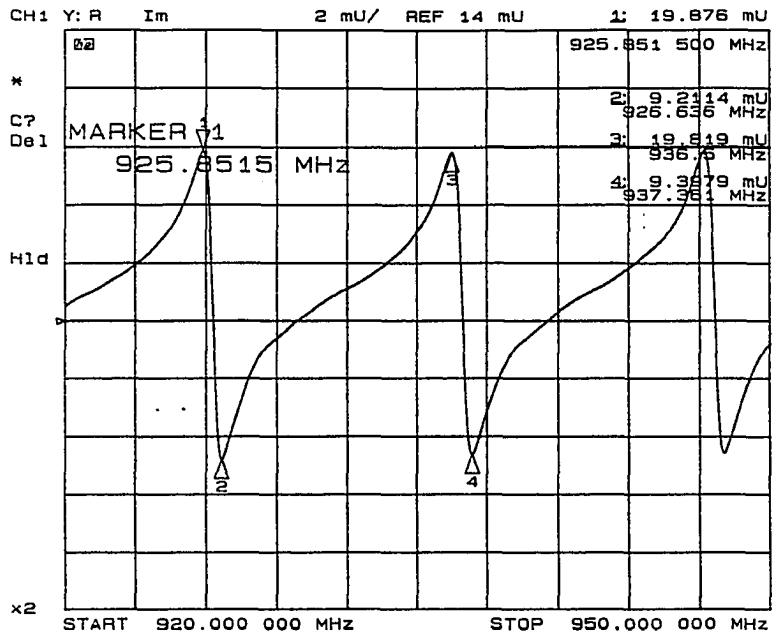


Figure 35: Imaginary admittance display of Al/AlN/Al bulk acoustic wave resonator at 293°K.

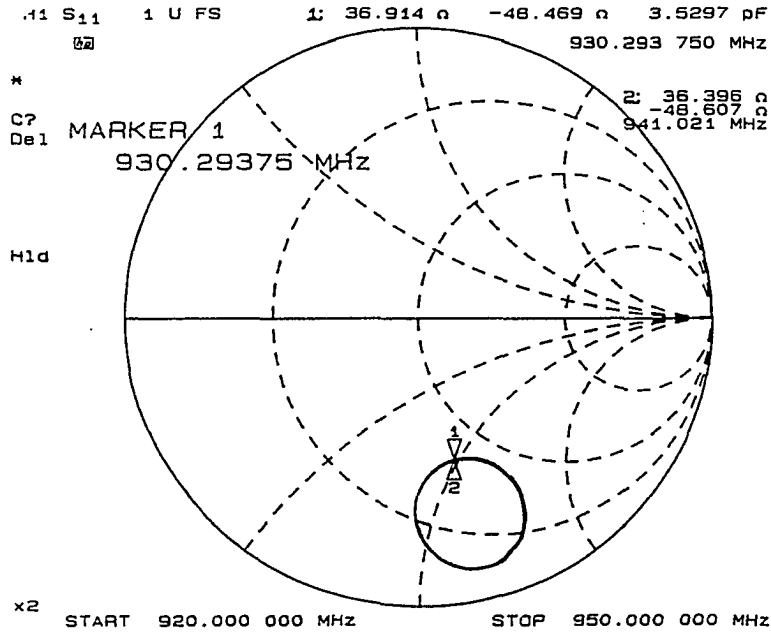


Figure 36: Smith chart display of Al/AlN/Al bulk acoustic wave resonator at 77°K.

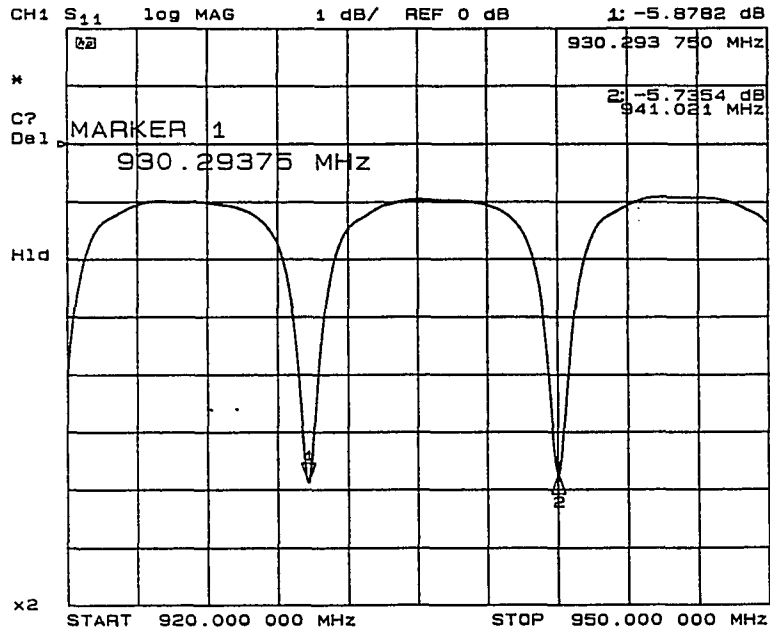


Figure 37: Log magnitude display of Al/AlN/Al bulk acoustic wave resonator at 77°K.

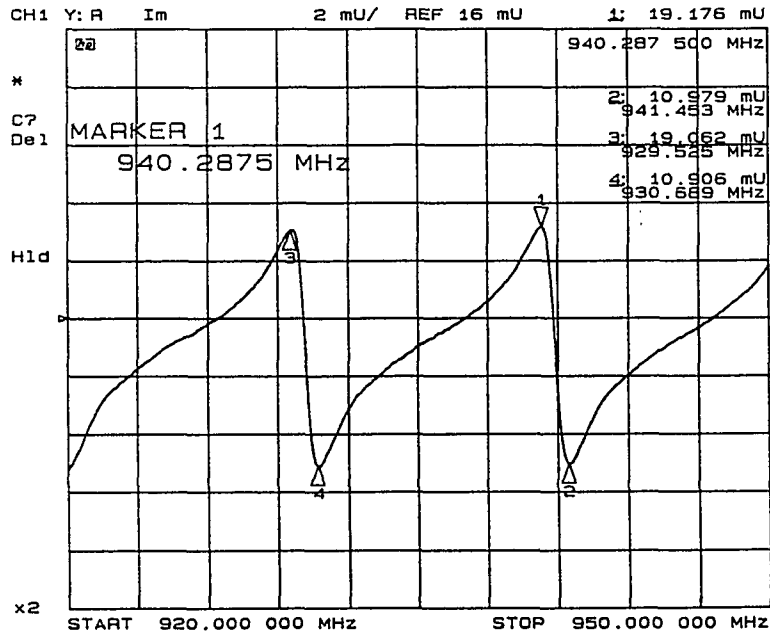


Figure 38: Imaginary admittance display of Al/AlN/Al bulk acoustic wave resonator at 77°K.

$$Q = \frac{f}{\Delta f} = \frac{930.107\text{MHz}}{930.689\text{MHz} - 929.525\text{MHz}} = 799 = Q \text{ of the BAW resonator at } 77^\circ\text{K} \quad (43)$$

The next results shown are for the HTSC/AlN/Al sample. Figure 39 and 40 show the response of the device at room temperature. Figure 39 is the Smith representation of the data, and Figure 40 is the log magnitude output. There was no imaginary admittance plot shown because there was no visible resonance. This result is consistent with a bulk acoustic wave resonator with a lossy metal ground plane. Marker number one on these two plots is located at the resonance point of the AlN (1.068 GHz) which will be illustrated presently.

In Figure 41, a log magnitude plot is shown where the microwave probe is resting directly on the AlN, thus bypassing the top Aluminum contact. The resonance at this point is 1.068 GHz, which is very close to the predicted resonance point of 1 GHz for 3.954 μm of Aluminum Nitride. The fact that this resonance is observed is significant because it confirms that the AlN is high quality and piezoelectrically active.

At liquid nitrogen temperature, this resonance is still visible as shown in Figures 42 and 43, where Figure 42 is the Smith chart representation, and Figure 43 is the log magnitude plot for the data. The frequency has shifted marginally, but with the liquid nitrogen loading of the Aluminum Nitride, this result is consistent with predictions. Note that this measurement actually gives the resonance from the microprobes directly in contact with the Aluminum Nitride, thus measuring the HTSC ground plane and the Aluminum Nitride. The HTSC measurement on the Aluminum pads did not yield any significant results. There are a number of reasons for this result, and those reasons will be discussed presently.

There are a number of possibilities for the results of this cryogenic measurement. It is possible that the explanation could be a combination of effects listed below, or one reason alone could explain the results. Additional testing is required to determine the overall cause or explanation for these results.

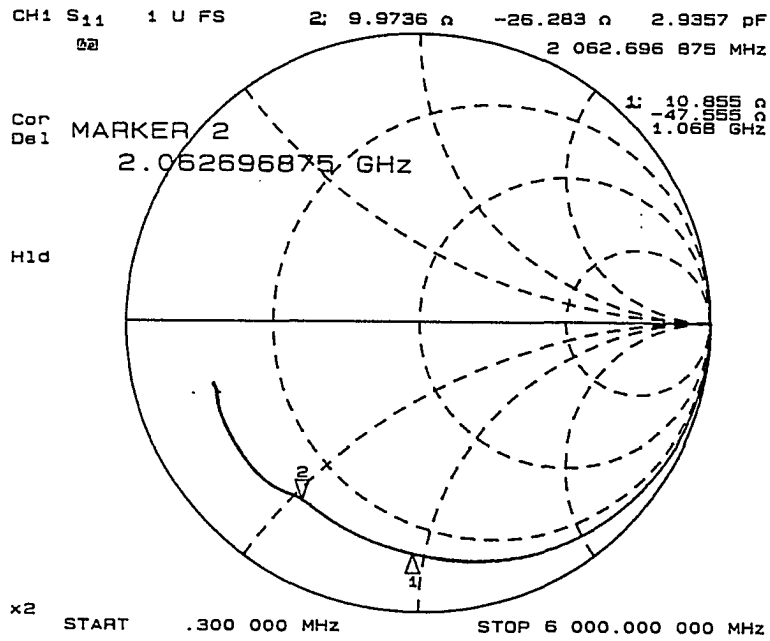


Figure 39: Smith display of HTSC/AIN/Al bulk acoustic wave resonator at 293°K.

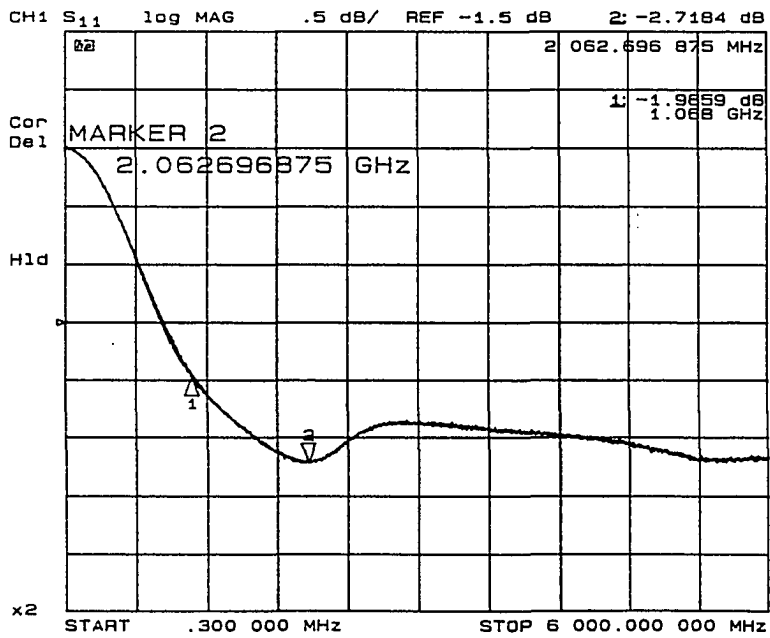


Figure 40: Log magnitude display of HTSC/AIN/Al bulk acoustic wave resonator at 293°K.

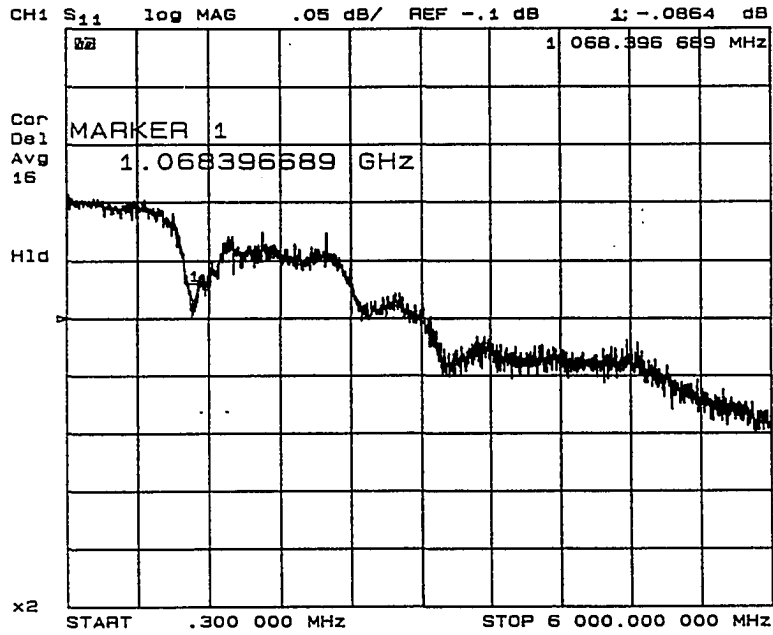


Figure 41: Log magnitude plot of microwave probes directly on the Aluminum Nitride

portion of the HTSC/AlN/Al sample at 293°K.

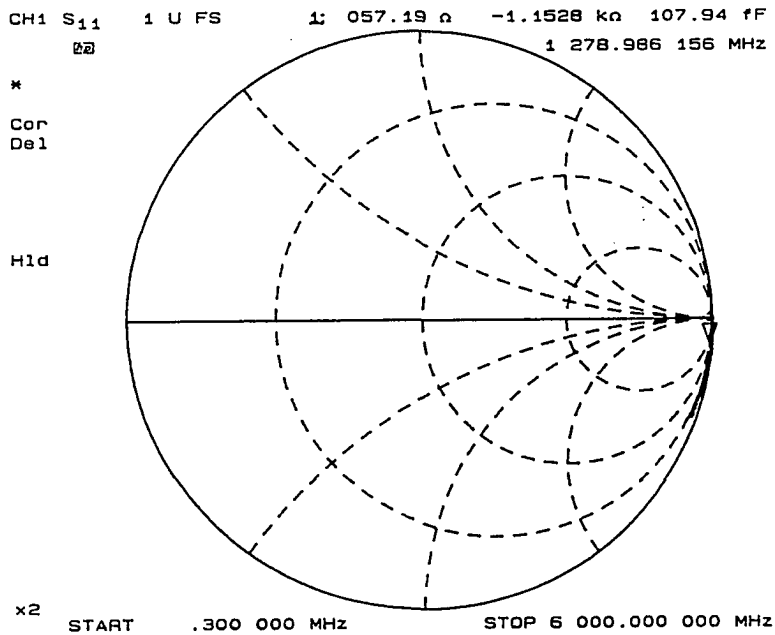


Figure 42: Smith chart display of microwave probes directly on the Aluminum Nitride

portion of the HTSC/AlN/Al sample at 77°K.

The first possible explanation is inherent in the measurement technique. The technique of using a “panhandle” resonator structure as shown in Figure 22 is dependent on capacitively coupling to the ground plane. If the ground plane is not a good conductor, or is a lossy conductor, then this could potentially be a source of uncertainty.

Another assumption is that the HTSC will behave similar to a metal at cryogenic temperatures in a bulk acoustic wave resonator. Theoretically, the HTSC will repulse all static electric fields from the surface of the superconductor, but the investigation of microwave or acoustic waves has yet to be determined. A possibility of acoustic attenuation combined with high frequency losses may have had a dramatic effect on the sample. This conclusion is logical, due to the auxiliary measurements performed on a superconductor-only sample from Oak Ridge National Labs. Placing the microwave probes on this sample yielded a capacitive lossy structure at cryogenic temperatures. The high frequency measurements yielded data that was sensitive to the amount of pressure applied to the high frequency probe. This is consistent with the explanation that as the pressure is increased to the probe, the probe is making contact with more HTSC crystals. Another possible explanation for this result is that the BeCu microwave probes could have a work function potential problem when measuring the HTSC. The quality of the HTSC is not an issue as subsequent DC measurements confirmed the quality of this sample shown in Figure 32. The contact issues of the HTSCs will be discussed shortly.

There were concerns with the ohmic contacts to the HTSC itself. Measurements were performed with the microwave probes onto a sample of HTSC that had no subsequent depositions performed. The impedance of the HTSC at higher frequencies below liquid nitrogen temperature decreased as the pressure on the probes was increased. One interpretation is that when the probes come into contact with more crystals of the superconductor, the impedance decreases. Another possibility is that the workfunctions of the BeCu probes and the HTSC may have been quite different, thus resulting in a non-

metallic contact. This result would dictate the use of a contact metal for the proposed HTSC - AlN - HTSC structure as the surface impedance of the structure would vary with the pressure applied to the microwave probes. The contact metal would then provide a more uniform contact to the HTSC. Further research and experimentation into HTSC contacts and microwave probes would be necessary for this structure.

If the HTSC were too thin, then the resistive and the acoustic losses of the bottom conductor would be amplified. This thinning effect could also be due to the subsequent processing steps such as the Aluminum Nitride deposition. Contamination by H_2O would adversely affect the HTSC and could potentially explain the lack of performance of the HTSC bulk acoustic wave device, but this could not explain the lack of results in the bare HTSC microwave measurement.

A couple of observations show that this technique for measuring the microwave characteristics of the HTSC structure was fairly accurate, but not optimal. The majority of measurements for HTSC microwave devices do not involve the submersion of the sample into the liquid Nitrogen, instead a typical setup is shown in Figure 44. The sample is placed in a vacuum to prevent H_2O vapor from condensing on the sample, while liquid Nitrogen flows below the sample, thus maintaining a constant temperature of $77^{\circ}K$. In the technique described in Figure 24, there are a number of non-optimal measurement conditions. One result is the liquid Nitrogen loading of the bulk acoustic resonators. This is shown in the Al/AlN/Al resonator structure Q calculations in Equations 42 and 43. Another condition stems from the possibility that water condensation caused the probes to “ice up” during measurements. Since ice is a fairly proficient insulator, the probes were warmed up and dried to insure valid measurements.

These are some possible explanations to explain these microwave results for the bulk acoustic wave resonators. There are many experiments that could potentially be performed to eliminate some of these variables, but they will not be presented here.

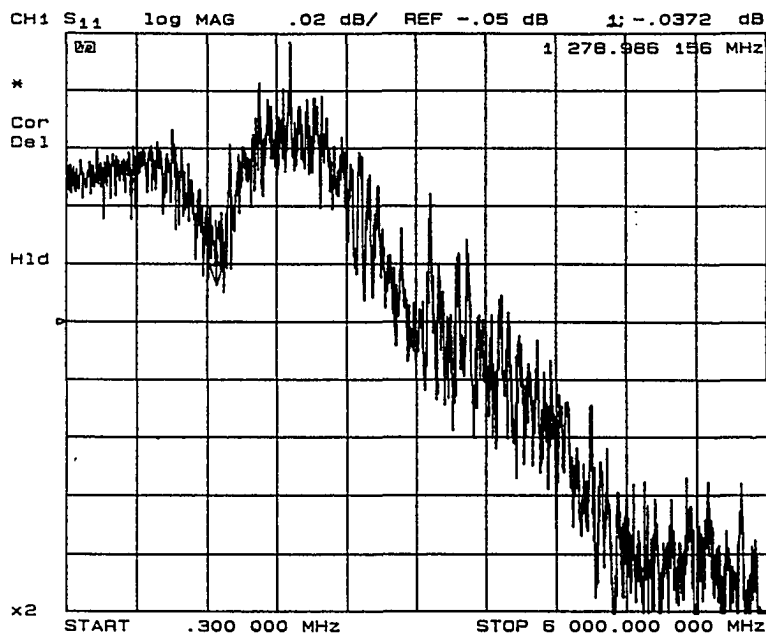


Figure 43: Log magnitude plot of microwave probes directly on the Aluminum Nitride portion of the HTSC/AlN/Al sample at 77°K.

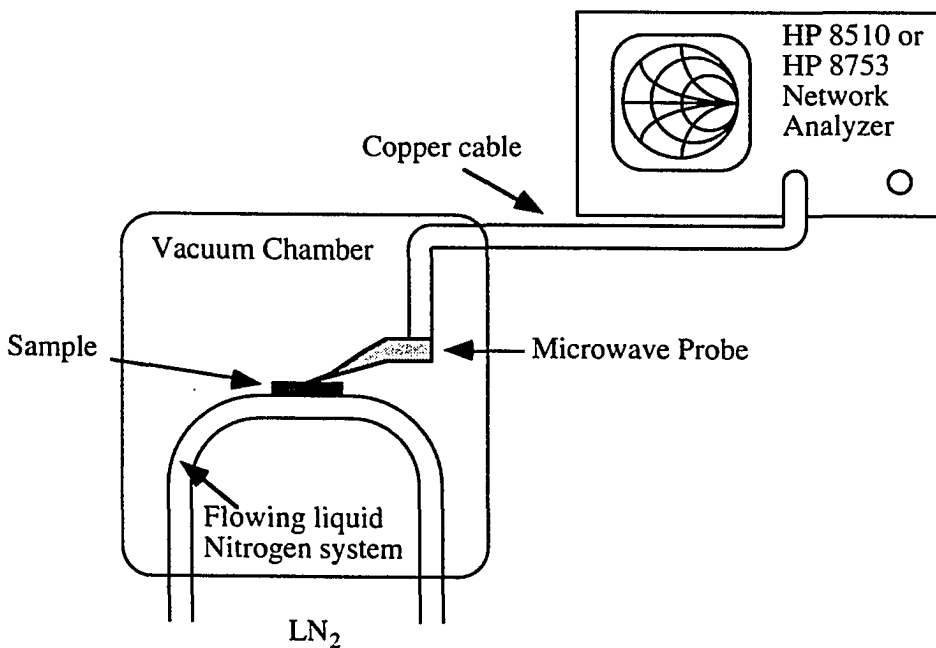


Figure 44: Optimal microwave measurement setup

VI. CONCLUSIONS

This dissertation has presented a superconducting microwave resonator structure design, analysis, and experimental method. Theoretical and experimental conclusions may be made concerning the results obtained. The conclusions are broken into two sections. Both sections will then be compared and a final conclusion will be given.

The theoretical conclusions of this dissertation cover the analysis of the HTSC structure. From the theoretical analysis, it is evident that this HTSC - AlN - HTSC structure may be modeled using a transmission line structure. This transmission line structure accounts for the HTSC and the non-superconducting component of the HTSC with the two-fluid model. The piezoelectric AlN may be modeled using the Mason model and utilizing the acoustical parameters for the HTSC given in the literature and documented in the experimental analysis section. These theoretical results closely resemble the nature and behavior of the HTSC for current flow and the electric potential of the HTSC layers. The piezoelectric effects also are similar to the standard Al - AlN - Al resonating structures. This device has been successfully simulated and modeled using this transmission line - Mason model approach.

The experimental conclusions of this dissertation are numerous and noteworthy. The first conclusion is that Al/AlN/Al bulk acoustic wave resonators are stable from room temperature to 77°K, and that the acoustic properties of the AlN are stable throughout this temperature range. The second conclusion drawn from these experiments is that the Al - AlN - HTSC structure is realizable and feasible. Further research must be performed on this structure to effectively evaluate the performance as a feasible device.

In comparing the theoretical results with the experimental results, a few general conclusions may be drawn. The theoretical results do not account for the unknown qualities

of the HTSC such as acoustic interfaces. Modeled as a conductive metal, the HTSC theoretically performs well, but experimentally there are drawbacks. Once these obstacles are resolved, this device may be realized. Because the superconductor alone is not a perfect short circuit at 77°K, it has been determined that more work must be done in the materials development to engineer an epitaxial HTSC bulk acoustic wave resonator stack. There currently exists no measure of the bulk acoustic properties of HTSC, and this measurement is worthy of publication.

VI.A. Significant Contributions

There are five directly foreseeable contributions by the author of this dissertation to the state of the art in microwave superconducting devices and circuits. These contributions are advances in materials, theory, and analysis. All of these contributions are detailed below and are documented throughout this dissertation.

The first contribution is that of the layered structure itself. This configuration of Aluminum Nitride and HTSC has not previously been attempted. This is the first attempted epitaxial bulk acoustic wave resonating structure using HTSCs. The addition of ZrO_2 to the layered structure is another original design, with the AlN/ZrO_2 interface being a novel design. Similarly, this is the first device of this nature utilizing this AlN/ZrO_2 interface.

The testing procedure development for these devices was considerable: Software and hardware interface protocols were developed to automate this analysis, yielding a more efficient measurement technique. The cryogenic testing was a logistical problem to overcome, with the structure being tested at both room temperature and liquid nitrogen temperatures. Both DC and RF measurements were taken on all the samples to ascertain the DC characteristics as well as the microwave characteristics of the HTSC.

Included in this analysis is the comparison of room temperature versus liquid nitrogen temperature performance of the microwave resonators. Both structures, Al - AlN - Al and HTSC - AlN - Al were analyzed by collecting measurements of efficiency and Q value at both room temperature and liquid nitrogen temperatures. This data is significant in predicting the material characteristics of the HTSC and is a significant contribution to this dissertation.

The theoretical analysis of the superconductor in conjunction with an Aluminum Nitride bulk acoustic wave resonator is a contribution that has been presented at the Fall Materials Research Society conference [64]. Additional publishable work could result from probing further the microwave and acoustic properties of these HTSC bulk acoustic wave structures. This work would encompass many of the other contributions and would serve as an excellent overview of the project. Another possible publishable result would be to perform material analysis on the interface between the AlN and the HTSC, along with an analysis of the HTSC's acoustic properties.

VI.B. Future Work

There are other possibilities to expand upon the research presented in this dissertation. The first area of possible expansion is that of researching other more complicated structures that may be attempted with similar or entirely different materials such as a HTSC/AlN/HTSC structure. The high temperature superconductor itself may be changed to some of the newer, higher transition temperature superconductors such as the Thallium compound, or other compounds.

Another possible study would be to replace the piezoelectric AlN with other dielectrics or other piezoelectrics to determine the effects of cryogenic operation on these compounds and these devices. The last area of materials research which could be a possible

topic for research would be to use a buffer layer that may be an exotic metal which is lattice matched to the superconductors instead of using the dielectric ZrO_2 .

A further theoretical study expanding on the joint transmission line analysis and the Mason model should yield some interesting results. A comparison between procedures for calculating resonant structures, along with a theoretical tolerance analysis on various processing variables would be a useful future project. Additional simulations on the microwave properties of superconductors are needed to further understand and utilize the acoustic properties of HTSCs.

Future work could also be devoted to studying different HTSC microwave devices in conjunction with the bulk acoustic wave resonator. There are a variety of devices such as microwave antennas, oscillators, filters that could be designed and fabricated from the HTSC materials. These devices could be built in conjunction with the bulk acoustic wave resonator presented in this dissertation to create an entire superconducting microwave circuit, or they could be investigated as a separate research project.

BIBLIOGRAPHY

- [1] Bednorz, J.G., and Muller, K.A. "Possible high T_c superconductivity in the Ba-La-Cu-O system." Zeitschrift fur Physik 64, (1986): 189-193.
- [2] Young, K. H., Robinson, McD., Negrete, G. V., Yamashita, T., Hirai, T., Suzuki, H., Kurosawa, H., Drabek, L., and Gruner, G. "Microstructure and microwave properties of YBCO thin films grown on MgO and SrTiO₃ by CVD." Journal of Materials Research 6, No. 11 (November 1991): 2259-2263.
- [3] Kovacheva, D., Petrov, K., and Peshev, P. "Investigation on the Interaction of Powdered YBa₂Cu₃O_{7-x} and Bi₂Sr₂CaCu₂O₈ with Some Oxides Used as Substrates of Thin Superconducting Films." Materials Research Bulletin 24, No. 10 (October 1989): 1295-1302.
- [4] Masuda, Y., Matsubara, K., Ogawa, R., and Kawate, Y. "Production of YBa₂Cu₃O_{7-x} Thick Films on Ag Metal Substrate Controlled by Oxygen." Japanese Journal of Applied Physics 31, Part 1, No. 9A (September 1992): 2709-2715.
- [5] Ma, Q. Y., Shu, C., Yang, E. S., Chang, C. A., and Farrell, C. E. "Patterning of High T_c Superconducting Thin Films on Si Substrates." In Superconductivity Applications for Infrared and Microwave Devices in Orlando, Florida, April 19-20, 1990, by SPIE. Bellingham, WA: Proceedings of SPIE, 38-43.
- [6] Shaw, D. T., Narumi, E., Yang, F., and Patel, S. "Role of Buffer Layers in the Laser-ablated Films on Metallic Substrates." In Progress in High-Temperature Superconducting Transistors and Other Devices in Santa Clara, California, October 4-5, 1990, by SPIE. Bellingham, WA: Proceedings of SPIE, 1990, 214-220.
- [7] Ballentine, P. H., Kadin, A. M., Fisher, M. A., Mallory, D. S., and Donaldson, W. R. "Microlithography of High-Temperature Superconducting Films: Laser Ablation vs. Wet

- Etching." IEEE Transactions on Magnetics 25, No. 2 (March 1989): 950-953.
- [8] Shibata, S., Kitagawa, T., Okazaki, H., and Kimura, T. "C-Axis-Oriented Superconducting Oxide Film by the Sol-Gel Method." Japanese Journal of Applied Physics 27, No. 4 (April 1988): 646-648.
- [9] Deslandes, F., Raveau, B., Dubots, P. and Legat, D. "Reserach of the Effective Role of Silver Additions to $\text{YBa}_2\text{Cu}_3\text{O}_7$." Solid State Communications 71, No. 5 (1989): 407-410.
- [10] Martens, J. S., Pance, A., Char, K., Lee, L., Whiteley, S., and Hietala, V. M. "Superconducting Josephson Arrays as Tunable Microwave Sources Operating at 77K", Applied Physics Letters 63, No.12 (September 20, 1993): 1681-1683.
- [11] Chew, W., Riley, A. L., Rascoe, D. L., Hunt, B. D., Foote, M. C., Cooley, T. W., and Bajuk, L. J. "Design and Performance of a High- T_c Superconductor Coplanar Waveguide Filter." IEEE Transaction on Microwave Theory and Techniques 39, No. 9 (September 1991): 1455-1461.
- [12] Bonetti, R. R., and Williams, A. E. "Preliminary Design Steps for Thin-Film Superconducting Filters." In the 1990 IEEE MTT-S International Microwave Symposium Digest in Dallas, Texas, May 8-10, 1990, by the IEEE Microwave Theory & Techniques Society. Piscataway, New Jersey: IEEE, 1990, 273-276.
- [13] Lyons, W. G., Bonetti, R. R., Williams, A. E., Mankiewich, P. M., O'Malley, M. L., Hamm, J. M., Anderson, A. C., Withers, R. S., Meulenberg, A., and Howard, R. E. "High- T_c Superconducting Microwave Filters." IEEE Transactions on Magnetics 27, No. 2 (March 1991): 2537-2539.
- [14] Talisa, S. H., Janocko, M. A., Jones, C. K., McAvoy, B. R., Talvacchio, J., Wagner, G. R., Moskowitz, C., Buck, D. C., Billing, J., and Brown, R. "Microwave Superconducting Filters." IEEE Transactions on Magnetics 27, No. 2 (March 1991): 2544-2547.
- [15] Talisa, S. H., Janocko, M. A., Moskowitz, C., Talvacchio, J., Billing, J. F., Brown, R.,

- Buck, D. C., Jones, C. K., McAvoy, B. R., Wagner, G. R., and Watt, D. H. "Low- and High-Temperature Superconducting Microwave Filters." IEEE Transactions on Microwave Theory and Techniques 39, No. 9 (September 1991): 1448-1454.
- [16] Bhasin, K. B., Warner, J. D., Romanofsky, R. R., Heinen, V. O., and Chorey, C. M. "High Temperature Superconducting Thin Film Microwave Circuits: Fabrication, Characterization, and Applications." In Superconductivity Applications for Infrared and Microwave Devices in Orlando, Florida, April 19-20, 1990, by SPIE. Bellingham, WA: Proceedings of SPIE, 1990, 71-82.
- [17] Bhasin, K. B., Chorey, C. M., Warner, J. D., Romanofsky, R. R., Heinen, V. O., Kong, K. S., Lee, H. Y., and Itoh, T. "Performance and Modeling of Superconducting Ring Resonators at Millimeter-Wave Frequencies." In the 1990 IEEE MTT-S International Microwave Symposium Digest in Dallas, Texas, May 8-10, 1990, by the IEEE Microwave Theory & Techniques Society. Piscataway, New Jersey: IEEE, 1990, 269-272.
- [18] Wilker, C., Shen, Z. Y., Pang, P., Face, D. W., Holstein, W. L., Matthews, A. L., and Laubacher, D. B. "5 GHz High-Temperature-Superconductor Resonators with High Q and Low Power Dependence up to 90 K." IEEE Transaction on Microwave Theory and Techniques 39, No. 9 (September 1991): 1462-1467.
- [19] Takemoto, J. H., Jackson, C. M., Hu, R., Manasevit, H. M., Petite-Hall, C., Burch, J. F., St. John, D. C., Lee, A., and Daly, K. P. "High- T_c Superconducting Microstrip Resonators and Filters on LaAlO_3 ." In the Proceedings of the 45th Annual Symposium on Frequency Control in Los Angeles, California, May 29-31, 1991, by the IEEE Ultrasonics, Ferroelectrics, & Frequency Control Society. Piscataway, New Jersey: IEEE, 1991, 477-481.
- [20] Oates, D. E., Anderson, A. C., and Steinbeck, J. "Superconducting Resonators and High- T_c Materials." In the Proceedings of the 42nd Annual Frequency Control

- Symposium in Baltimore, Maryland, June 1-3, 1988, by the IEEE Ultrasonics, Ferroelectrics, & Frequency Control Society. Piscataway, New Jersey: IEEE, 1988, 545-549.
- [21] Oates, D. E., Lyons, W. G., and Anderson, A. C. "Superconducting Thin-Film $\text{YBa}_2\text{Cu}_3\text{O}_{7-x}$ Resonators and Filters." In the Proceedings of the 45th Annual Symposium on Frequency Control in Los Angeles, California, May 29-31, 1991, by the IEEE Ultrasonics, Ferroelectrics, & Frequency Control Society. Piscataway, New Jersey: IEEE, 1991, 460-466.
- [22] Namordi, M. R., Mogro-Campero, A., Turner, L. G., and Hogue, D. W. "Comparison of High-Temperature-Superconductor and Metal-Based Resonators." IEEE Transactions on Microwave Theory and Techniques 39, No. 9 (September 1991): 1468-1474.
- [23] Tazoh, Y. "Evaluation of High-Frequency Performances of a Superconducting Base Transistor Using High- T_c Materials." IEEE Transactions on Magnetics 27, No. 2 (March 1991): 3316-3319.
- [24] Tamura, H., Yoshida, A., Gotoh, K., Hasuo, S., and Van Duzer, T. "A Superconducting Resonant Tunneling Transistor with Insulating Base Layer." IEEE Transactions on Magnetics 27, No. 2 (March 1991): 2594-2597.
- [25] Hashiguchi, S., Min, E., Awaji, T., Asano, K., Kabasawa, U., Sakuta, K., and Kobayashi, T. "Selective Epitaxial Growth of YBaCuO Thin Films and its Application to MOS-FET Fabrication." IEEE Transactions on Magnetics 27, No. 2 (March 1991): 1441-1444.
- [26] Glasser, L. A. "Circuit Models and Applications of the Superconducting Field-Effect Transistor." IEEE Journal of Solid-State Circuits 24, No. 5 (October 1989): 1441-1417.
- [27] Satchell, J. S., Edwards, J. A., Chew, N. G., and Humphreys, R. G. "High Temperature Superconducting Vortex Flow Transistor." Electronics Letters 28, No. 8 (April 9, 1992): 781-783.

- [28] Konopka, J, Sobolewski, R., Jung, G., Kula, W., Konopka, A., Giertowski, P., and Lewandowski, S. J. "Microwave Detectors Based on Granular High- T_c Thin Films." IEEE Transactions on Microwave Theory and Techniques 38, No. 2 (February 1990): 160-164.
- [29] Chaloupka, H., Piel, H., Pischke, A., Gieres, G., Peiniger, M., Schultz, L., Bode, M., and Schubert, J. "High-Temperature Superconductor Meander-Antenna." In the 1992 IEEE MTT-S International Microwave Symposium Digest in Albuquerque, New Mexico, June 1-5, 1992, by the IEEE Microwave Theory & Techniques Society. Piscataway, New Jersey: IEEE, 1992, 189-192.
- [30] Van Duzer, T., and Turner, C. W. Principles of Superconductive Devices and Circuits. New York: Elsevier, 1981.
- [31] Gupta, L.C., ed. Theoretical and Experimental Approaches to High- T_c and Conventional Superconductivity. A Child's Guide to BCS by Finnemore, D. K. Commack, NY: Nova Science Publishers Inc, 1992.
- [32] Kresin, V. Z., Wolf, S. A., and Deutscher, G. "Correlation between microstructure and properties of high T_c films: application to microwave properties" Materials Science and Engineering B: Solid-State Materials for Advanced Technology B12, No. 4 (February 29, 1992): 365-368
- [33] Mei, K. K., and Liang, G. C. "Electromagnetics of Superconductors." IEEE Transactions on Microwave Theory and Techniques 39, No. 9 (September 1993): 1545-1552.
- [34] Lee, L. H., Ali, S. M., and Lyons, W. G. "Full-Wave Characterization of High T_c Superconducting Transmission Lines." IEEE Transactions on Applied Superconductivity 2, No. 2 (June 1992): 49-57.
- [35] Pond, J. M., and Weaver, P. "Field and Energy-Density Profiles in Layered Superconductor-Dielectric Structures." In the 1990 IEEE MTT-S International

Microwave Symposium Digest in Dallas, Texas, May 8-10, 1990, by the IEEE

Microwave Theory & Techniques Society. Piscataway, New Jersey: IEEE, 1990, 277-280.

- [36] Catania, P., Hovnanian, N., Cot, L., Pham Thi, M., Kormann, R., and Ganne, J. P. "Influence of Sol-Gel Methods on the Superconducting $\text{YBa}_2\text{Cu}_3\text{O}_{7-x}$ Phase." Materials Reserach Bulletin 25, No. 5 (1990): 631-642.
- [37] Koo, H. S., Wu, P. T., Chen, F. H., and Tsent, T. Y. "Preparation and Properties of gel-derived High T_c $\text{YBa}_2\text{Cu}_3\text{O}_{7-x}$ superconductor." Journal of Materials Science Letters 9, No. 7 (July 1990): 807-809.
- [38] Hayri, E. A., Greenblatt, M., Ramanujachary, K. V., Nagano, M., Oliver, J., Miceli, M. J., and Gerhardt, R. "Magnetic, electrical and microstructural properties of $\text{YBa}_2\text{Cu}_3\text{O}_7$: A comparison of sol-gel, co-precipitated, and solid state processing routes." Journal of Materials Research 4, No. 5, (September/October 1989): 1099-1102.
- [39] Sanjinés, R., Thampi, K. R., and Kiwi, J. "Preparation of Monodispersed Y-Ba-Cu-O Superconductor Particles via Sol-Gel Methods." Journal of the American Ceramic Society 71, No. 12 (December 1988): 512-514.
- [40] Kordas, G. "Sol-Gel Processing of Ceramic Superconductors." Journal of Non-Crystalline Solids 121, nos. 1-3 (May 1, 1990): 436-442.
- [41] Moore, G., Kramer, S., and Kordas, G. "Sol-Gel Processing of $\text{Y}_1\text{Ba}_2\text{Cu}_3\text{O}_{7-x}$ Using Alkoxide Precursors: Two Systems Yielding High Degrees of Thin Film Orientation and Crystal Growth." Materials Letters 7, No. 12 (March 1989): 415-424.
- [42] Hirano, S., Hayashi, T., and Miura, M. "Preparation of $\text{Ba}_2\text{YCu}_3\text{O}_{7-x}$ Thin Films with Preferred Orientation through an Organometallic Route." Journal of the American Ceramic Society 73, No. 4 (April 1990): 885-888.
- [43] Masuda, Y., Tateishi, T., Matsubara, K., Ogawa, R., and Kawate, Y. "Preparation of $\text{YBa}_2\text{Cu}_3\text{O}_{7-x}$ (YBCO) Superconductive Film Using Sol-Gel Method." Japanese Journal

- of Applied Physics 30, No. 7 (July 1991): 1390-1397.
- [44] Shibata, S., Kitagawa, T., Okazaki, H., Kimura, T., and Murakami, T.
"Superconducting Oxides by the Sol-Gel Method Using Alkoxides." Japanese Journal of Applied Physics 27, No. 1 (January 1988): 53-54.
- [45] Murakami, H., Yaegashi, S., Nishino, J., Shiohara, Y., and Tanaka, S. "Synthesis of $\text{YBa}_2\text{Cu}_3\text{O}_8$ Powders by Sol-Gel Method under Ambient Pressure." Japanese Journal of Applied Physics 29, No. 3 (March 1990): 445-446.
- [46] Masuda, Y., Ogawa, R., Kawate, Y., Matsubara, K., Tateishi, T., and Sakka, S.
"Preparation of $\text{YBa}_2\text{Cu}_3\text{O}_{7-x}$ superconducting films through the sol-gel method using metal alkoxides as starting materials." Journal of Materials Reserach 7, No. 4 (April 1992): 819-826.
- [47] Nagano, M., and Greenblatt, M. "High Temperature Superconducting Films by Sol-Gel Preparation." Solid State Communications 67, No. 6 (1988): 595-602.
- [48] Umeda, T., Kozuka, H., and Sakka, S. "Fabrication of $\text{YBa}_2\text{Cu}_3\text{O}_{7-d}$ Superconducting Fibers by the Sol-Gel Method." Advanced Ceramic Materials 3, No. 5 (1988): 520-522.
- [49] Hussain, A. A., and Sayer, M. "Chemical Fabrication of Superconducting Y-Ba-Cu-Oxide Films." Journal of Superconductivity 5, No. 1 (February 1992): 11-18.
- [50] Kwon, C. H., Cho, S. M., Choi, Y. H., Moon, B. K., Yang, D. Y., and Kim, S. T.
"Formation of Y-Ba-Cu-O Thin Films by Sol-Gel Technique." Physica C: Superconductivity 185-189, No. 4 (December 1, 1991): 2107-2108.
- [51] Khan, S. A., Barboux, P., Bagley, B. G., and Torres, F. E. "Rheology of Precursors for Sol-Gel Derived $\text{YBa}_2\text{Cu}_3\text{O}_{7-x}$ Superconductors." Journal of Non-Crystalline Solids 110, Nos. 2-3 (August 1989): 142-152.
- [52] Kitagawa, T., Shibata, S., Okazaki, H., Kimura, T., and Enomoto, Y. "High- T_c Superconducting Film on Silicon Substrate with ZrO_2 Buffer Layer." Japanese Journal of Applied Physics 27, No. 6 (June 1988): 1113-1115.

- [53] Gupta, A., Jagannathan, R., Cooper, E. I., Giess, E. A., Landman, J. I., and Hussey, B. W. "Superconducting oxide films with high transition temperature prepared from metal trifluoroacetate precursors." Applied Physics Letters 52, No. 24 (June 13, 1988): 2077-2079.
- [54] Dishal, M. "Alignment and Adjustment of Synchronously Tuned Multiple-Resonant-Circuit Filters." Proceedings of the I.R.E. (November, 1951): 1448-1455.
- [55] Talvacchio, J., and Wagner, G. R. "High- T_c film development for electronic applications." In Superconductivity Applications for Infrared and Microwave Devices in Orlando, Florida, April 19-20, 1990, by SPIE. Bellingham, WA: Proceedings of SPIE, 1990, 2-12.
- [56] Beasley, M. R. "High Temperature Superconductive Thin Films." Proceedings of the IEEE 77, No. 8 (August 1989): 1155-1163.
- [57] Scheel, H. J., Berkowski, M., and Chabot, B. "Problems in epitaxial growth of high- T_c superconductors." Journal of Crystal Growth 115, (1991): 19-30.
- [58] Bourdillon, A. and Bourdillon, N. X. Tan. High Temperature Superconductors: Processing and Science. Boston: Academic Press, Inc., 1994.
- [59] Schieber, M., Han, S. C., Ariel, Y., Chokron, S., Tsach, T., Maharizi, M., Deutscher, C., Racah, D., Raizman, A., and Rotter, S. "Comparison of thin films of $YBa_2Cu_3O_{7-x}$ deposited by physical (laser ablation) and chemical (OMCVD) methods for device applications." Journal of Crystal Growth 115, 1991: 31-42.
- [60] Lubig, A., Buchal, C., Schubert, J., Copetti, C., Guggi, D., Jia, C. L., and Stritzker, B. "Epitaxial growth of $YBa_2Cu_3O_{7-x}$ thin films on Si(100) with zirconia buffers of varying crystalline quality and structure." Journal of Applied Physics 71, No. 11 (June 1, 1992): 5560-5564.
- [61] Fork, D. K., Garrison, S. M., Hawley, M., and Geballe, T. H. "Effects of homoepitaxial surfaces and interface compounds on the in-plant epitaxy of YBCO films on yttria-

- stabilized zirconia." Journal of Materials Research 7, No. 7 (July 1992): 1641-1651.
- [62] Rosenbaum, J. F. Bulk Acoustic Wave Theory and Devices. Norwood, MA: Artech House, Inc., 1988.
- [63] Beyers, R., and Ahn, B. T. "Thermodynamic Considerations in Superconducting Oxides." Annual Review of Material Science 21 (1991): 335-372.
- [64] Goff, E. D., and Weber, R. W. *** MRS Paper reference
- [65] Goff, E. D. and Braymen, S. D. "A novel approach to the deposition of piezoelectric thin films." Materials Letters 21 (1994): 347-349.
- [66] Ledbetter, H., and Lei, M. "Monocrystal elastic constants of orthotropic $Y_1Ba_2Cu_3O_7$: An estimate." Journal of Materials Research 6, No. 11 (Nov. 1991): 2253-2255.
- [67] Auld, B. A. Acoustic Fields and Waves in Solids New York: John Wiley & Sons, 1973.
- [68] Libra Rel. 4.0, EESOF Corporation, Boulder, Colorado.

ACKNOWLEDGMENTS

I would like to thank my advisor and friend, Dr. Robert Weber, for his guidance and assistance throughout my tenure at Iowa State University. His encouragement, support, and commitment of time were invaluable in the completion of this dissertation project. I would also like to thank the other members of my committee, Dr. Stanley Burns, Dr. John Basart, Dr. David Stephenson, Dr. Scott Chumbley, and Dr. Howard Shanks for their time, effort, and guidance in the completion of this doctoral dissertation.

There are some friends who have made my experience at Iowa State University a memorable one, and I would like to thank them for their friendship. These people include (in alphabetical order): Kent Blomgren, Steve Braymen, Dr. Chuck Cychosz, Scott DeBoer, Joel Fastenau, Jeff Galvin, Milt Haar, Heather Hobson, Dr. George Karas, Aimee Kingery, Kevin McCarville, Dana McCullough, Erick Michel, Ron O'Toole, Melissa Phillips, Dave Schmidt, Kristin Stainer, Casey Thielen, Dave Turner, Keith Turner, and many others.

Thanks also go to my friends from Minnesota, as well as many thanks to my family: Mom C., Dad C., Nancy & Brian, Diane & Chris, Mike, Dick & Diane, Laddie, and Casey, but I would like to especially thank my parents Kathy and Bob. Their love and guidance through the years have made me what I am today. Most important on my list of individuals to thank is my wife Karen. Her constant love and support have helped to guide me through the past few years at ISU. For this and so many other reasons, I give her all my love.

This research was performed at Iowa State University's Microelectronic Research Center with funding made possible by a Department of Education fellowship, and a grant from the Center for Advanced Technology Development (CATD). Additional processing was made provided by a collaboration with Dr. Doug Lowndes and Mukund Godbole at Oak Ridge National Laboratories.

APPENDIX A: PUBLICATIONS

Paper #1, Published in Materials Letters, Volume 21 (November, 1994): 347-349 [65]

A Novel Approach to the Deposition of Piezoelectric Thin Films.

Edward D. Goff and Steven D. Braymen

Iowa State University, Ames, IA 50011

A novel technique for the deposition of piezoelectric thin films is presented. By applying the benefits of DC Magnetron Sputtering and Radio Frequency Plasma Enhanced Chemical Vapor Deposition, a new technique denoted Direct Current Biased Radio Frequency Plasma Enhanced Chemical Vapor Deposition, or DCB-RFPECVD, has been developed. A DC bias was placed on the RF plasma; the bias voltage was much greater than typically used in RF PECVD. The high deposition rate and uniformity associated with RF PECVD are maintained in this process, and an enhanced crystallographic orientation to the thin film can be obtained.

INTRODUCTION:

Piezoelectric thin films are being realized in numerous applications as microelectronic circuits continue to decrease in size. Microwave transducers, resonators, sensors, and dielectrics in capacitors utilizing the unique properties of AlN and other piezoelectrics are used in many applications today. To produce high quality piezoelectrics is a challenge due to the limitations of the technology available today.

Chemical Vapor Deposition systems use thermal energy at high temperatures (>500°C) to deposit films. Using thermal CVD to deposit piezoelectrics is not beneficial

because the crystalline structure of the resultant thin film is either polycrystalline, or the temperature of reaction is not conducive to microelectronic processing.^[1,2] The process of Plasma Enhanced Chemical Vapor Deposition (PECVD) produces uniform thin films at high rate.^[3] The advantage of RF PECVD is that the films are deposited at lower temperatures. However, this technique yields films with inferior piezoelectric properties due to the random orientation of the crystal structure. Although the plasma in RF PECVD is automatically DC biased, this bias is typically 10-12V which is insufficient for producing crystal alignment in piezoelectric films. Experimentally it has been determined that a minimum of 40V DC is required for piezoelectric activity in Aluminum Nitride.

Materials such as CdS, ZnO, CdSe, AlN and BeO are all piezoelectric crystals which when grown with the Z axis normal to the specimen surface exhibit a strong piezoelectric effect for longitudinal acoustic waves.^[4] DC-biased Magnetron Sputtering produces this highly aligned crystal orientation. The alignment of the crystals is a result of the potential difference across the dark space between the substrate and the plasma. This potential is determined by the DC biasing of the plasma. However, this process results in films with non-uniform thickness. ^[5]

The positive qualities of both PECVD and DC-Magnetron Sputtering processes may be realized within a single system, thereby producing superior films. These positive qualities include (1) the uniformity of the thickness of the thin film deposition, which is a product of the RF PECVD process, and (2) the superior crystal orientation, which is a result of the DC biasing in the RF plasma.

PROCEDURE:

A parallel plate Radio Frequency (RF) reactor (LFE model PFS/PDE/PDS - 1002) was modified by adding an anode ring positioned between the two plates as shown in Figure 1. This modification enables the plasma to acquire both an RF and a DC bias. A sample

reaction to produce a thin film of Aluminum Nitride was attempted. Reaction gases, Trimethyl Aluminum ($\text{Al}(\text{CH}_3)_3$) and Nitrogen (N_2), were introduced at a reduced pressure and allowed to react in the plasma. The parameters used for this deposition were:

- 500 Watts RF power
- 13.5 MHz for the plasma frequency
- +60 Volts DC bias
- 100 mtorr pressure
- input gas flow rate of 100 sccm for both the nitrogen and Trimethyl Aluminum (TMA)

The first step in the deposition was to start up the RF plasma using nitrogen to equilibrate the system. The DC bias was applied to the N_2 plasma. Initially, the plasma occurred across both plates, but as the DC bias was increased, the plasma shape changed and was confined to the central region of the anode ring. The system is shown in Figure 2. The low-pass filter was used to filter out the RF power to protect the DC source. The substrate used for this initial test was a polished <100> Silicon wafer.

RESULTS AND DISCUSSION:

This reaction yielded a uniform deposition of material. The initial deposition resulted in an Aluminum-Carbon-Nitrogen product on the surface of the wafer. The TMA reacted incompletely with the nitrogen in the plasma creating the Al-C-N mixture. The incomplete reaction was a result of uneven gas flow into the reaction area with the Nitrogen not reacting in the correct stoichiometric proportion with the Aluminum. Ammonia (NH_3) may be substituted for nitrogen, potentially enhancing the quality of the film due to the increased reactivity of the ammonia in the plasma. The films were not fully characterized due to the preliminary nature of the process. Nevertheless, this process shows great promise to achieve highly oriented thin films.

Piezoelectric thin films must be highly oriented with uniform film thickness for electronic applications. The concept of the DCB-RFPECVD was shown, and further experimentation and optimization of the deposition remain to be performed. This work resulted in an improved method for the deposition of Aluminum Nitride as a piezoelectric material. However, this process is not limited to Aluminum Nitride and may be adapted to any material systems currently being deposited by PECVD, where a strong crystal orientation in the films is desired. Three such materials are Silicon Dioxide (SiO_2) Zinc Oxide (ZnO), and Lead Lanthanum Zirconate Titanate (PLZT).

ACKNOWLEDGEMENTS:

The authors would like to thank the Microelectronics Research Center of Iowa State University for the use of their facilities and equipment.

REFERENCES:

- [1] J. K. Liu, *Journal of Applied Physics* 46 (1975) 3703.
- [2] W. M. Yim, *Journal of Applied Physics* 44 (1973) 292.
- [3] Fumio Hasegawa, *Japanese Journal of Applied Physics* 26 (1987) 1555.
- [4] Velimir Ristic, *Principles of Acoustic Devices* (John Wiley & Sons, New York, 1983).
- [5] J.S. Morgan, *Journal of Materials Research* 5 (1990) 2677.

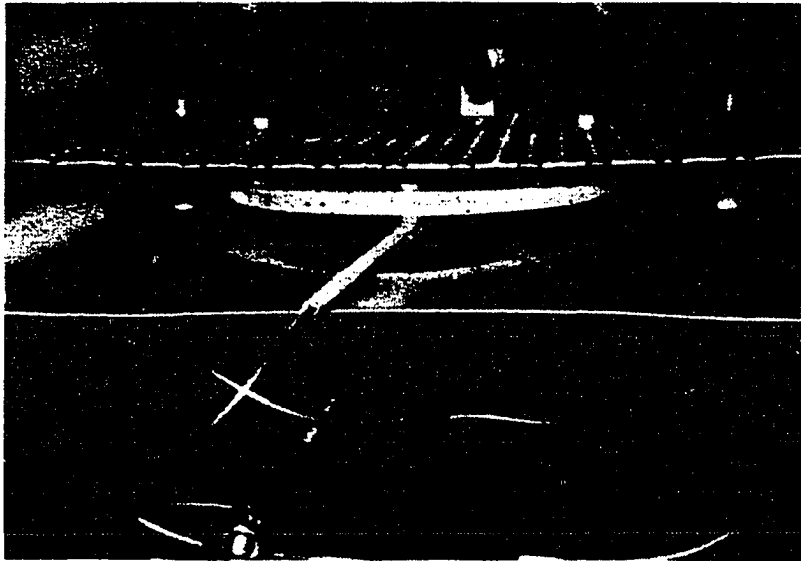


Figure 1: Photograph taken of the actual experimental setup used for the deposition of Aluminum Nitride.

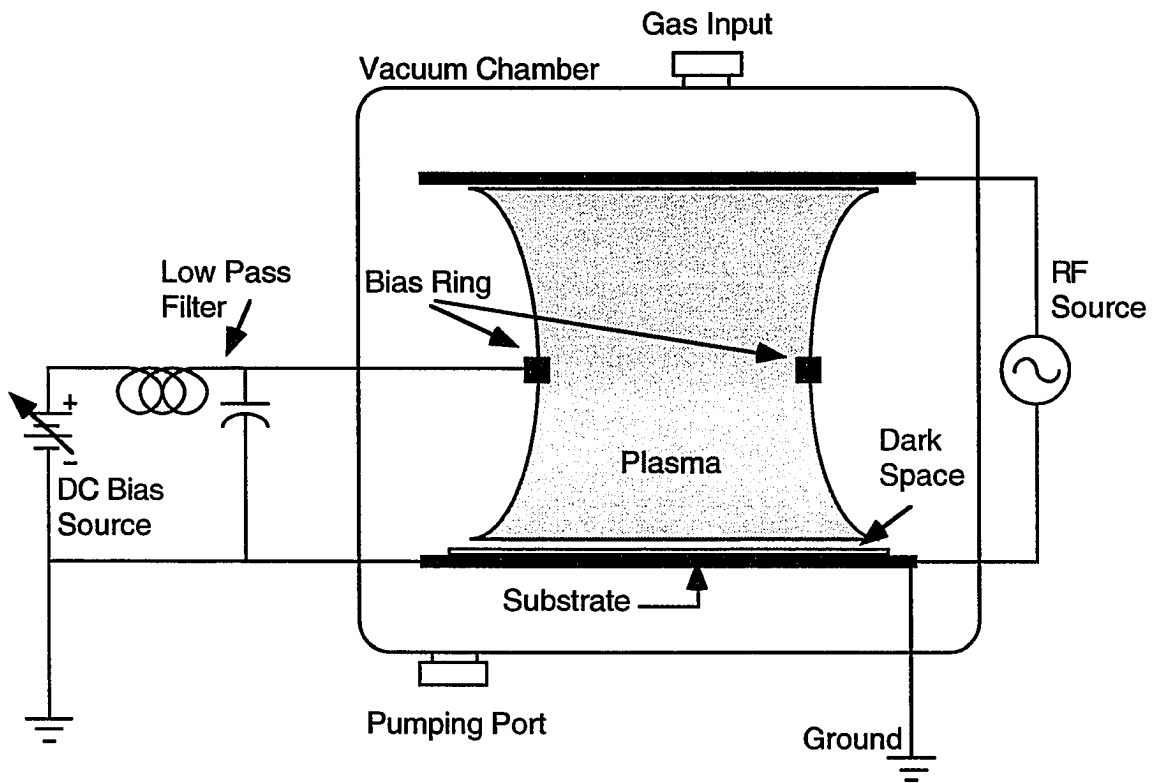


Figure 2: Schematic diagram of the DCB-RFPECVD system.

Paper #2, Presented at the 1994 Fall conference of the Materials Research Society, Boston Massachusetts. [64]

A MODIFIED TRANSMISSION LINE APPROACH TO THE ANALYSIS OF SUPERCONDUCTING MICROWAVE RESONATORS

EDWARD D. GOFF AND ROBERT J. WEBER

Microelectronics Research Center, Iowa State University, Ames, IA 50011

ABSTRACT

A technique for modeling a superconductor contacted piezoelectric microwave resonator is presented. A transmission line method of modeling the superconductor as a two fluid model is shown to agree with the London penetration depth, and is modeled to take into account the superconductor to normal transition. By including both the normal conductor effects along with the superconductor effects, crystal quality can be factored into this model using an analytical approximation. A two dimensional model for the superconductor, applying experimental results from $Y_1Ba_2Cu_3O_{7-x}$ for circuit elements, is analyzed. The superconducting layer is modeled as an electrical circuit in combination with an acoustical circuit to model its effect on a piezoelectric resonator. The acoustical equivalent of the superconductor including mass loading effects and terminations are taken into account in the Mason model acoustical equivalent circuit.

BACKGROUND AND OVERVIEW

The integration of piezoelectric and superconductive technologies will allow a greater range of possible microwave system applications to be fabricated on a smaller scale due to the increase in performance of the devices. The goal of this analysis is to model a hybrid superconductor piezoelectric resonator structure using transmission line theory. To accomplish this goal, an equivalent circuit must be set up which correctly approximates the entire structure. The structure to be simulated is a High-Temperature Superconductor / Aluminum Nitride / High-Temperature Superconductor resonator structure, hereafter abbreviated by HTSC - AlN - HTSC.

The calculation will be broken down into sections dealing with specific aspects of the analysis. The first section analyzed will be the equivalent inductance of the HTSC. The second section analyzed will be the terminating resistance at the free space boundary. The third section will be to add the Mason model to the circuit to model the piezoelectric resonator and the mass loading effects of the superconductor and the substrate. The results of this analysis are then presented. Figure 1 shows the electromagnetic model for the superconducting transmission line structure.

The results from this analysis agree well with predicted superconductor analysis, as well with superconducting theory. The penetration depth is found to be consistent with both measurements and this analysis.

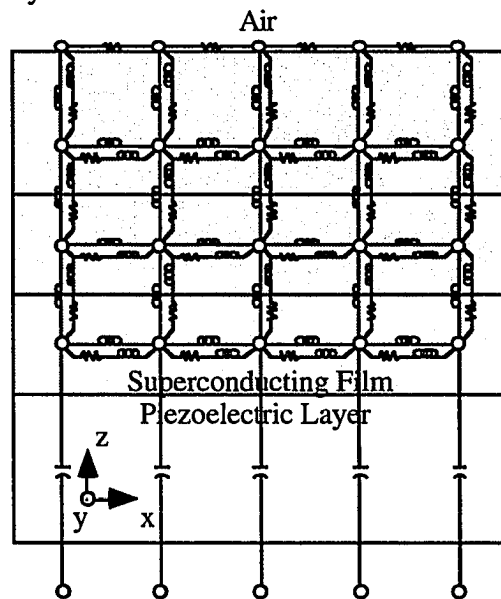


Figure 1: HTSC - AlN Resonator Equivalent Circuit Diagram

THEORY

Determining Equivalent Inductance For A Section Of Superconductor

The intent of the inductor analysis is to find an equivalent circuit element that may be used in the transmission line analysis. Using a section of material with dimensions of dx , dy , and dz , a current is introduced and assumed to flow in only the x - direction. There is assumed to be no magnetic field variation in the y - direction, or $\partial H_y / \partial y = 0$.

The magnetic energy stored in a section of material is given in equation 1 as

$$W_M = \frac{1}{2} \iiint_V \vec{B} \cdot \vec{H} \cdot dv = \frac{1}{2} \iiint_V \mu H^2 \cdot dv \quad (1)$$

Setting equation 1 equal to the energy stored in an inductor we obtain

$$LI^2 = \iiint_V \mu_o H^2 \cdot dv \quad (2)$$

where $\vec{B} = \mu \vec{H}$, $I = \iint_S \vec{J} \cdot ds$, and $\mu = \mu_o = 4\pi \times 10^{-7}$ H/m in HTSC. Along with Ampere's Law in integral form, we now have two constitutive relations between the magnetic fields and the current passing through the sample. Analyzing the differential current traveling in the x-direction, and approximating the integrals as differentials while assuming that $\partial H_y / \partial y = 0$, Ampere's law can be approximated as

$$J_x(z) \approx -\frac{\partial H_y}{\partial z}. \quad (3)$$

Substituting equation 3 into equation 2 we can now eliminate the current from the previous equations:

$$L \left(\iint_S -\frac{\partial H_y}{\partial z} \cdot dy \cdot dz \right)^2 = \iiint_V \mu_o H_y^2 \cdot dx \cdot dy \cdot dz. \quad (4)$$

Assuming a solution of the form $\vec{H} = \vec{H}_o e^{-\alpha z}$, we can solve equation 4 for the equivalent inductance in the circuit. Expanding the exponentials and simplifying, the resulting inductance is

$$L_x = \frac{\mu_o \Delta x}{\alpha^2 \Delta y \Delta z} \quad (5)$$

where L_x is the incremental inductance of a current flowing in the x - direction. A similar calculation was performed for L_z . These results are for a sample that is entirely superconducting. In this analysis, the case when the sample is not entirely superconducting will be investigated, since for most HTSC there remains a small finite resistance that will be accounted for in the transmission line analysis. The effective area of the superconductor will be treated as being decreased by a percentage equal to the ratio of superconducting to non-superconducting regions, i.e. equation 5 becomes

$$L_{x-sc} = \frac{\mu_o \Delta x}{\alpha^2 K \Delta y \Delta z} \quad (6)$$

where K is the ratio of superconducting to non-superconducting regions. Similarly, the non-superconducting region will have an inductive component and a resistive component to its impedance given by

$$L_{x\text{-NSC}} = \frac{\mu_0 \Delta x}{\alpha^2 (1 - K) \Delta y \Delta z}, \quad R_{x\text{-NSC}} = \frac{\rho \Delta x}{(1 - K) \Delta y \Delta z} \quad (7)$$

where ρ is the resistivity of the superconductor just before the sample passes through the transition and becomes superconducting. [1]

Determining The Equivalent Resistance For The Air-Superconductor Interface

The equivalent resistance as shown in Figure 1 at the free space boundary of the sample simulates the power lost into the half space that may be used in the transmission line analysis. Assuming an area $\Delta x \Delta y$, we will consider the power in free space at the boundary. Starting with the Poynting vector in the z direction, $P_z = E_x \times H_y$, we then use plane wave relations to relate the electric and magnetic fields in free space, $H_y = E_x / \eta$, where $\eta = \sqrt{\mu_0 / \epsilon_0} = 377 \Omega$. Applying these principles to the Poynting vector we obtain

$$P_z = E_x \times \frac{E_x}{\eta} = \frac{E_x^2}{\eta} \quad (8)$$

where the actual power in the z - direction can be found by multiplying by the area, $\Delta x \Delta y$. Equating this result with the standard power equation for a resistor, $P = V^2 / R$ where V is found by using Maxwell's equation in integral form as the voltage drop across a distance Δx , or

$$V = - \int \vec{E} \cdot d\vec{l} = - E_x \Delta x \quad (9)$$

Equating the power of a resistor with the Poynting vector power, we obtain the equivalent resistance,

$$R = \frac{\eta \Delta x}{\Delta y} \quad (10)$$

Mason Model Calculation

In Figure 1 there is a capacitor across the AlN structure. This is only partially correct, since there are other effects due to the piezoelectric resonator structure such as mass loading. In a piezoelectric, the electric field interacts with the crystal structure of the lattice creating stress and strain across the lattice. The model chosen is the Mason model and is shown in Figure 2.[2] The electrical connections shown in Figure 2 will connect to every port in the x - direction of the simulated structure between both the top and bottom superconductor layer. The elements in the circuit shown in Figure 2 are calculated from the acoustical properties of the materials involved.

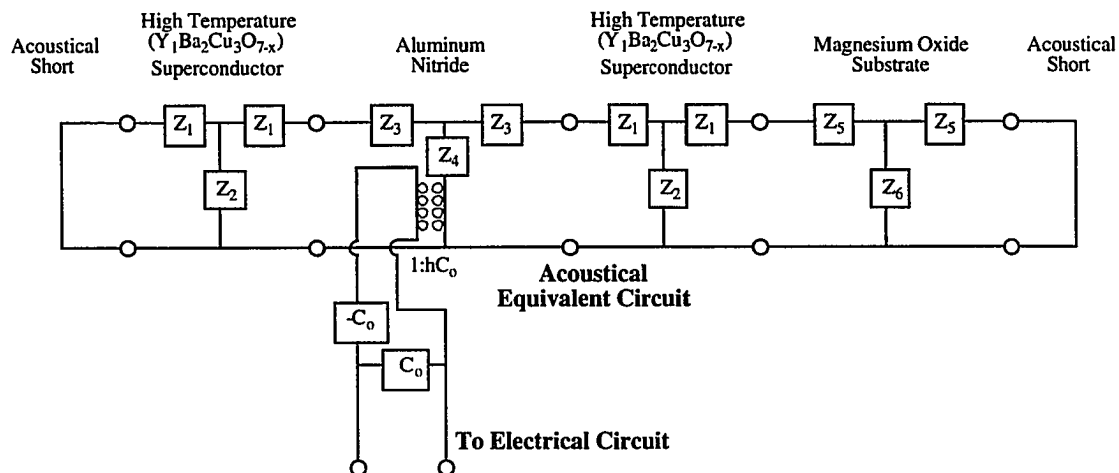


Figure 2: Mason Model Equivalent Circuit.

Note that both the piezoelectric and acoustic loading effects are taken into account in the Mason model, thus yielding a fairly accurate result. [2] The resulting electrical equivalent circuit for the Mason model is a reactance in parallel with a resistance. This circuit accurately models the acoustic effects of the different layers, and introduces these effects correctly into the transmission line analysis.

To simulate this Mason model, a Libra^(tm) [3] circuit was designed that corresponds directly with Figure 2. Employing material constants for HTSC, AlN, and MgO, the circuit was simulated and the results were used to model the admittance at resonance. Since not all material constants are available for HTSC and to simplify the analysis of the structure, some approximations were made. The acoustical loss of the superconductor was assumed to be equivalent to that of Al and MgO was not included in the Libra simulation in order to an overmoded circuit response. The values for the real and imaginary admittance were found at the resonant frequency of 1 GHz and are equal to $Y_{\text{resonance}} = 707.88 + j64.60 \mu\text{S}$ for the area

used. This is the acoustical equivalent to the HTSC - AlN - HTSC circuit for a $20 \mu\text{m} \times 20 \mu\text{m}$ square at the HTSC - AlN interface. This calculated result replaces the capacitor impedance of the AlN in Figure 1 and models the physical parameters of the piezoelectric.

RESULTS

FORTTRAN code was written taking all of these elements into account. The strategy used to solve this circuit was to input the admittance of each of the elements into the array, and then invert the array to obtain the impedances at each point in the matrix, $[Y]^{-1} = [Z]$. All the impedances are then referenced to the first upper HTSC node for a plane of reference. Assuming a 1A current passing into the sample, the potentials across the sample are equal to the impedance values of the Z matrix. Therefore, currents and the electric field potential may be found by

$$I = \frac{\Delta V}{Z} = \Delta V \cdot Y = (V_i - V_j) \cdot Y_{ij} \approx (Z_i - Z_j) \cdot Y_{ij} \quad (11)$$

$$E \approx \frac{\Delta V}{dx} \approx \frac{V_i - V_j}{dx} \approx \frac{Z_i - Z_j}{dx} \quad (12)$$

where i and j are adjacent node numbers in the calculation.

Values for the specific elements and some of the parameters for analyzing the circuit were found from the literature or were obtained from Libra. [4] The potential is shown in Figure 3 in the form of a contour plot, and the current is shown in Figure 4 in the form of a vector field plot. The conclusions that may be drawn from these plots are that the current in the superconductor remains near the lower edge of the sample near the AlN, and does not propagate above the superconducting penetration depth. As can be seen in the current density plot, there is very little current above the third tier of nodes, and in the potential plot, the values are even more remarkable. In the potential plot, the potential decreases rapidly both in the z - direction, as well as decreasing somewhat in the x - direction. These results verify the penetration depth in showing that the current does not flow in the upper regions of the superconductor.

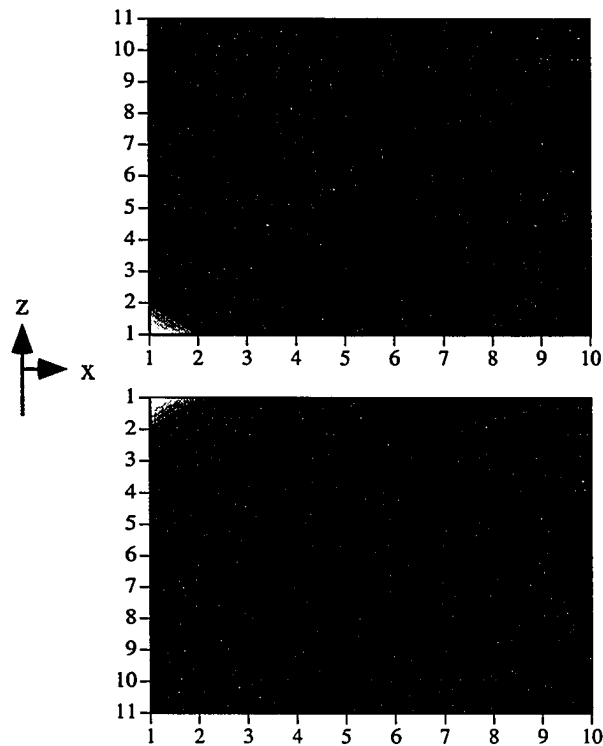


Figure 3: Potential of the HTSC Resonator Sample

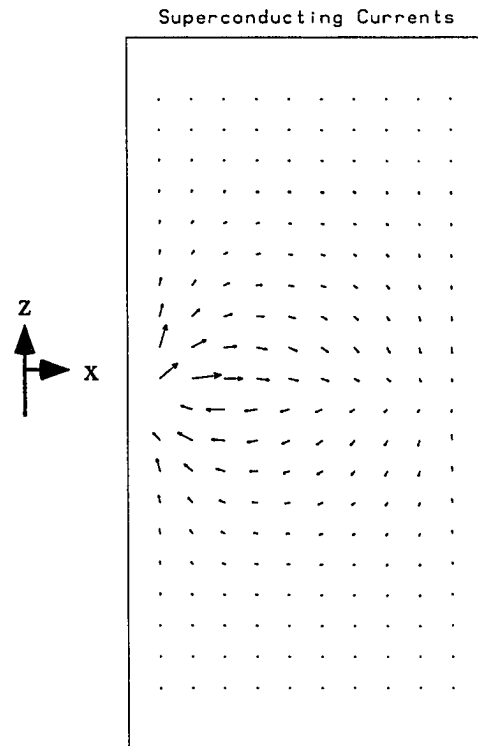


Figure 4: Current flow of the HTSC Resonator Sample

CONCLUSIONS

This theoretical presentation verifies that the penetration depth holds in microwave analysis of High Temperature Superconductors. The superconductor may be modeled using a transmission line model, while continuing to hold to the theoretical approximations. The Mason Model may be applied to High Temperature Superconductor contacted piezoelectrics to account for standard piezoelectric mass loading.

REFERENCES

1. D. W. Cooke, et al., J. Appl. Phys. 68 (5), 2514 (1990).
2. J. F. Rosenbaum, Bulk Acoustic Wave Theory and Devices, (Artech House, Boston, 1988), P. 167.
3. Libra (R) 4.0, (c) 1987-1992 EESOF Corporation.
4. H. Ledbetter and M. Lei., J. Mater. Res. 6 (11), 2253 (1991).

APPENDIX B: SOL-GEL PROCESSING

The procedure for the Sol-Gel processing that was performed at the Microelectronics Research Center had three distinct phases. The first phase in any project is to procure the equipment and resources necessary for the project. The next phase was to adapt the procedure outlined in the literature to the capabilities available at the Microelectronics Research Center. The third phase is the analysis of the results and conclusions.

To process the Sol-Gel HTSCs, the procedure that was chosen was spin-coating. This involves a standard photoresist type of spinner rotating at a controllable speed. A used Headway spinner was purchased and a small spinner chuck was machined to handle the small substrates. Another major piece of equipment that was necessary is an accurate electronic balance (accurate to 0.01g). The accuracy of this device must be high to ensure the correct stoichiometry of the resultant solutions. A high-temperature furnace is required to sinter the HTSCs after the sol-gel processing. MgO substrates were purchased to provide a suitable lattice match to the HTSC. Note that the paper by Gupta, et al. [31] uses Ytria Stabilized Zirconia, but the author has significant experience in working with MgO from 3M Company. The only remaining component is the chemicals themselves. The distinct chemicals and their concentrations will be described in detail below.

The method used for the Sol-Gel processing performed on this dissertation comes from a paper by Gupta, et al. [31]. This paper describes a method for depositing high temperature superconductors using trifluoroacetates of Yttrium, Barium and Copper. The procedure for the creation of the HTSCs by the Sol-Gel method will be outlined presently:

1. Create aqueous trifluoroacetate solutions of the constituent chemicals.
2. Evaporate the water from the trifluoroacetate solutions.
3. Add methanol to the dried trifluoroacetate solution to create a methanol based solution.

4. Perform a gravimetric analysis on the solutions to accurately determine the concentration.
5. Mix together the correct proportion of chemicals to yield $Y_1Ba_2Cu_3$ in solution form.
6. Spin the HTSC solution onto the substrates.
7. Sinter the substrates to create the correct phase of HTSC.
8. Test.

Given in the subsequent paragraphs will be a detailed description of each of these steps.

To create the aqueous trifluoroacetate solutions of the constituent chemicals, an assumed concentration and weight of the solution are necessary. The quantity of Moles per kilogram (Molal) is used in lieu of Moles per liter (Molar) due to the ease of measuring weights accurately on the electronic balance. The solutions require two calculations to obtain the correct chemical amounts, the amount of constituent chemical (Y, Ba, or Cu), and trifluoroacetic acid. The calculations are given presently.

Copper calculations: 600g of 0.3M $Cu(TFA)_2$ (0.3 Molal of Copper TFA)

$$600g(Cu(TFA)_2) \cdot \frac{0.3M(Cu(TFA)_2)}{1000g(Cu(TFA)_2)} \cdot \frac{1Mole(Cu)}{1M(Cu(TFA)_2)} \cdot \frac{63.54g(Cu)}{1Mole(Cu)} = 11.44g \text{ Cu}$$

$$600g(Cu(TFA)_2) \cdot \frac{0.3M(Cu(TFA)_2)}{1000g(Cu(TFA)_2)} \cdot \frac{2Moles(TFA)}{1M(Cu(TFA)_2)} \cdot \frac{114.02g(TFA)}{1Mole(TFA)} = 41.05g \text{ TFA}$$

Barium calculations: 400g of 0.3M $Ba(TFA)_2$ (0.3 Molal of Barium TFA)

$$400g(Ba(TFA)_2) \cdot \frac{0.3M(Ba(TFA)_2)}{1000g(Ba(TFA)_2)} \cdot \frac{1Mole(Ba)}{1M(Ba(TFA)_2)} \cdot \frac{197.35g(BaCO_3)}{1Mole(Ba)} = 23.68g \text{ BaCO}_3$$

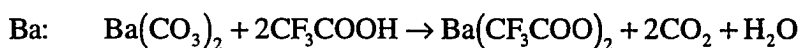
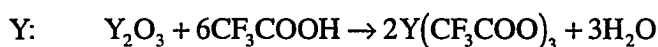
$$400g(Ba(TFA)_2) \cdot \frac{0.3M(Ba(TFA)_2)}{1000g(Ba(TFA)_2)} \cdot \frac{2Moles(TFA)}{1M(Ba(TFA)_2)} \cdot \frac{114.02g(TFA)}{1Mole(TFA)} = 27.36g \text{ TFA}$$

Yttrium calculations: 200g of 0.3M $Y(TFA)_3$ (0.3 Molal of Yttrium TFA)

$$200g(Y(TFA)_3) \cdot \frac{0.3M(Y(TFA)_3)}{1000g(Y(TFA)_3)} \cdot \frac{1Mole(Y)}{1M(Y(TFA)_3)} \cdot \frac{225.81g(Y_2O_3)}{2Mole(Y)} = 6.77g \text{ Y}_2\text{O}_3$$

$$200\text{g}(\text{Y}(\text{TFA})_3) \cdot \frac{0.3\text{M}(\text{Ba}(\text{TFA})_3)}{1000\text{g}(\text{Ba}(\text{TFA})_3)} \cdot \frac{3\text{Moles}(\text{TFA})}{1\text{M}(\text{Ba}(\text{TFA})_3)} \cdot \frac{114.02\text{g}(\text{TFA})}{1\text{Mole}(\text{TFA})} = 20.52\text{g TFA}$$

The procedure for the mixing of the chemicals is as follows. An arbitrary amount of deionized water is placed in a 1000 ml beaker, usually about 500 ml. The acid is then added to this water. The acid solution is heated while the constituent chemical is added to the heating acid. For Yttrium, there must be a great deal of heating since the Y_2O_3 compound does not break up well. At high heat on a stirring hot plate, the procedure takes about 15 minutes. The Barium compound produces a somewhat volatile reaction since it is a carbonate compound. This chemical must be added very slowly to prevent the chemical from “foaming” over the side of the beaker. This procedure takes approximately 15 minutes for the BaCO_3 to react. The Copper in trifluoroacetic acid must have a oxidizing agent to complete the reaction to Copper trifluoroacetate, and the catalyst used is hydrogen peroxide. A small amount of peroxide should be added to the copper and TFA mixture to promote the conversion to Copper trifluoroacetate. If a large amount of peroxide is added, then the chemicals tend to “foam” over the side of the beaker. The chemical reactions for these processes are given below:



After the solutions are mixed, the solutions are filtered to remove any unreacted compounds. These filtered compounds are then placed into a warm oven ($\sim 150^\circ\text{C}$) to evaporate the water in the solution. After a period of time when the solutions are then reduced to a solid, they are taken out of the oven and methanol is added to the individual mixtures. After the new methanol-based solutions have formed, they are filtered again to remove any residual chemicals that did not dissolve into the solvent.

The next procedure is to perform a gravimetric analysis on the resultant solution. This will give an accurate reading of the concentration of the solutions. The filtering described in the previous two steps does not affect the overall stoichiometry of the solution due to the gravimetric analysis. At the conclusion of the analysis, new concentrations are calculated for the solutions. The detailed description of the gravimetric analysis procedure is given in Appendix C.

After the concentrations have been determined, the next step is to mix up the chemical constituents. Typically, it was helpful to find the chemical that was the “limiting reagent,” or the chemical that had the least amount of material left after the filtering. This was accomplished by multiplying the total weight of the solution times the concentration of the solution, while recalling that the proportion of the Y:Ba:Cu must be 1:2:3. An example is shown below. Note that the concentrations have been normalized to one mole of chemical constituent (i.e., CuTFA = $\text{Cu}_1(\text{TFA})_{0.5}$).

$$0.216 \text{ M Y TFA} \times 146.64 \text{ g solution} = 0.03167 \text{ Moles Y} = 0.03167 \text{ Moles } \text{Y}_1\text{Ba}_2\text{Cu}_3 *$$

$$0.349 \text{ M Ba TFA} \times 181.50 \text{ g solution} = 0.06334 \text{ Moles Ba} = 0.03167 \text{ Moles } \text{Y}_1\text{Ba}_2\text{Cu}_3 *$$

$$0.372 \text{ M Cu TFA} \times 255.42 \text{ g solution} = 0.09502 \text{ Moles Cu} = 0.03167 \text{ Moles } \text{Y}_1\text{Ba}_2\text{Cu}_3 *$$

* = if this is the limiting reagent. Analyzing the smallest quantity of the chemicals, Ba is the limiting reagent, although all of the values are very close. This is predicted due to the quantities mixed in the initial calculation. The amount of chemical required is therefore:

$$0.031672 \text{ Moles } \text{Y}_1\text{Ba}_2\text{Cu}_3 \times \frac{1 \text{ Mole Y}}{1 \text{ Mole } \text{Y}_1\text{Ba}_2\text{Cu}_3} \times \frac{1000 \text{ g}}{0.216 \text{ Moles Y}} = 146.63 \text{ g Y TFA}$$

$$0.031672 \text{ Moles } \text{Y}_1\text{Ba}_2\text{Cu}_3 \times \frac{2 \text{ Mole Ba}}{1 \text{ Mole } \text{Y}_1\text{Ba}_2\text{Cu}_3} \times \frac{1000 \text{ g}}{0.349 \text{ Moles Ba}} = 181.50 \text{ g Ba TFA}$$

$$0.031672 \text{ Moles } \text{Y}_1\text{Ba}_2\text{Cu}_3 \times \frac{3 \text{ Mole Cu}}{1 \text{ Mole } \text{Y}_1\text{Ba}_2\text{Cu}_3} \times \frac{1000 \text{ g}}{0.372 \text{ Moles Cu}} = 255.42 \text{ g Cu TFA}$$

After mixing the solution, the next step is to decide on the spin-casting variables to be used. The best performance came from the following procedure and variables:

1. A concentration of $\sim 0.25\text{M}$ of solution was used for spinning onto the substrates.
2. 10 layers are spun on the sample.
3. Multiple layers are separated by a hot-plate heating step to dry out the solvent. If this hot-plate step is omitted, subsequent layers tend to remove the previous layer due to the solvent present.

The firing schedule given below was developed by the author over a period of six months and approximately 50 samples. The samples ranged from no recognizable transition temperature, to a transition temperature of 90°K . There are many auxiliary data points that are not included, but the results are found indirectly in processes and procedures.

The spin-coated samples are then fired in the furnace for the following temperature and times:

1. Ramp the furnace with the sample up to 970°C .
2. Hold this temperature overnight.
3. Ramp down to 550°C .
4. Hold for 12 hours under flowing Oxygen

A preliminary test for the HTSCs to see how they will perform at liquid Nitrogen temperature is to measure the DC resistance across the sample at room temperature with a standard two-point resistance measurement. The samples from Oak Ridge both had resistances in the $1\ \Omega$ range, whereas the samples that the author processed had a range of $10\ \Omega$ to $1\ \text{M}\Omega$. The samples with the best superconducting transition tend to have a low room temperature resistance. This technique was used to ascertain the quality of the samples before the liquid nitrogen temperature test was performed.

The best samples for the sol-gel process yielded the results shown in the results section in Figures 30 and 31. The transition temperature is satisfactory for these samples, but

the overall quality of the samples is not adequate for devices. This is due to the “island” nature of the samples, or the tendency for the HTSC to grow in concentrated sections, thus creating open pockets down to the substrate. This is probably due to the method of formation for the HTSC. When the HTSC is fired to the highest temperature (~970°C), a large volume of material has left the sol-gel solution that was spun onto the surface originally, due to the high organic content in the sol-gel HTSC solution. This organic contribution evaporates from the substrate at the sample’s highest firing temperature, while the constituent HTSC elements, Y, Ba, and Cu remain on the substrate and are subsequently oxidized. This evaporation of organics results in a very small weight of HTSC remaining on the surface, thus forming the HTSC “islands.” To solve this problem, ramping the furnace at very small temperature increments, or starting with a more concentrated solution are possibilities that could yield better results. The author attempted these solutions with somewhat mixed results.

APPENDIX C: GRAVIMETRIC ANALYSIS

Gravimetric analysis refers to the analysis of a solution or chemical compound to determine the concentration of the chemical compound or solution. When a solution or compound has only known constituents, gravimetric analysis is the most effective. It is a technique used routinely by chemists both in academia and industry because it is fairly accurate and inexpensive. The required elements for performing a gravimetric analysis are an accurate balance with precision to 0.01g, a furnace capable of reaching temperatures of ~1000°C, and ceramic or platinum crucibles. Platinum crucibles are the best for this application, but due to the extreme cost of Platinum, standard glazed alumina crucibles may be used. Below will be a detailed description of a gravimetric analysis performed on a solution which was routinely performed on the sol-gel processing of the HTSC.

The first step in gravimetric analysis for analyzing a solution is to weigh the crucible. This will provide the baseline for all subsequent measurements. Next, add the solution to be analyzed into the crucible and weigh again. Note that the solution may have water, methanol, or any other liquid as the solvent. Gravimetric analysis works equally well on all solvents. At this point, an additional step would be to dry out all the solvents from the solution and weigh the crucible again. This yields the weight percent of solids in the solution which is commonly quoted for purchasing solutions.

After the solution is dried in the crucible, the solution must be fired at approximately ~1000°C to convert all the constituent chemicals to their oxide forms and to further dry out the solution. This is the key to gravimetric analysis. After a final weighing, the weight will give an accurate mole percent of the solution since all chemical complexes are then eliminated and the only remaining chemical is an oxide. The solvent does not have an oxide form and burns off, and the same is true for most chemical compounds such as acetates,

carbonates, nitrates, etc. There are some compounds that become complex at high temperatures, but these compounds are special cases and will not be discussed here.

Shown below is a sample calculation for Copper Trifluoroacetate that the author performed on the sol-gel superconductor experiment

Weight of crucible: 16.58 g

Weight of crucible + solution: 32.72 g

Weight of crucible + oxide: 17.39 g

Weight of oxide: 0.81 g

Weight of solution: 16.14 g

Calculation of the concentration of the solution:

$$0.81 \text{ g oxide} \times \frac{1 \text{ Mole Cu oxide}}{79.54 \text{ g Cu oxide}} \times \frac{1}{16.14 \text{ g solution}} \times \frac{1000 \text{ g}}{1 \text{ kg}} = 0.631 \frac{\text{M}}{\text{kg}}$$

Note that there are methods to improve the accuracy of this analysis. As stated previously, knowing the constituents of the solution will greatly aid the accuracy. Unknowns may be taken into account if they are given with the pure chemical (i.e.: 87% BaCO₃ will mean that 87% of the oxide measured will be BaO). Increasing the weight of the solution measured will add to the accuracy since the scale can measure a larger sample with a higher degree of precision.

APPENDIX D: ALUMINUM NITRIDE PROCESSING

The Aluminum Nitride deposition was deposited by means of DC Magnetron Reactive Sputtering. This technique is beneficial for the deposition of piezoelectrics due to the increased electric field adding to the alignment of the molecules. The drawback of DC Magnetron sputtering is that the deposition is not uniform and yields a change in resonant frequency across a three inch silicon wafer. Due to the small size of these HTSC samples, the change in resonant frequency should not be a factor.

The process of deposition will be outlined presently. In the system used by the Microelectronics Research Center, there is an Aluminum Target, a bias ring, and a substrate heater all in a high vacuum chamber with gas inlets. This is shown below in Figure 41.

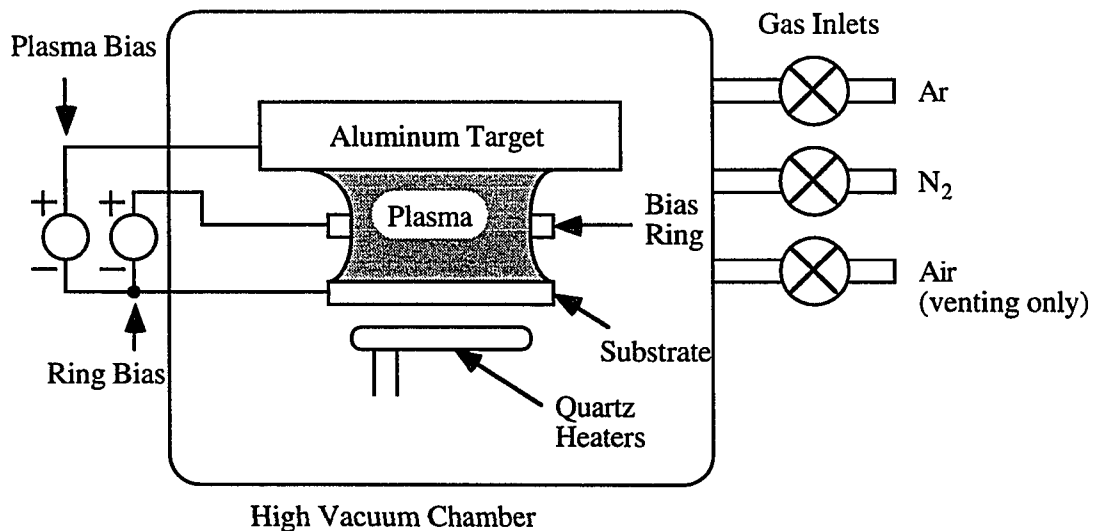


Figure 41: Schematic diagram of the DC Magnetron Reactive Sputtering system.

The process for the formation of Aluminum Nitride takes place in the Nitrogen plasma. When the Nitrogen plasma comes into contact with the Aluminum target,

Aluminum molecules are released from the surface and proceed toward the heated substrate. The AlN is formed on the surface of the substrate.

Due to the DC biasing inherent in this system and also because AlN is an insulator, charging occurs in the system and if nothing was done about it, there would be arcing in the chamber. To alleviate this problem, there is a patented procedure performed at the Microelectronics Research Center where Aluminum is deposited throughout the chamber to retain the potential difference necessary for the deposition of AlN. An Argon plasma is formed with the shutter closed above the substrate to prevent the deposition of an Aluminum layer on the substrate. This procedure sputters Aluminum throughout the chamber, and after 5 to 10 minutes, the AlN deposition may commence again. This Argon sputtering should be performed about every 30 minutes and with this process in place, thick layers of AlN may be produced with the thickest attempted being $\sim 15\mu\text{m}$.

APPENDIX E: PROGRAMS

The first program listed below was created to take the data from the four point probe measurement system developed by the author. It is written in Microsoft QuickBasic, and uses a National Instruments GPIB communication device.

```

REM BASIC HP Voltage Meter
REM Program
REM
REM Initialization from QB488Init.bas.
REM
LIBRARY "QuickBASIC4882.lib" 'open the library (should be in the System Folder).
ibsta%=0 : iberr%=0 : ibcnt&=0 'initialize the variables so the library can write to them.
CALL ibinit(ibsta%,iberr%,ibcnt&) 'tell the library what variables to write to.
REM
REM Set up the Break-out routine
REM
BREAK ON
ON BREAK GOSUB Quit
REM
REM Assign the HPIB address to DVM1%
REM for the first voltmeter
REM Voltage across sample
dvm1% = 23
dynam1$ = "vmeter1"
CALL ibfind (dynam1$,dvm1%)
REM
CALL ibclr (dvm1%)
REM
REM
REM Same thing for the second meter
REM Voltage across temp diode
dvm2% = 22
dynam2$ = "vmeter2"
CALL ibfind (dynam2$,dvm2%)
REM
REM
CALL ibclr (dvm2%)
REM
REM
REM Same thing for the third meter
REM Current of the sample
dvm3% = 24
dynam3$ = "vmeter3"
CALL ibfind (dynam3$,dvm3%)
REM

```

```

REM
CALL ibclr (dvm3%)
REM
REM
REM Start the measuring process
REM
REM
DIM tg(1000),r(1000),cur(1000),vol(1000)
wrt1$="F1;RA;N5;T1"
CALL IBWRT (dvm1%,wrt1$)
wrt2$="F1;R1"
CALL IBWRT (dvm2%,wrt2$)
wrt3$="F5;RA;N5;T1"
CALL IBWRT (dvm3%,wrt3$)
REM
REM
REM Take some data
REM
INPUT "Sample name:",sam$
INPUT "Ready?",rea$
REM
REM
rd1$=SPACE$(20)
rd2$=SPACE$(20)
rd3$=SPACE$(20)
a1=0:a2=0:b1=1:b2=2:n=1:verr=.02
OPEN sam$ FOR OUTPUT AS #1
PRINT #1, "Temperature (°K)", "Resistance (Ω)", "Voltage (V)", "Current (A)"
10 GOSUB datatake
IF ABS((a1-b1)/b1)>verr THEN 20
IF ABS((a2-b2)/b2)>verr THEN 20
GOTO 10
20 tg(n)=b1:r(n)=b2:cur(n)=xp2:vol(n)=xp1
SOUND 523,1
n=n+1:a1=b1:a2=b2
GOTO 10

datatake:
CALL ibrd (dvm1%,rd1$)
CALL ibrd (dvm2%,rd2$)
CALL ibrd (dvm3%,rd3$)
c1=VAL(rd2$):v=c1
GOSUB convtot
xp1=VAL(rd1$)
xp2=VAL(rd3$)
b2=xp1/xp2
PRINT t,b2,xp1,xp2
b1=t
RETURN

```

```

convtot:
t=0:icount=icount+1
IF icount=1 THEN DIM a(11),t1(11)
IF v < .999614 THEN
  vl=.079767:vu=.999614:CALL x1(vl,vu,v,x)
  a(0)=287.7564797#
  a(1)=-194.144823#
  a(2)=-3.837903
  a(3)=-1.318325
  a(4)=-.10912
  a(5)=-.393265
  a(6)=.146911
  a(7)=-.111192
  a(8)=.028877
  a(9)=-.029286
  a(10)=.015619
  t1(0)=1: t1(1)=x
  FOR ni=1 TO 9
    t1(ni+1)=2*x*t1(ni)-t1(ni-1)
  NEXT ni
  FOR n2=0 TO 10
    t=t+a(n2)*t1(n2)
  NEXT n2
ELSEIF v<1.13935 THEN
  vl=.923174:vu=1.13935:CALL x1(vl,vu,v,x)
  a(0)=71.81802500000001#
  a(1)=-53.799888#
  a(2)=1.669931
  a(3)=2.314228
  a(4)=1.566635
  a(5)=.723026
  a(6)=-.149503
  a(7)=.046876
  a(8)=-.0388555
  a(9)=.056889
  a(10)=-.116823
  a(11)=.05858
  t1(0)=1: t1(1)=x
  FOR ni=1 TO 10
    t1(ni+1)=2*x*t1(ni)-t1(ni-1)
  NEXT ni
  FOR n2=0 TO 11
    t=t+a(n2)*t1(n2)
  NEXT n2
ELSEIF v< 1.42013 THEN
  vl=1.11732:vu=1.42013:CALL x1(vl,vu,v,x)
  a(0)=17.304227#
  a(1)=-7.894688
  a(2)=.453442
  a(3)=-.002243
  a(4)=.158036

```

```

a(5)=-.193093
a(6)=.155717
a(7)=-.85185
a(8)=.07855
a(9)=-.018312
a(10)=.039255
t1(0)=1: t1(1)=x
FOR ni=1 TO 9
t1(ni+1)=2*x*t1(ni)-t1(ni-1)
NEXT ni
FOR n2=0 TO 10
t=t+a(n2)*t1(n2)
NEXT n2
ELSE
vl=1.32412:vu=1.69812:CALL x1(vl,vu,v,x)
a(0)=7.556358
a(1)=-5.917261
a(2)=.237238
a(3)=-.334636
a(4)=-.058642
a(5)=-.019929
a(6)=-.020715
a(7)=-.014814
a(8)=-.008789
a(9)=-.008554
t1(0)=1: t1(1)=x
FOR ni=1 TO 8
t1(ni+1)=2*x*t1(ni)-t1(ni-1)
NEXT ni
FOR n2=0 TO 9
t=t+a(n2)*t1(n2)
NEXT n2
END IF
RETURN

SUB x1(vl,vu,v,x) STATIC
x=((v-vl)-(vu-v))/(vu-vl)
END SUB

Quit:
FOR l=1 TO n-1
PRINT #1, tg(l),r(l),vol(l),cur(l)
NEXT l
CLOSE #1
REM CALL ibclr (dvm1%):CALL ibclr (dvm2%):CALL ibclr (dvm3%)
LIBRARY CLOSE
STOP

```

This FORTRAN program was simulated on Iowa State University's Project Vincent system. The program invokes matrix inversion subroutines found in the NAG locker, along with vector graphing subroutines found in the NCAR locker.

```

program scmatrix
C
C Superconducting Microwave Analysis
C using a modified Transmission Line Approach
C
C This program will simulate both an acoustic circuit
C along with an electrical circuit.
C
C Modified for the Augmented array analysis on 7/1/94
C
C Initialize Constants and Arrays
C
integer i,j,k,l,num,icap,ipiv(101475),n
double complex x(500,500),z(500,500),y,r,ap,a(101475)
double complex yls,zrn,zln,pi,fr,y2,r2,c2,kon,uo,zt,one1
double complex one,two,three,four,dx,alpha,rho,two1
real u(12,24),v(12,24),w(12,24),x2(12,24)
double precision work(101475),dcabs,cur(500,500),pot(500,500)
character uplo
C Set the matrix elements and define the size
C of the matrix
C
num=10
C num=# of unit cells
C
C Other constants
C
C Array constant used in calculations
icap=num*(num+1)
n=icap*2
one1=(1.0d0,0.0d0)
two1=(0.0d0,2.0d0)
one=(-1.0d0,0.0d0)
two=(2.0d0,0.0d0)
three=(3.0d0,0.0d0)
four=(4.0d0,0.0d0)
C
C kon=% of superconducting to non-sc (0<=kon<=1)
C
kon=(5.0d-1,0.0d0)
C
C New Values!!!
C dx=.1um, dy=.1um, dz1=.1um, dz2=5um

```

```

C
dx=(2.0d-5,0.0d0)
C dz2=(5.6d-7,0.0d0)
pi=(3.14159265359d0,0.0d0)
fr=(1.0d9,0.0d0)
uo=four*pi*(1.d-7,0.0d0)
alpha=one1/(9.25d-8,0.0d0)
rho=(4d-6,0.0d0)
C
C
C ap=(2.5d-10,1.119381d-9): Leaky, added 8/11/94
C ap=(2.5d-10,9.5d-11)*dx*dx*two*pi*fr/dz2
C ap=(0.0d0,9.5d-11)*dx*dx*two*pi*fr/dz2
C e=9.5e-11, c=(e*dx*dy)/dz2
C
C From the Libra Calculation:
C ap=(1.3d-7,2.9d-7)
C ap=(7.0757d-4,7.114d-5)
C
C r=eta*dx/dy
C r=one1/(3.76734d2,0.0d0)
C
C y=yl(sc)+1/(zl(nsc)//zr(nsc))
C yls=1/(2*pi*fr*uo*dx/alpha^2*kon*dy*dz)
C zln=2*pi*fr*uo*dx/alpha^2*(1-kon)*dy*dz
C zrn=rho*dx/(1-kon)*dy*dz
zln=two1*pi*fr*uo/(alpha*alpha*(one1-kon)*dx)
zrn=rho/((one1-kon)*dx)
yls=one1/(two1*pi*fr*uo/(alpha*alpha*kon*dx))
zt=zln+zrn
y=(one1/zt)+yls
write (*,*) zln,zrn,yls,zt,(one1/zt),y
C y1=1.5d6-j4.2d17/f, y=y1*dy*dx/dz1
C taken from RW&VD.
C y=(1.0d0,0.0d0)
C ap=(1.0d0,0.0d0)
C r=(1.0d0,0.0d0)
y2=one*y
r2=one*r
c2=one*ap
C
C Clear the arrays
C
C do 1 i=1,n,1
  do 2 j=1,n,1
    x(i,j)=(0.0d0,0.0d0)
    z(i,j)=(0.0d0,0.0d0)
  2 continue
1 continue
n=n-1
C n=n-1 is for the augmented array analysis.

```

```

C
C Initialize the array for a num x num cell
C superconducting lattice
C Redone, 7/17/94 with lots of comments
C
C k=augmented analysis constant
k=num*(num+1)-1
C
do 3 i=1,num,1
  l=k+i
  if (i.eq.1) then
C
C First Column, Top and Bottom
C Augmented matrix taken into account
C
    x(i+1,i)=y2
    x(i,i+1)=y2
    x(i,i)=two*y
    do 4 j=1,num-1,1
C Matching term
      x(j*num+i,j*num+i)=three*y
      x(l+j*num,l+j*num)=three*y
C # 11-12
      x(j*num+i,j*num+i+1)=y2
      x(j*num+i+1,j*num+i)=y2
      x(j*num+1,j*num+1+1)=y2
      x(j*num+1+1,j*num+1)=y2
C Special for the bottom part:
      if (j.ne.1) then
        x((j-1)*num+1,j*num+1)=y2
        x(j*num+1,(j-1)*num+1)=y2
      endif
C # 1-11
      x((j-1)*num+i,j*num+i)=y2
      x(j*num+i,(j-1)*num+i)=y2
4 continue
C # 91-101
      x((num-1)*num+i,num*num+i)=y2
      x(num*num+i,(num-1)*num+i)=y2
      x((num-1)*num+1,num*num+1)=y2
      x(num*num+1,(num-1)*num+1)=y2
C # 101-102
      x(num*num+i,num*num+i+1)=r2
      x(num*num+i+1,num*num+i)=r2
      x(num*num+1,num*num+1+1)=r2
      x(num*num+1+1,num*num+1)=r2
C Matching term
      x(num*num+i,num*num+i)=r+y
      x(num*num+1,num*num+1)=r+y
    else
      if (i.eq.num) then

```

C
 C Last Column, Top and Bottom
 C
 $x(i,i)=ap+two*y$
 $x(l,l)=ap+two*y$
 C Capacitor
 C
 C Changed on 8/3/94 adding a resistor...
 C
 $x(l,i)=c2$
 $x(i,l)=c2$
 do 5 j=1,num-1,1
 C # 10-20
 $x((j-1)*num+i,j*num+i)=y2$
 $x(j*num+i,(j-1)*num+i)=y2$
 $x((j-1)*num+l,j*num+l)=y2$
 $x(j*num+l,(j-1)*num+l)=y2$
 C Matching term
 $x(j*num+i,j*num+i)=three*y$
 $x(j*num+l,j*num+l)=three*y$
 5 continue
 C # 100-110
 $x((num-1)*num+i,num*num+i)=y2$
 $x(num*num+i,(num-1)*num+i)=y2$
 $x((num-1)*num+l,num*num+l)=y2$
 $x(num*num+l,(num-1)*num+l)=y2$
 C Matching term
 $x(num*num+i,num*num+i)=r+y$
 $x(num*num+l,num*num+l)=r+y$
 else
 C
 C Middle of the Matrix
 C
 $x(i,i)=three*y+ap$
 $x(l,l)=three*y+ap$
 C # 2-3
 $x(i+1,i)=y2$
 $x(i,i+1)=y2$
 $x(l+1,l)=y2$
 $x(l,l+1)=y2$
 C Capacitor
 $x(i+k,i)=c2$
 $x(i,i+k)=c2$
 do 6 j=1,num-1,1
 C Matching term
 $x(j*num+i,j*num+i)=four*y$
 $x(j*num+l,j*num+l)=four*y$
 C # 12-13
 $x(j*num+i,j*num+i+1)=y2$
 $x(j*num+i+1,j*num+i)=y2$
 $x(j*num+l,j*num+l+1)=y2$

```

      x(j*num+1+1,j*num+1)=y2
C # 12-2
      x((j-1)*num+i,j*num+i)=y2
      x(j*num+i,(j-1)*num+i)=y2
      x((j-1)*num+1,j*num+1)=y2
      x(j*num+1,(j-1)*num+1)=y2
6   continue
C # 92-102
      x((num-1)*num+i,num*num+i)=y2
      x(num*num+i,(num-1)*num+i)=y2
      x((num-1)*num+1,num*num+1)=y2
      x(num*num+1,(num-1)*num+1)=y2
C # 102-103
      x(num*num+i,num*num+i+1)=r2
      x(num*num+i+1,num*num+i)=r2
      x(num*num+1,num*num+1+1)=r2
      x(num*num+1+1,num*num+1)=r2
C Matching term
      x(num*num+i,num*num+i)=two*r+y
      x(num*num+1,num*num+1)=two*r+y
endif
endif
3   continue
C
C   Check if it's workin'
C
C   open (unit=1000,file='out1',status='new')
C   do 21 i=1,icap*2-1
C     write (1000,*) i
C     do 20 j=1,icap*2-1
C       if (dcabs(x(i,j)).ne.0.0d0) then
C         write (1000,*) j, x(i,j)
C       endif
C 20  continue
C 21  continue
C     close (unit=1000)
C
C   Now that the matrix is set up, invert
C   the matrix to get the z-matrix for this problem
C
do 53 i=1,n,1
  do 54 j=1,n,1
    a(i+(2*n-j)*(j-1)/2)=x(i,j)
54  continue
53  continue
uplo='l'
C
call inv2 (a,n,work,ipiv,uplo)
C
C   do 55 i=1,n,1
C     x(i,1)=a(i)

```

```

C 55 continue
C
C Now, translate this result back into a matrix
C that can be analyzed
C
C call bout(a,num,icap,z)
C
C Fix x for the augmented matrix analysis
C
C call xout(x,icap)
C
C Calculate the currents for the matrix
C
C call curr (x,cur,z,num,icap,u,v)
C
C Calculate the electric field
C
C call pote (pot,z,num,dx,w,x2)
C
C
C Save the matrix into something close to usable...
C
C
C
C open (unit=1001,file='out2',status='new')
open (unit=1002,file='out3',status='new')
open (unit=1003,file='out4',status='new')
open (unit=1004,file='out5',status='new')
do 200 k=2,4,1
  write (1000+k,*) ' y=',y
  write (1000+k,*) ' c=',ap
  write (1000+k,*) ' r=',r
200 continue
do 100 i=1,num,1
C   write (1001,102) i
  write (1002,102) i
  write (1003,102) i
  write (1004,102) i
  do 101 j=num+1,1,-1
C   write (1001,*) j,u(i,j),v(i,j)
    write (1002,*) j,dcabs(z(i,j))
    write (1003,*) j,cur(i,j)
    write (1004,*) j,pot(i,j)
101 continue
100 continue
do 103 i=num+1,2*num,1
C   write (1001,102) i
  write (1002,102) i
  write (1003,102) i
  write (1004,102) i
  do 104 j=1,num+1,1
C   write (1001,*) j,u(i,j),v(i,j)

```

```

        write (1002,*) j,dcabs(z(i,j))
        write (1003,*) j,cur(i,j)
        write (1004,*) j,pot(i,j)
104  continue
103  continue
102  format (' i=',i2)
C   close (unit=1001)
    close (unit=1002)
    close (unit=1003)
    close (unit=1004)
C
C   Make a flow-field plot
C
call pplot (u,v,w,x2)
C
C
C
    stop
    end
C
C   Subroutine dcabs
C
function dcabs(x)
double complex x
double precision dcabs
dcabs=dsqrt(dreal(dconjg(x)*x))
return
end
C
C   Subroutine dcabs2
C
function dcabs2(x,y)
double complex x,y,dum
double precision dcabs2
dum=dconjg(x)*x+dconjg(y)*y
dcabs2=dsqrt(dreal(dum))
return
end
C
C   Subroutine abb
C
function abb(x)
double complex x,dum
real abb,a1
if (real(x).gt.0.d+0) then
    a1=-1.
else
    a1=1.
endif
dum=dconjg(x)*x
abb=a1*sngl(dsqrt(dreal(dum)))

```

```

return
end
C
C Subroutine valu(lo,hi)
C
function valu (lo,hi)
real lo,hi,valu
if (lo.gt.hi) then
valu=-1.*(lo-hi)
else
valu=hi-lo
endif
return
end
C
C
C
C subroutine inv2 (ap,n,work,ipiv,uplo)
C
C This subroutine uses the 'canned' subroutines
C available with NAG Mark 15 library and in
C specific, uses the F07QWF program.
C
C This will find the inverse of a given complex
C matrix.
C
external f07qwf,f07qrf
double complex ap(101475)
double precision work(101475)
character uplo
integer n,ipiv(101475),info
info=0
C
C Factorize a:
C
call f07qrf (uplo,n,ap,ipiv,info)
write (*,*) info,uplo
if (info.eq.0) then
C
C Compute the inverse of a:
C
call f07qwf (uplo,n,ap,ipiv,work,info)
C
C Output the inverse
C
else
write (*,*) 'singular'
endif
return
end
C

```

```

C
C
C  subroutine bout(a,num,icap,z)
C
C  This subroutine converts the inverted matrix
C  into a matrix that can be easily analyzed
C
C  integer i,j,icap,num,q,p,r
C  double complex a(101475),z(500,500)
C
C  Calculate some useful constants
C
C  Fix for the augmented matrix
C
C  do 4 i=2*icap-1,icap+1,-1
C    a(i+1)=a(i)
C  4  continue
C    a(icap+1)=(0.0d0,0.0d0)
C
C  Move the solution into the first column
C
C  do 1 i=2,2*icap,1
C    a(i)=a(i)/a(1)
C  1  continue
C    a(1)=(1.0d0,0.0d0)
C
C  Move the solution into the matrix:
C
C  do 2 i=1,2*num,1
C    if (i.gt.num) then
C      p=i-num
C      r=icap
C    else
C      p=i
C      r=0
C    endif
C    do 3 j=1,num+1
C      q=(j-1)*num
C      z(i,j)=a(p+q+r)
C  3  continue
C  2  continue
C
C  Return to main program
C
C  return
C  end
C
C
C  Subroutine curr (x,cur,z,num,icap)
C
C  This calculates the currents when given

```

C the potentials (z) and the admittances (x)
 C
 subroutine curr (x,c,z,num,icap,u,q)
 C
 double complex x(500,500),z(500,500),v,v2
 double precision dcabs,c(500,500)
 real u(12,24),q(12,24),q1,q2
 integer num,icap,i,j,k,l,m
 C
 C Multiply the numbers out
 C
 do 11 i=1,num,1
 l=icap+i
 m=num+i
 C This takes care of the bottom part of the
 C matrix
 if (i.eq.1) then
 C First column
 C Bottom value #1
 v=z(1,1)-z(1,2)
 c(1,1)=dcabs(x(1,num+1)*v)
 q1=abb(x(1,num+1)*v)
 q(2,num+3)=valu(0.,q1)
 v=z(1,1)-z(2,1)
 c(1,1)=c(1,1)+dcabs(x(1,2)*v)
 q1=abb(x(1,2)*v)
 u(2,num+3)=valu(0.,q1)
 C (Bottom half of the matrix)
 v=z(m,1)-z(m,2)
 c(m,1)=dcabs(x(1,num+1)*v)
 q1=abb(x(1,num+1)*v)
 q(2,num+2)=valu(q1,0.)
 v=z(m,1)-z(m+1,1)
 c(m,1)=c(m,1)+dcabs(x(1,l+1)*v)
 q1=abb(x(1,l+1)*v)
 u(2,num+2)=valu(0.,q1)
 C Top Value #101
 v=z(1,num+1)-z(2,num+1)
 v2=x(num*num+1,num*num+2)*v
 c(1,num+1)=dcabs(v2)
 q1=abb(v2)
 u(2,2*(num+1)+1)=valu(0.,q1)
 v=z(1,num+1)-z(1,num)
 v2=x(num*num+1,num*(num-1)+1)*v
 c(1,num+1)=c(1,num+1)+dcabs(v2)
 q1=abb(v2)
 q(2,2*(num+1)+1)=valu(q1,0.)
 C (Bottom half of the matrix)
 v=z(m,num+1)-z(m+1,num+1)
 v2=x(num*num+1,num*num+1+1)*v
 c(m,num+1)=dcabs(v2)

```

q1=abb(v2)
u(2,2)=valu(0.,q1)
v=z(m,num+1)-z(m,num)
v2=x(num*num+1,num*(num-1)+1)*v
c(m,num+1)=c(m,num+1)+dcabs(v2)
q1=abb(v2)
q(2,2)=valu(0.,q1)
C Middle Values #11-91
do 12 j=1,num-1,1
  k=j*num
  v=z(1,j+1)-z(1,j+2)
  c(1,j+1)=dcabs(x(k+1,k+num+1)*v)
  q1=abb(x(k+1,k+num+1)*v)
  v2=z(1,j+1)-z(1,j)
  c(1,j+1)=c(1,j+1)+dcabs(x(k+1,k-num+1)*v2)
  q2=abb(x(k+1,k-num+1)*v2)
  q(2,num+3+j)=valu(q2,q1)
  v=z(1,j+1)-z(2,j+1)
  c(1,j+1)=c(1,j+1)+dcabs(x(k+1,k+2)*v)
  q1=abb(x(k+1,k+2)*v)
  u(2,num+3+j)=valu(0.,q1)
C (Bottom half of the matrix)
v=z(m,j+1)-z(m,j+2)
c(m,j+1)=dcabs(x(k+1,k+num+1)*v)
q1=abb(x(k+1,k+num+1)*v)
v2=z(m,j+1)-z(m,j)
c(m,j+1)=c(m,j+1)+dcabs(x(k+1,k-num+1)*v2)
q2=abb(x(k+1,k-num+1)*v2)
q(2,num+2-j)=valu(q1,q2)
v=z(m,j+1)-z(m+1,j+1)
c(m,j+1)=c(m,j+1)+dcabs(x(k+1,k+1+1)*v)
q1=abb(x(k+1,k+1+1)*v)
u(2,num+2-j)=valu(0.,q1)
12 continue
else
  if (i.eq.num) then
C Last Column
C Bottom Value #10
v2=z(i,1)-z(i+num,1)
c(i,1)=dcabs(x(i,1)*v2)
q1=abb(x(i,1)*v2)
v=z(i,1)-z(i-1,1)
c(i,1)=c(i,1)+dcabs(x(i,num-1)*v)
q2=abb(x(i,num-1)*v)
u(num+1,num+3)=valu(q2,0.)
v=z(i,1)-z(i,2)
c(i,1)=c(i,1)+dcabs(x(i,num+i)*v)
q2=abb(x(i,num+i)*v)
q(num+1,num+3)=valu(q1,q2)
C (Bottom half of the matrix)
v2=z(m,1)-z(m-num,1)

```

```

c(m,1)=dcabs(x(l,i)*v2)
q1=abb(x(l,i)*v2)
v=z(m,1)-z(m-1,1)
c(m,1)=c(m,1)+dcabs(x(l,l-1)*v)
q2=abb(x(l,l-1)*v)
u(num+1,num+2)=valu(q2,0.)
v=z(m,1)-z(m,2)
c(m,1)=c(m,1)+dcabs(x(l,num+1)*v)
q2=abb(x(l,num+1)*v)
q(num+1,num+2)=valu(q2,q1)
C Top Value #110
v=z(i,num+1)-z(i-1,num+1)
v2=x(num*(num+1),num*(num+1)-1)*v
c(i,num+1)=dcabs(v2)
q1=abb(v2)
u(num+1,2*(num+1)+1)=valu(q1,0.)
v=z(i,num+1)-z(i,num)
v2=x(num*(num+1),num*num)*v
c(i,num+1)=c(i,num+1)+dcabs(v2)
q1=abb(v2)
q(num+1,2*(num+1)+1)=valu(q1,0.)
C (Bottom half of the matrix)
v=z(m,num+1)-z(m-1,num+1)
v2=x(num*(num+1)+icap,num*(num+1)-1+icap)*v
c(m,num+1)=dcabs(v2)
q1=abb(v2)
u(num+1,2)=valu(q1,0.)
v=z(m,num+1)-z(m,num)
v2=x(num*(num+1)+icap,num*num+icap)*v
c(m,num+1)=c(m,num+1)+dcabs(v2)
q1=abb(v2)
q(num+1,2)=valu(0.,q1)
C Middle Values #20-100
do 13 j=1,num-1,1
k=j*num
v2=z(i,j+1)-z(i,j+2)
c(i,j+1)=dcabs(x(k+i,k+num+i)*v2)
v=z(i,j+1)-z(i,j)
c(i,j+1)=c(i,j+1)+dcabs(x(k+i,k-num+i)*v)
q1=abb(x(k+i,k+num+i)*v2)
q2=abb(x(k+i,k-num+i)*v)
q(num+1,num+3+j)=valu(q2,q1)
v=z(i,j+1)-z(i-1,j+1)
c(i,j+1)=c(i,j+1)+dcabs(x(k+i,k+i-1)*v)
q1=abb(x(k+i,k+i-1)*v)
u(num+1,num+3+j)=valu(q1,0.)
C (Bottom half of the matrix)
v2=z(m,j+1)-z(m,j+2)
c(m,j+1)=dcabs(x(k+1,k+num+1)*v2)
v=z(m,j+1)-z(m,j)
c(m,j+1)=c(m,j+1)+dcabs(x(k+1,k-num+1)*v)

```

```

    q1=abb(x(k+1,k+num+1)*v2)
    q2=abb(x(k+1,k-num+1)*v)
    q(num+1,num+2-j)=valu(q2,q1)
    v=z(m,j+1)-z(m-1,j+1)
    c(m,j+1)=c(m,j+1)+dcabs(x(k+1,k+1-1)*v)
    q1=abb(x(k+1,k+1-1)*v)
    u(num+1,num+2-j)=valu(q1,0.)
13    continue
    else
C    The inside of the matrix
C    Bottom Values
    v2=z(i,1)-z(i+num,1)
    c(i,1)=dcabs(x(i,1)*v2)
    v=z(i,1)-z(i+1,1)
    c(i,1)=c(i,1)+dcabs(x(i,i+1)*v)
    q1=abb(x(i,i+1)*v)
    v=z(i,1)-z(i-1,1)
    c(i,1)=c(i,1)+dcabs(x(i,i-1)*v)
    q2=abb(x(i,i-1)*v)
    u(i+1,num+3)=valu(q2,q1)
    v=z(i,1)-z(i,2)
    c(i,1)=c(i,1)+dcabs(x(i,num+i)*v)
    q1=abb(x(i,num+i)*v)
    q2=abb(x(i,1)*v2)
    q(i+1,num+3)=valu(q2,q1)
C    (Bottom half of the matrix)
    v2=z(m,1)-z(m-num,1)
    c(m,1)=dcabs(x(1,i)*v2)
    v=z(m,1)-z(m+1,1)
    c(m,1)=c(m,1)+dcabs(x(1,l+1)*v)
    q1=abb(x(1,l+1)*v)
    v=z(m,1)-z(m-1,1)
    c(m,1)=c(m,1)+dcabs(x(1,l-1)*v)
    q2=abb(x(1,l-1)*v)
    u(i+1,num+2)=valu(q2,q1)
    v=z(m,1)-z(m,2)
    c(m,1)=c(m,1)+dcabs(x(1,num+1)*v)
    q1=abb(x(1,i)*v2)
    q2=abb(x(1,num+1)*v)
    q(i+1,num+2)=valu(q2,q1)
C    Top Values
    v=z(i,num+1)-z(i-1,num+1)
    v2=x(num*num+i,num*num+i-1)*v
    c(i,num+1)=dcabs(v2)
    q1=abb(v2)
    v=z(i,num+1)-z(i+1,num+1)
    v2=x(num*num+i,num*num+i+1)*v
    c(i,num+1)=c(i,num+1)+dcabs(v2)
    q2=abb(v2)
    u(i+1,2*(num+1)+1)=valu(q1,q2)
    v=z(i,num+1)-z(i,num)

```

```

v2=x(num*num+i,num*(num-1)+i)*v
c(i,num+1)=c(i,num+1)+dcabs(v2)
q1=abb(v2)
q(i+1,2*(num+1)+1)=valu(q1,0.)
C (Bottom half of the matrix)
v=z(m,num+1)-z(m-1,num+1)
v2=x(num*num+1,num*num+1-1)*v
c(m,num+1)=dcabs(v2)
q1=abb(v2)
v=z(m,num+1)-z(m+1,num+1)
v2=x(num*num+1,num*num+1+1)*v
c(m,num+1)=c(m,num+1)+dcabs(v2)
q2=abb(v2)
u(i+1,2)=valu(q1,q2)
v=z(m,num+1)-z(m,num)
v2=x(num*num+1,num*(num-1)+1)*v
c(m,num+1)=c(m,num+1)+dcabs(v2)
q1=abb(v2)
q(i+1,2)=valu(0.,q1)
C Middle Values
do 15 j=1,num-1,1
  k=j*num
  v=z(i,j+1)-z(i+1,j+1)
  c(i,j+1)=dcabs(x(k+i,k+i+1)*v)
  q1=abb(x(k+i,k+i+1)*v)
  v=z(i,j+1)-z(i-1,j+1)
  c(i,j+1)=c(i,j+1)+dcabs(x(k+i,k+i-1)*v)
  q2=abb(x(k+i,k+i-1)*v)
  u(i+1,num+3+j)=valu(q2,q1)
  v=z(i,j+1)-z(i,j+2)
  c(i,j+1)=c(i,j+1)+dcabs(x(k+i,k+num+i)*v)
  q1=abb(x(k+i,k+num+i)*v)
  v=z(i,j+1)-z(i,j)
  c(i,j+1)=c(i,j+1)+dcabs(x(k+i,k-num+i)*v)
  q2=abb(x(k+i,k-num+i)*v)
  q(i+1,num+3+j)=valu(q2,q1)
C (Bottom half of the matrix)
v=z(m,j+1)-z(m+1,j+1)
c(m,j+1)=dcabs(x(k+1,k+1+1)*v)
q1=abb(x(k+1,k+1+1)*v)
v=z(m,j+1)-z(m-1,j+1)
c(m,j+1)=c(m,j+1)+dcabs(x(k+1,k+1-1)*v)
q2=abb(x(k+1,k+1-1)*v)
u(i+1,num+2-j)=valu(q2,q1)
v=z(m,j+1)-z(m,j+2)
c(m,j+1)=c(m,j+1)+dcabs(x(k+1,k+num+1)*v)
q1=abb(x(k+1,k+num+1)*v)
v=z(m,j+1)-z(m,j)
c(m,j+1)=c(m,j+1)+dcabs(x(k+1,k-num+1)*v)
q2=abb(x(k+1,k-num+1)*v)
q(i+1,num+2-j)=valu(q1,q2)

```

```

15     continue
      endif
      endif
11 continue
C
C   Put in the 0's around the border
C
do 20 i=1,num+2,1
  u(i,1)=0.
  q(i,1)=0.
  u(i,2*(num+2))=0.
  q(i,2*(num+2))=0.
20 continue
do 21 i=1,2*(num+2),1
  u(1,j)=0.
  q(1,j)=0.
  u(num+2,j)=0.
  q(num+2,j)=0.
21 continue
C
C   Return to main program
C
return
end

C
C   Subroutine pot(c,z,num,dx)
C
C   Calculates the electric field of the matrix
C   and gives the output as a real number
C
subroutine pote (c,z,num,dx,u,v)
C
double complex z(500,500),v1,v2,dx
double precision dcabs,dcabs2,c(500,500)
real u(12,24),v(12,24),q1,q2,valu
integer num,i,j,m
C
C   Multiply the numbers out
C
do 1 i=1,num,1
  m=num+i
C
C   First Column
C
  if (i.eq.1) then
    do 4 j=1,num+1,1
C
C   Bottom Row
C
      if (j.eq.1) then
        v1=z(i+1,j)-z(i,j)

```

```

v2=z(i,j+1)-z(i,j)
c(i,j)=dcabs2(v1/dx,v2/dx)
q1=abb(-v1/dx)
u(2,num+3)=valu(0.,q1)
q1=abb(-v2/dx)
q2=abb((z(i,j)-z(m,j))/dx)
v(2,num+3)=valu(q2,q1)
C Bottom half
v1=z(m+1,j)-z(m,j)
v2=z(m,j+1)-z(m,j)
c(m,j)=dcabs2(v1/dx,v2/dx)
q1=abb(-v1/dx)
u(2,num+2)=valu(0.,q1)
q1=abb(-v2/dx)
q2=abb((z(m,j)-z(i,j))/dx)
v(2,num+2)=valu(q1,q2)
else
C
C Top Row
C
if (j.eq.num+1) then
v1=z(i+1,j)-z(i,j)
c(i,j)=dcabs(v1/dx)
q1=abb(-v1/dx)
u(2,2*(num+1)+1)=valu(0.,q1)
q2=abb((z(i,j)-z(i,j-1))/dx)
v(2,2*(num+1)+1)=valu(q2,0.)
C Bottom half
v1=z(m+1,j)-z(m,j)
c(m,j)=dcabs(v1/dx)
q1=abb(-v1/dx)
u(2,2)=valu(0.,q1)
q2=abb((z(m,j)-z(m,j-1))/dx)
v(2,2)=valu(0.,q2)
else
C
C Rest of column
C
v1=z(i+1,j)-z(i,j)
v2=z(i,j+1)-z(i,j)
c(i,j)=dcabs2(v1/dx,v2/dx)
q1=abb(-v1/dx)
u(2,num+2+j)=valu(0.,q1)
q1=abb(-v2/dx)
q2=abb((z(i,j)-z(i,j-1))/dx)
v(2,num+2+j)=valu(q2,q1)
C Bottom half
v1=z(m+1,j)-z(m,j)
v2=z(m,j+1)-z(m,j)
c(m,j)=dcabs2(v1/dx,v2/dx)
q1=abb(-v1/dx)

```

```

        u(2,num+3-j)=valu(0.,q1)
        q1=abb(-v2/dx)
        q2=abb((z(m,j)-z(m,j-1))/dx)
        v(2,num+3-j)=valu(q1,q2)
    endif
endif
4    continue
    else
C
C    Last Column
C
        if (i.eq.num) then
            do 5 j=1,num+1,1
C
C    First row
C
                if (j.eq.1) then
                    v1=z(i,j+1)-z(i,j)
                    c(i,j)=dcabs(v1/dx)
                    q1=abb(-v1/dx)
                    q2=abb((z(i,j)-z(m,j))/dx)
                    v(num+1,num+3)=valu(q2,q1)
                    q1=abb((z(i,j)-z(i-1,j))/dx)
                    u(num+1,num+3)=valu(q1,0.)
C    Bottom Half
                    v1=z(m,j+1)-z(m,j)
                    c(m,j)=dcabs(v1/dx)
                    q1=abb(-v1/dx)
                    q2=abb((z(m,j)-z(i,j))/dx)
                    v(num+1,num+2)=valu(q1,q2)
                    q1=abb((z(m,j)-z(m,j-1))/dx)
                    u(num+1,num+2)=valu(q1,0.)
                else
C
C    Top row
C
                    if (j.eq.num+1) then
                        c(i,num+1)=0.0d0
                        q1=abb((z(i,j)-z(i,j-1))/dx)
                        v(num+1,2*(num+1)+1)=valu(q1,0.)
                        q1=abb((z(i,j)-z(i-1,j))/dx)
                        u(num+1,2*(num+1)+1)=valu(q1,0.)
C    Bottom Half
                        c(m,num+1)=0.0d0
                        q1=abb((z(m,j)-z(m,j-1))/dx)
                        v(num+1,2)=valu(0.,q1)
                        q1=abb((z(m,j)-z(m-1,j))/dx)
                        u(num+1,2)=valu(q1,0.)
                    else
C
C    Rest of the Column

```

```

C
    v1=z(i,j+1)-z(i,j)
    c(i,j)=dcabs(v1/dx)
    q1=abb(-v1/dx)
    q2=abb((z(i,j)-z(i,j-1))/dx)
    v(num+1,num+2+j)=valu(q2,q1)
    q1=abb((z(i,j)-z(i-1,j))/dx)
    u(num+1,num+2+j)=valu(q1,0.)
C Bottom Half
    v1=z(m,j+1)-z(m,j)
    c(m,j)=dcabs(v1/dx)
    q1=abb(-v1/dx)
    q2=abb((z(m,j)-z(m,j-1))/dx)
    v(num+1,num+3-j)=valu(q2,q1)
    q1=abb((z(m,j)-z(m-1,j))/dx)
    u(num+1,num+3-j)=valu(q1,0.)
    endif
    endif
5 continue
else
C
C Middle Section
C
    do 6 j=1,num+1,1
C
C Bottom Row
C
    if (j.eq.1) then
        v1=z(i+1,j)-z(i,j)
        v2=z(i,j+1)-z(i,j)
        c(i,j)=dcabs2(v1/dx,v2/dx)
        q1=abb(-v1/dx)
        q2=abb((z(i,j)-z(i-1,j))/dx)
        u(1+i,num+3)=valu(q2,q1)
        q1=abb(-v2/dx)
        q2=abb((z(i,j)-z(m,j))/dx)
        v(1+i,num+3)=valu(q2,q1)
C Bottom Half
        v1=z(m+1,j)-z(m,j)
        v2=z(m,j+1)-z(m,j)
        c(m,j)=dcabs2(v1/dx,v2/dx)
        q1=abb(-v1/dx)
        q2=abb((z(m,j)-z(m-1,j))/dx)
        u(i+1,num+2)=valu(q2,q1)
        q1=abb(-v2/dx)
        q2=abb((z(m,j)-z(i,j))/dx)
        v(i+1,num+2)=valu(q1,q2)
    else
C
C Top Row
C

```

```

        if (j.eq.num+1) then
            v1=z(i+1,j)-z(i,j)
            c(i,j)=dcabs(v1/dx)
            q1=abb(-v1/dx)
            q2=abb((z(i,j)-z(i-1,j))/dx)
            u(i+1,2*(num+1)+1)=valu(q2,q1)
            q1=abb((z(i,j)-z(i,j-1))/dx)
            v(i+1,2*(num+1)+1)=valu(q1,0.)
C    Bottom Half
            v1=z(m+1,j)-z(m,j)
            c(m,j)=dcabs(v1/dx)
            q1=abb(-v1/dx)
            q2=abb((z(m,j)-z(m-1,j))/dx)
            u(i+1,2)=valu(q2,q1)
            q1=abb((z(m,j)-z(m,j-1))/dx)
            v(i+1,2)=valu(0.,q1)
        else
C
C    Bulk of the matrix
C
            v1=z(i+1,j)-z(i,j)
            v2=z(i,j+1)-z(i,j)
            c(i,j)=dcabs2(v1/dx,v2/dx)
            q1=abb(-v1/dx)
            q2=abb((z(i,j)-z(i-1,j))/dx)
            u(i+1,num+2+j)=valu(q2,q1)
            q1=abb(-v2/dx)
            q2=abb((z(i,j)-z(i,j-1))/dx)
            v(i+1,num+2+j)=valu(q2,q1)
C    Bottom Half
            v1=z(m+1,j)-z(m,j)
            v2=z(m,j+1)-z(m,j)
            c(m,j)=dcabs2(v1/dx,v2/dx)
            q1=abb(-v1/dx)
            q2=abb((z(m,j)-z(m-1,j))/dx)
            u(i+1,num+3-j)=valu(q2,q1)
            q1=abb(-v2/dx)
            q2=abb((z(m,j)-z(m,j-1))/dx)
            v(i+1,num+3-j)=valu(q2,q1)
        endif
    endif
6    continue
    endif
endif
1    continue
C
C    Put in the 0's around the border
C
do 20 i=1,num+2,1
    u(i,1)=0.
    v(i,1)=0.

```

```

    u(i,2*(num+2))=0.
    v(i,2*(num+2))=0.
20  continue
    do 21 i=1,2*(num+2),1
        u(1,j)=0.
        v(1,j)=0.
        u(num+2,j)=0.
        v(num+2,j)=0.
21  continue
C
C  Return to main program
C
    return
    end
C
C  Subroutine xout
C
    subroutine xout (x,icap)
    double complex x(500,500)
    integer icap,i,j
C
C  Fix X for the augmented matrix
C
    do 1 i=2*icap-1,icap+1,-1
        do 2 j=2*icap-1,icap+1,-1
            x(i+1,j+1)=x(i,j)
2        continue
            x(i+1,icap+1)=(0.0d0,0.0d0)
1    continue
        do 3 j=icap+1,2*icap,1
            x(icap+1,j)=(0.0d0,0.0d0)
3    continue
C
C  That's it....
C
    return
    end
C
C
    subroutine pplot (u,v,w,x)
    real u(12,24),v(12,24),w(12,24),x(12,24),y,z
C  real WRK(2200)
C  integer num
C
C  $Id: tvelvc.f,v 1.2 1993/03/05 00:12:46 halev Exp $
C
C OPEN GKS, OPEN WORKSTATION OF TYPE 1, ACTIVATE WORKSTATION
C
    CALL GOPKS (6,IDUM)
    CALL GOPWK (1, 2, 1)
    CALL GACWK (1)

```

```

C
C INVOKE DEMO DRIVER
C
C
C   SUBROUTINE TVELVC (IERROR)
C
C PURPOSE           To provide a simple demonstration of VELVCT.
C
C USAGE             CALL TVELVC (IERROR)
C
C ARGUMENTS
C
C ON OUTPUT        IERROR
C                   An integer variable
C                   = 0, if the test was successful,
C                   = 1, the test was not successful.
C
C I/O               If the test is successful, the message
C
C                   VELVCT TEST EXECUTED--SEE PLOTS TO CERTIFY
C
C                   is printed on unit 6. In addition, 1
C                   frame is produced on the machine graphics
C                   device. In order to determine if the test
C                   was successful, it is necessary to examine
C                   the plot.
C
C PRECISION        Single
C
C LANGUAGE          FORTRAN 77
C
C REQUIRED ROUTINES  VELVCT
C
C REQUIRED GKS LEVEL  0A
C
C ALGORITHM         This test program calls entries EZVEC and
C                   VELVCT. Each call produces a plot of a
C                   vector field obtained from the function
C
C                   
$$Z(X,Y) = X + Y + 1./((X-.1)**2+Y**2+.09)$$

C                   
$$-1./((X+.1)**2+Y**2+.09),$$

C
C                   by using the direction of the Z gradient
C                   vectors and the logarithm of the absolute
C                   value of the components.
C
C HISTORY           Originally written in November 1976.
C                   Converted to FORTRAN 77 and GKS in July 1984.
C
C DIMENSION        U(21,25) ,V(21,25)

```

```

C
C Specify coordinates for a plot title.
C
C   DATA IX/94,IY/1000/
C
C Specify VELVCT arguments.
C
C   DATA FLO/0./,HI/0./,NSET/0/,LENGTH/0/,ISPV/0/,SPV/0./
C
C Initialize the error parameter.
C
C   IERROR = 1
C
C Specify velocity field functions U and V.
C
C   M = 21
C   N = 25
C   DO 20 I=1,M
C     X = .1*FLOAT(I-11)
C     DO 10 J=1,N
C       Y = .1*FLOAT(J-13)
C       DZDX = 1.-2.*(X-.10)/((X-.10)**2+Y**2+.09)**2+
C 1       2.*(X+.10)/((X+.10)**2+Y**2+.09)**2
C       DZDY = 1.-2.*Y/((X-.10)**2+Y**2+.09)**2+
C 1       2.*Y/((X+.10)**2+Y**2+.09)**2
C       UVMAG = ALOG(SQRT(DZDX*DZDX+DZDY*DZDY))
C       UVDIR = ATAN2(DZDY,DZDX)
C       U(I,J) = UVMAG*COS(UVDIR)
C       V(I,J) = UVMAG*SIN(UVDIR)
C 10  CONTINUE
C 20  CONTINUE
C
C   CALL GQCNTN(IERR,ICN)
C
C Select normalization transformation 0.
C
C   CALL GSELNT(0)
C
C Call PLCHLQ to write the plot title.
C
C   X = CPUX(IX)
C   Y = CPUY(IY)
C   CALL PLCHLQ (X,Y,'Superconducting Sample Plot',
C 1   16.,0.,-1.)
C   CALL GSELNT(ICN)
C
C Call EZVEC for a default velocity field plot.
C
C   CALL EZVEC (u,v,num,2*(num+1))
C
C Call VELVCT to generate the user tuned velocity field plot.

```

```

C
C CALL VELVCT (U,M,V,M,M,N,FLO,HI,NSET,LENGTH,ISPV,SPV)
C
C call velvct(u,12,v,12,12,24,FLO,HI,NSET,LENGTH,ISPV,SPV)
C CALL GQCNTN(IERR,ICN)
C CALL SET(0.1, 0.9, 0.1, 0.9,1.0, 10., 1.0, 22.,1)
C CALL STRMLN (u,v,WRK,10,10,22,1,IER)
C call perim (1,0,1,0)
C
C Select normalization transformation 0.
C
C CALL GSELNT(0)
C
C Call PLCHLQ to write the plot title.
C
C z = CPUX(IX)
C Y = CPUY(IY)
C CALL PLCHLQ (z,Y,
1 'Superconducting Currents',16.,0.,-1.)
C CALL GSELNT(ICN)
C CALL FRAME
C CALL GQCNTN(IERR,ICN)
C
C Select normalization transformation 0.
C
C CALL GSELNT(0)
C call velvct(w,12,x,12,12,24,FLO,HI,NSET,LENGTH,ISPV,SPV)
C CALL GQCNTN(IERR,ICN)
C call gselnt(0)
C CALL PLCHLQ (z,Y,'Superconducting Potentials',16.,0.,-1.)
C CALL GSELNT(ICN)
C CALL FRAME
C IERROR = 0
C WRITE (6,1001)
C
C 1001 FORMAT (' VELVCT TEST EXECUTED--SEE PLOTS TO CERTIFY')
C
C
C DEACTIVATE AND CLOSE WORKSTATION, CLOSE GKS.
C
C CALL GDAWK (1)
C CALL GCLWK (1)
C CALL GCLKS
C
C open (unit=200, file='odata', status='new')
C do 100 i=1,num
C write (200,*) 'i=',i
C do 110 j=1,2*(num+1)
C write (200,*) 'j=',j,u(i,j),v(i,j)
C 110 continue
C 100 continue

```

```
C  close(unit=200)  
  RETURN  
END
```